University of New Mexico
UNM Digital Repository

Nanoscience and Microsystems ETDs

Engineering ETDs

Spring 3-28-2019

The Effect of Defects and Surface Modification on Biomolecular Assembly and Transport

Haneen Martinez
University of New Mexico - Main Campus

Follow this and additional works at: https://digitalrepository.unm.edu/nsms_etds

Part of the Biology and Biomimetic Materials Commons, Biomaterials Commons, Biomechanics and Biotransport Commons, Nanoscience and Nanotechnology Commons, and the Structural Materials Commons

Recommended Citation

Martinez, Haneen. "The Effect of Defects and Surface Modification on Biomolecular Assembly and Transport." (2019). https://digitalrepository.unm.edu/nsms_etds/49

This Dissertation is brought to you for free and open access by the Engineering ETDs at UNM Digital Repository. It has been accepted for inclusion in Nanoscience and Microsystems ETDs by an authorized administrator of UNM Digital Repository. For more information, please contact amywinter@unm.edu.

Haneen Martinez

Candidate

Nanoscience and Microsystems Engineering

Department

This dissertation is approved, and it is acceptable in quality and form for publication:

Approved by the Dissertation Committee:

Andrew P. Shreve, PhD., Chairperson

George D. Bachand, PhD., Co-Chairperson

Nick J. Carroll, PhD.

Francesca Cavallo, PhD.

THE EFFECT OF DEFECTS AND SURFACE MODIFICATION ON BIOMOLECULAR ASSEMBLY AND TRANSPORT

by

HANEEN MARTINEZ

B.S., Biology, 2009
B.A., Chemistry, 2009
M.S. Nanoscience and Microsystems Engineering, 2017
The University of New Mexico
Albuquerque, New Mexico

DISSERTATION

Submitted in Partial Fulfillment of the
Requirements for the Degree of

Doctor of Philosophy
Nanoscience and Microsystems Engineering

The University of New Mexico
Albuquerque, New Mexico

May 2019

Dedication

This manuscript is dedicated to my husband, who managed to get his Ph.D. along with me. I couldn't have done this without you, your movie quotes, and your inability to take anything seriously. I would like to also dedicate this to the biggest distraction in my life, my precious kids and niece, thank you (my kids) for delaying my graduation. Also, to my parents, who left me no choice but to push beyond my limits, only to achieve what I thought I could only dream of. Lastly, to my siblings, who managed to be a source of drama and laughter throughout my life and my Ph.D. journey.

Acknowledgments

I would like to sincerely thank my mentor, George D. Bachand, for giving me the opportunity to work with him, for his endless support of my Ph.D. journey, for his patience, motivation, and immense knowledge. Thank you for giving me a chance, believing in me, and for allowing me opportunity most graduate students dream of. I would also like to thank Professor Andrew P. Shreve for his support, advice, and help, both academically and personally. I would like to thank Professor Deborah G. Evans, and more recently, Francesca Cavallo and Nick J. Carroll for their advice and guidance. I would like to thank all members of my research group, and individuals I collaborated with outside my group, for making this such an invaluable experience.

THE EFFECT OF DEFECTS AND SURFACE MODIFICATION ON BIOMOLECULAR ASSEMBLY AND TRANSPORT

by

Haneen Martinez

B.S., Biology, University of New Mexico, 2009

B.A., Chemistry, University of New Mexico, 2009

M.S., Nanoscience and Microsystems Engineering, University of New Mexico, 2017

Ph.D., Nanoscience and Microsystems Engineering, University of New Mexico, 2019

Abstract

Nanoscale transport using the kinesin-microtubule (MT) biomolecular system has been successfully used in a wide range of nanotechnological applications including self-assembly, nanofluidic transport, and biosensing. Most of these applications use the ‘gliding motility geometry’, in which surface-adhered kinesin motors attach and propel MT filaments across the surface, a process driven by ATP hydrolysis. It has been demonstrated that active assembly facilitated by these biomolecular motors results in complex, non-equilibrium nanostructures currently unattainable through conventional self-assembly methods. In particular, MTs functionalized with biotin assemble into rings and spools upon introduction of streptavidin and/or streptavidin-coated nanoparticles. Upon closer examination of these structures using fluorescence and electron microscopy, the structures revealed a level of irregularity including kinked and coiled domains, as well as in- and out- of -plane loops. In this work, we describe the effects of large scale “defective” segments (i.e. non-biotinylated MTs) on active assembly of nanocomposite spools. We demonstrate the preferential removal of the defective portions from spools during assembly to overcome structurally induced strain in regions that lack biotin-streptavidin bonds. Additionally, we show how the level of defective MTs affect the morphology and physical properties of the resulting nanostructures.

Further, we explore alternative nanostructures for controlling transport using the kinesin-MT biomolecular system. Guiding MT transport has been achieved using lithographically patterning physical and chemical features, which have been shown to limit the MT trajectories, causing MTs to escape the barriers and lead to stalling or complete loss of MTs. Here, we demonstrate reliable guiding and transport of MTs on three different chemically modified, and structurally varying surfaces using 1) self-assembled monolayers (SAMs) with varying functional groups, 2) Fetal-bovine serum (FBS) coated SAMs to generate protein patterns, and 3) silicification of the FBS coated SAMs to preserve the surface. Overall, the work presented in this dissertation provides crucial insights for future development of dynamic and adaptable hybrid nanostructures, as well as provides biocompatible patterns to modulate MT motility with the goal of advancing self-regulating, multi-functional materials.

Table of Contents

List of Figures.....x

List of Tables.....xi

Chapter 1.....1

Introduction and overview of this work.....1

Chapter 2.....9

Biomolecular motors in nanotechnology.....9

- Introduction.....10
- The cellular cytoskeleton.....10
  - Microtubule cytoskeletal filaments.....11
  - Kinesin biomolecular motors.....14
- Biomolecular transport systems in nanotechnology.....18
  - Bead Geometry.....19
  - Gliding Geometry.....19
- Guiding of molecular shuttles.....21
  - Surface topography to guide the molecular shuttles.....22
  - Surface chemistry to guide the molecular shuttles.....25
  - Guiding using the combination of surface topography and chemistry.....27
- Cargo loading and unloading.....28
- Nanomaterials assembly.....31
  - Bundles and network structures.....32
  - Rings and spools.....34
- Conclusions.....39

Chapter 3.....41

How building block composition affects the active assembly of microtubule spools.....41

- Abstract.....42
- Introduction.....44
- Materials and Methods.....47
  - Preparation of motor proteins.....47
  - Preparation of Microtubules.....48
  - Motility assays.....48

Fluorescence Microscopy 49
Calculation of fraction defect MTs in spools 50
Results and discussion 51
Conclusions 61
Acknowledgements 61
Appendix 63
Chapter 4 69
Biomolecular probes navigate through chemical and topographical landscapes 69
Abstract 70
Introduction 72
Materials and methods 76
Fabrication of self-assembled monolayers (SAMs) 77
Protein deposition 77
Silicification 78
Contact angle measurements 78
X-ray photoelectron spectroscopy (XPS) 78
Atomic force microscopy (AFM) 79
Preparation of motor proteins 80
Preparation of Microtubules 80
Motility assays 81
Fluorescence Microscopy 81
Image and Statistical Analysis 82
Results and discussion 82
Characterization of self-assembled monolayers (SAMs) 82
Characterization of Fetal Bovine Serum (FBS) coated SAMs 87
Characterization of silicified FBS coated SAMs 90
Effect of substrate modification on microtubule velocity 92
Effect of SAMs substrates on MT trajectory and displacement 96
Effect of FBS coated SAMs substrates on MT trajectory and displacement 100
Effect of silicified FBS-coated SAMs substrates on MT trajectory and displacement 101
Conclusion 103

Acknowledgments 105

Appendix 106

Chapter 5 112

Conclusions and future direction 112

References 121

List of Figures

Figure 2. 1. schematic representation of a microtubule and polymerization process 12
Figure 2. 2. Schematic representation of Kinesin-1 and the mechanochemical cycle of the motor 15
Figure 2. 3. Schematic representation of the gliding (inverted) motility assay ... 20
Figure 2. 4. Guiding of molecular shuttles and investigation of surface properties and topography 23
Figure 2. 5. Guiding of molecular shuttles using surface chemistry and the combination of surface topography and chemistry. 26
Figure 2. 6. Cargo loading 29
Figure 2. 7. Phase diagram for the morphology of self-assembled microtubule structures as a function of cross-linker ratio (streptavidin/biotin or St/Bt) and tubulin concentration (Tub). 32
Figure 2. 8. Assembly of nanocomposite spools 37
Figure 3. 1. Assembly of spools using segmented MTs 52
Figure 3. 2. Spool morphology and size. 53
Figure 3. 3. Theoretical vs. measured fraction of non-bonding MTs in spools ... 55
Figure 3. 4. Breakage and release of non-bonding MTs 58
Figure 3. 5. Spools integrate or reject MTs upon collision 59
Figure A 3. 1. Average inner diameter and thickness of spools 64
Figure A 3. 2. Average length and count of MT domains within the segmented MTs. 65
Figure A 3. 3. The average density and length of unattached non-bonding MTs (i.e., not in spools) as a function of percent non-bonding MTs 66
Figure A 3. 4. Average change in density and length of bonding MTs as a function of non-bonding MT level 67
Figure A 3. 5. Average change in density and length of segmented MTs as a function of non-bonding MT percent 68
Figure 4. 1. Schematic of the in vitro gliding motility assay on top layer (SiO_2) . 73
Figure 4. 2. Atomic force microscopy (AFM) topography images. 85
Figure 4. 3. MT tracking to determine and average gliding velocity 93
Figure 4. 4. MT motility on various SAMs surfaces. 98
Figure 4. 5. MT motility on FBS coated SAMs. 100
Figure 4. 6. MT motility on silicified, FBS coated SAMs. 101
Figure A 4. 1. Surface topography using atomic force microscopy (AFM). 107
Figure A 4. 2. SEM images of FBS coated SAMs 108
Figure A 4. 3. Histograms of microtubule gliding velocities for SAMs, FBS coated SAMs, and silicified FBS coated SAMs. 109

List of Tables

Table 4. 1. X-ray photoelectron spectroscopy atomic composition and static water contact angles. 83
Table A 4. 1. Statistical results comparing velocity of gliding MTs on the various substrates. 110
Table A 4. 2. Statistical results comparing MT velocity on the various SAMs functional groups. 111

Chapter 1

Introduction and overview of this work

For centuries, humankind has taken advantage of biological materials by extracting and adapting them for our needs. For example, animal proteins such as silk or wool have been transformed into materials that significantly impacted and influenced cultural and economic growth throughout human history[1]. Protein based materials have significantly evolved due to the scientific advances that allowed for exploring their use in a radically different manner, as they provide enormous potential especially at the nanoscale. Our extraordinary understanding of the biophysics of many proteins have enabled researchers around the world to tailor individual units and tune their function and shape to be used for many nanotechnological applications[1,2]. Cytoskeletal motor proteins such as kinesin have been proven to be very promising for nanotechnological applications because they are capable of converting chemical energy into mechanical motion.

Thus far, nanoscale generation of mechanical work in synthetic material systems has been achieved through[3,4]: 1) bottom up design of molecular motors through chemical synthesis, in which conformational changes can be achieved using light or fuel molecules to enable macroscopic changes of material properties[5–9], 2) top down fabrication using lithography to create miniaturized electric motors (e.g. carbon nanotubes) at the submicron level[10], and finally 3) biomolecular motor integration into synthetic environments, which proves advantageous over the other two approaches, as it overcomes the challenges of designing the motors and instead focuses on the integration of such highly efficient and functional nanomachines into a synthetic environment[11].

Many applications that involve nanomotors include, but are not limited to, biosensing, nanofluidics, molecular electronics, nanoscale/macroscale actuation, adaptive materials, and nanoscale transport, which were inspired by macroscale technology and advances in our understanding of molecular and cellular processes[4]. Biomolecular motors offer many advantages with respect to many of these applications. In particular, the genes that encode these proteins are well studied and known and can be inserted into bacteria to produce large numbers of these motor at a very low cost, hence enabling efficient biotechnological production[12]. The ability to modify the genes enabled additional tuning of mechanical and chemical parameters, as well as introducing chemical linkers to further modify the motors[4].

Further, these motors exhibit remarkable efficiency in converting chemical energy into mechanical work (≥ 50%) compared to manmade nanomachines powered by electrical energy that yield low efficiency (<30%) with large heat loss[1]. Additionally, these motors move fast, approximately 100 steps (8 nm per step) per second[13]. These motor proteins undergo dramatic conformational changes due to the binding and hydrolyzing of ATP in a cyclic process, and specifically bind to their complementary filaments, in this case, Microtubules

(MTs) for kinesin motors. MTs are linear polymers of tubulin proteins and serve as “railroads” or specific structures that kinesin motors exert force against. Through the conformational changes during hydrolysis coupled with the kinesin motor’s affinity to cytoskeletal filaments, motors can move or “walk” along MTs in a directed stepwise manner. These nanomachines are truly an example of how polymeric structures can evolve in nature, a characteristic unmatched by man-made nanomachines[14].

These motors, however, have a major disadvantage of a limited lifetime *in vitro*, in addition to very limited environmental conditions that can be tolerated[4]. Nevertheless, biomolecular motors operate autonomously in a constant environment, which far exceeds performance advantages of synthetic polymer nanomachines such as poly(N-isopropyl acrylamide)(PNIPAM). For example, protein grafted PNIPAM can undergo phase transition from collapsed to extended state to block a binding site[14–16], however, this type of nanomachine requires continual external stimulus. Although artificially designed motors, for example DNA motors, have been shown to operate autonomously, they are still far behind on speed and efficiency, orders of magnitude lower as compared to biomolecular motors[14,17,18]. The ability of molecular motors to continuously cycle through their mechanochemical cycle (ATP hydrolysis of ~ 12kcal/mol) allows for many applications of long-distance transport and independent operation[4].

The technological applications and advances of biomolecular motors since their discovery would not have been possible without the collaborative efforts of biophysicists and cell biologists to discover and expand the designs and roles of motors in cells and in artificial environments. The research involved in advancing their application in biotechnology was achieved by using research advances in motor proteins arising from studies of cancer, heart disease, Alzheimer’s and other topics[4,19–22].

Much of the research used the ‘gliding motility assay’ [23] in which MTs (or actin filaments) attach to surface-bound kinesin (or myosin) motors and glide in the presence of ATP. This arrangement sparked the idea of exploring the transport mechanism of this biomolecular system in nanotechnology, based on the notion of allowing for directed and controlled movement of cargo using these ‘molecular shuttles’ [24–28]. Additionally, an alternative configuration can provide single-molecule transport in which filaments are immobilized on the surface and motors then attach and “walk” on the filaments. The two arrangements can also be combined successfully for more complex applications[4]. **Chapter 2** of this work provides a detailed overview of the basic characteristics of the kinesin-MT biomolecular transport system discussed above, along with research and advances using this biomolecular system in nanotechnological applications such as guiding approaches, loading and unloading of cargo, and achieving desired nanostructures. This comprehensive review will likely form the basis of a published review article in the future.

Highly strained, complex non-equilibrium structures have been assembled using active, motor-driven transport of kinesin-MT system. The configuration of these structures is not defined by the connections of their building blocks, but instead, their internal ordering is derived by the transport mechanism. Active transport using this biomolecular system can also be tuned (e.g. motor density, fuel concentration) to enable more control over desired complex structures, as compared to thermally activated self-assembly processes that are limited to a narrow range of temperatures (i.e., limited overall control mechanism). As such, biomolecular transport systems have been shown to contribute to nanomanufacturing by pushing the boundaries of molecular self-assembly[4]. Specifically, biotinylated MTs translated by surface-bound kinesin motors can form rings and spools when bound to streptavidin or streptavidin-coated nanoparticles (e.g. quantum dots (sQDs)) [29–33].

Although these structures sustain a level of order, fluorescence and electron microscopy reveal that these rings and spools contain irregular domains including twisted and kinked domains, as well as well as in- and out- of-plane loops[34,35]. Because these structures can tolerate a level of structural heterogeneity, they should also tolerate and possibly compensate for the controlled introduction of MTs that lack biotin (i.e. MTs that cannot bind sQDs). Because these non-biotinylated MTs cannot participate in spool formation, and hence are considered “defective”, we hypothesized that the spools’ ability to manage such defective building blocks will depend on the size and frequency of the defective MTs. **Chapter 3** in this work details the effect of introducing large-scale (micron size) defective building blocks (i.e., non-biotinylated domains) on the assembly of MT spools. This was accomplished by end-to-end annealing of MTs to create segmented MT building blocks with alternating biotinylated MTs (capable of forming spools) and defective MTs (non-biotinylated). We then implemented the ‘gliding assay’ to study the effects of the defective MTs on the morphology and physical properties of the resulting structures, and we provide detailed investigation on how the defective building blocks were managed.

The work detailed in Chapter 3 is currently in revisionas a research article in *Nanoscale*. As the primary author on this article, most of the research was performed by me at the Center for Integrated Nanotechnologies (CINT), Sandia National Laboratories (SNL). My role in this article was to design and perform all experiments, including MT preparation, assay preparation and performance, imaging, as well as image and data analysis. I was also responsible for preparing the manuscript and subsequent revisions. Virginia Vandelinder, the second author, assisted in experiments, analysis, and assisted in preparing the manuscript and revisions. Zackary Imam assisted in image and data analysis. Erik D. Spoerke assisted in writing the introduction of the manuscript and revising the article. Supervision, experimental input, data/statistical analysis, along with manuscript writing and revisions was provided by George D. Bachand. The format of this chapter is organized as follows: abstract, introduction, materials and methods, results and discussion, and acknowledgements. Supporting information for each chapter is included as an Appendix at the end of each chapter with corresponding figures. Chapter 4 is formatted in a similar manner for consistency to the reader.

Chapter 4 presents a collaborative effort between the University of New Mexico (UNM) and SNL. This manuscript will be submitted to *ACS Applied Materials and Interfaces* (ACS AMI). As the primary author of this work, my role was to design and perform the experiments at UNM and CINT, with the aid and guidance of fellow authors. I was responsible for preparing the MTs, preparing the self-assembled monolayers (SAMs) on glass, fetal bovine serum (FBS) layers on SAMs, preparing and performing motility assays, contact angle measurements, imaging using fluorescent microscopy, image and statistical analysis. I was also responsible for preparing the manuscript and subsequent revisions. Nicholas Martinez, the second author, contributed to the research plan, helped with image and data analysis, and assisted in writing the manuscript. Jimin Guo, the third author, also contributed to the research plan, performed silicification on the FBS coated SAMs samples, performed scanning electron microscopy (SEM) on the FBS layers, and provided input and revisions to the manuscript. Victoria Lujan perfumed image analysis. Jessica Depoy performed atomic force microscopy (AFM) on all samples. Michael T. Brumbach performed X-ray photoelectron spectroscopy (XPS) on all samples. Investigators on this research, C. Jeffrey Brinker and George D. Bachand provided guidance on experimental and data interpretation, and manuscript revisions.

The work in Chapter 4 describes the effects of surface chemistry and topography on MT transport behavior. Thus far, the control of MT gliding can be achieved by a variety of mechanisms including lithographically patterning chemical and physical features. These methods, however, can expose biological materials to harsh organic solvents, tend to be expensive, and have caused MTs to get stuck and detach from nanostructured surfaces, as well as limit MT run-time with poor motility quality. Overall, they therefore are limiting for more complex applications of the biomolecular transport system[36]. In this work, we explore the regulation of MT transport behaviors by implementing a more biocompatible alternative through: 1) chemically modifying the surfaces with self-assembled monolayers (SAMs) with varying end groups, 2) adding a protein layer by incubating the SAMs in Fetal Bovine Serum (FBS) to create protein patterns with varying morphology, and 3) silicifying the FBS coated SAMs to preserve the outermost protein structures. MT motility was evaluated on each of the three layers mentioned above. This approach enabled the production of topographically unique nanostructures and preserved features with chemical and structural diversity to study MT gliding and the ability of kinesin motors to guide motion.

A summary of the work presented in this dissertation along with possible future directions for this work are presented in **Chapter 5**. Overall, this dissertation demonstrates how the kinesin-MT biomolecular transport system continues to provide a means of achieving biomimetic functionalities for future development of nanoscale materials, specifically ones that exhibit self-regulating, healing, and adaptive features.

Chapter 2

Biomolecular motors in nanotechnology

Introduction

Molecular motors such as kinesin, enable a wide range of functions ranging from active transport in cells to large-scale actuation by muscles, and achieving these complex functions by efficiently converting chemical energy into mechanical work[4]. These motor proteins provide inspiration to be employed in synthetic nanodevices, and were the first prototypes of molecular shuttles[28]. This review focuses on the basic characteristics and the contributions involving the biomolecular motor kinesin and their associated filaments Microtubules (MTs) in nanotechnological applications. Techniques developed to guide the movement of the MT shuttles including surface topography and chemistry will be reviewed. Further, the coupling of cargo to the shuttles through strong and specific linking, as well as types of actively-assembled structures achieved are briefly discussed.

The cellular cytoskeleton

When the term “cytoskeleton” was first established in 1931 [37,38], cytoskeletons were thought of as a static, fibrous structural system that provides reinforcement. It eventually became clearthat it is highly dynamic and is involved in many major cell processes such as muscle contraction, the beating of cilia, chromosome segregation, cell division, phagocytosis, and organelle transport[38]. Both prokaryotic and eukaryotic cells have an internal cytoskeleton[39–44]. In eukaryotic cells, it is a protein scaffold that consists primarily of a network of three types of filaments: actin, microtubules (MTs), and intermediate filaments[39,40]. Two of these filaments, specifically actin and MTs, serve as “tracks” for biomolecular motors (myosin and kinesin, respectively) to transport vesicles and organelles around the cell [45]. In the following sections, a brief overview of the structure, properties, dynamics, and nanotechnological applications of the MT- kinesin system will be presented.

Microtubule cytoskeletal filaments

MT's are polymeric filaments that provide structural support for the cell and act as intracellular network to facilitate motor protein transport [39,45,46]. The fundamental building blocks of MTs are α- and β-tubulin monomers that share ~ 50% homology in their primary sequence[47]. These monomers bind together tightly through hydrophobic and electrostatic interactions to form a heterodimer[48,49], with a molecular weight of ~ 110 kDa, diameter of ~ 4nm, and ~ 8 nm in length. Each dimer has two bound guanosine triphosphate (GTP) molecules, one at the nonexchangeable (N) site on the α subunit where GTP is never hydrolyzed, and one at the exchangeable (E) site on the β subunit that is hydrolyzed to GDP during microtubule assembly [49] (Figure 2.1a).

These dimers bind head-to-tail [50] to form linear protofilaments that vary in number, 13-14 *in vivo*, while *in vitro* the number can vary from 10-15 [51–53], with most microtubules consisting of 13 protofilaments [51] (Figure 2.1b). The protofilaments associate to form extended sheets, and eventually form a cylindrical structure with an outer diameter of about 25 nm, inner diameter of about 15 nm, and a length of many micrometers [50,51,54]. Tubulin heterodimers

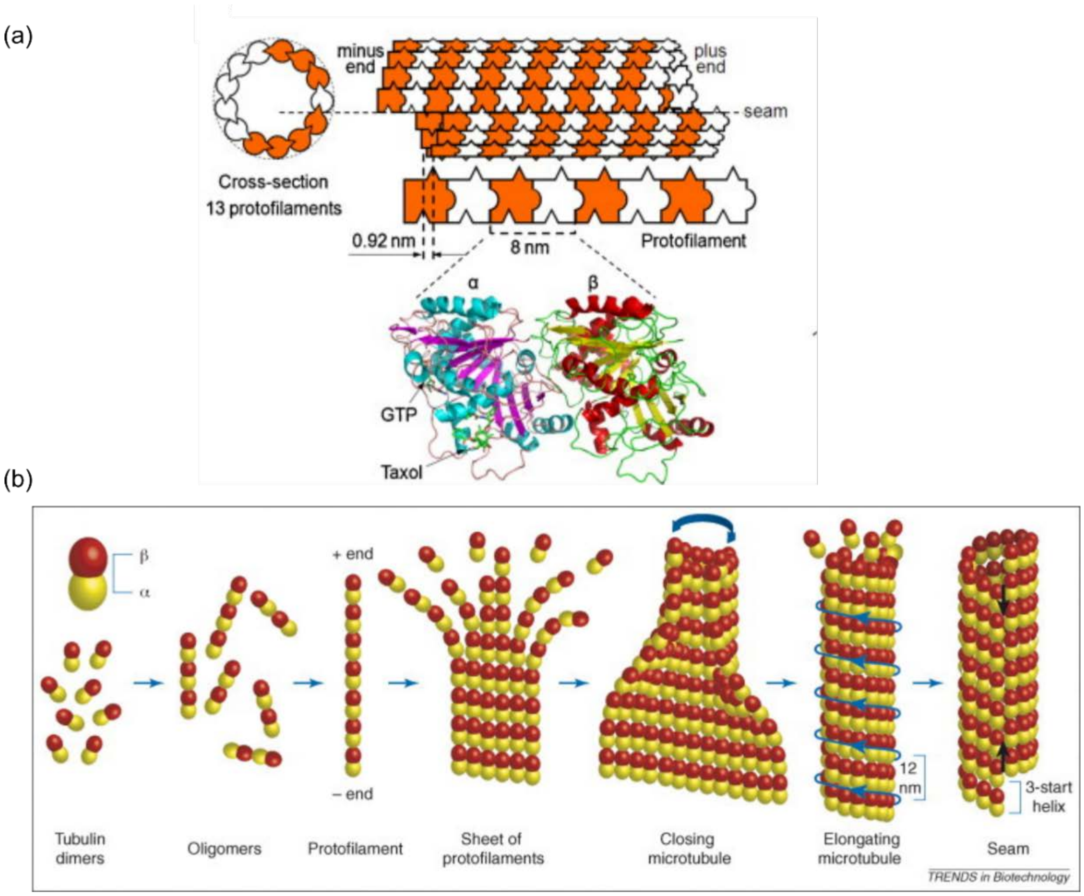
(a)
minus end
plus end
seam
Cross-section
13 protofilaments
0.92 nm
8 nm
Protofilament
α
β
GTP
Taxol
(b)
β
α
+ end
– end
12 nm
3-start helix
Tubulin dimers
Oligomers
Protofilament
Sheet of protofilaments
Closing microtubule
Elongating microtubule
Seam
TRENDS in Biotechnology

Figure 2.1. schematic representation of a microtubule and polymerization process. (a) Microtubule consisting of 13 protofilaments made up of linear chains αβ tubulin dimers (~ 8 nm) with an outer diameter of ~ 25 nm and lengths in the tens of microns. Ribbon diagram shows the GTP and Taxol binding sites, derived from electron crystallography[55]. (b) Polymerization process is initiated by tubulin dimers binding together in a head-to-tail fashion to form oligomers that elongate into protofilaments. Protofilaments interact laterally to form sheets once they reach 12 ± 2 dimers with an inward curvature, and the sheet closes into a tube (~13 protofilaments) to form the microtubule. The lattice forms a left-handed helical symmetry and discontinuity at the closure site (i.e. seam shown in black arrows). Figure (a) was adapted from Agrawal and Hess[14] and (b) was adapted from Pampaloni and Florin[56], and both reprinted with permission from Elsevier.

form non-covalent bonds, both longitudinally and laterally between the dimers in a protofilament, in which longitudinal bond energy is greater than the lateral bond[57,58]. In the cell, MTs primarily consist of 13 protofilaments, with ~ 0.92 nm offset between dimers on adjacent protofilaments. If a sheet contains less or more than 13 protofilaments, the MT undergoes lattice rotation causing the protofilaments to follow a helical path around the MT surface as opposed to running parallel to the MT axis [40]. These hollow tubular filaments possess high flexural rigidity, resulting in characteristic persistence lengths ranging from 1 to 10 mm [59]. Since the protofilaments bind to each other in the same direction, the microtubule develops structural polarity, where one end is slow growing, terminated by an α-tubulin (i.e., minus end), and the other end is fast-growing, terminated by a β-tubulin (i.e., plus-end). The linear charge density has been reported for MTs at ~ 280 e^-/ μm^-, approximately 0.19 e^- average charge per tubulin dimer [60,61], while the α- and β- terminated ends have positive and negative electrostatic potentials, respectively [62].

MTs are highly dynamic structures that endure persistent phases of growing and shrinking, with abrupt transitions between the phases, a phenomenon known as “dynamic instability” [63]. The growing and shrinking of MTs depend on the hydrolysis of GTP, and produce forces up to 40 pN and -15 pN, respectively [40]. When microtubules are in the growth phase, GTP in the E-site is hydrolyzed to GDP [49], inducing structural transitions that affect the longitudinal interfaces and overall MT lattice stability [64]. If polymerization exceeds hydrolysis, a “cap” of GTP-tubulin forms at the plus-end of the growing filament, stabilizing the MT. If the rate of GTP hydrolysis surpasses polymerization, the MT loses its GTP cap, and rapid depolymerization occurs (a phenomenon known as “catastrophe”). The depolymerization of the MT stops when a GTP tubulin encounters the MT lattice to initiate the growth phase (a phenomenon known as “rescue”) [65]. In the cell, proteins such as MAP2 and Tau modulate dynamic instability to increase the frequency of rescue and suppress catastrophe [66]. In vitro, MTs are stabilized using an anticancer drug paclitaxel (i.e., Taxol ®) for nanomaterial applications [67], where the drug binds specifically to the β-tubulin near the GTP binding site [68].

Although dynamic instability is stochastic and energy intensive, evolution clearly favors such process because dynamic MTs have been present in every eukaryotic organism (> 700 million years) [69]. Dynamic instability allows MTs to easily reorganize and efficiently search the three-dimensional volume in the cell to find targets. Additionally, It allows cells to perform multiple tasks, such as generating pushing and pulling forces [70] to enable, for example, movement of vesicles and intracellular components, and to separate chromosomes into two daughter cells during mitosis [71].

Kinesin biomolecular motors

Kinesin was first discovered in 1985 by Vale and colleagues, based on the first observation of transport in the cytoplasm extruded from the giant axon of the squid [72–75].The purified protein, known as Kinesin-1, is essential for transporting of vesicles and organelles [76], especially over large distances [77]. Kinesins are also involved in cell division, and the organization of cilia and flagella [14,78,79]. It has been reported that kinesin mutants lead to paralysis, lethality and vesicle jams, [80,81] and the motors’ association with disease-causing proteins can lead to degenerative neurological disorders [82,83]. The kinesin family of microtubule-based motors is large; humans have ~ 45 different kinesin motors with specific roles to support the needs of the cell [69]. Phylogenic analysis defined groups within the kinesin family, and divided them into 14 separate families, based on cellular functions in different cells or organisms [84,85].

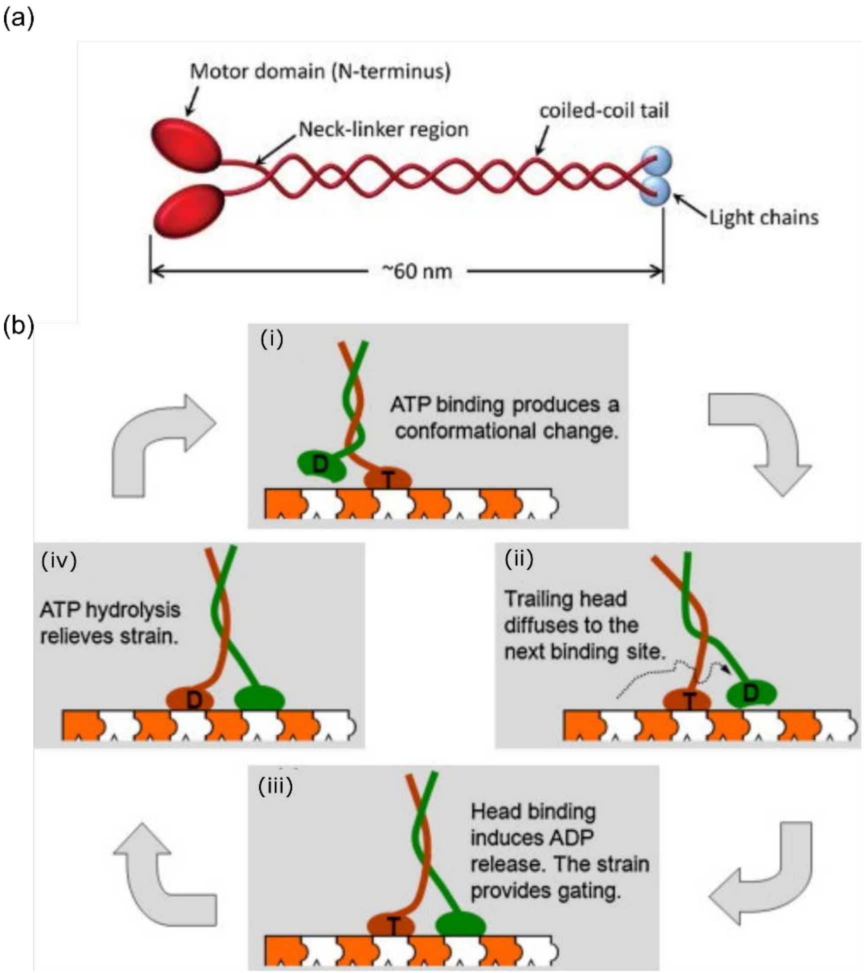
(a)
Motor domain (N-terminus)
Neck-linker region
coiled-coil tail
Light chains
~60 nm
(b)
(i)
ATP binding produces a conformational change.
D
T
(ii)
Trailing head diffuses to the next binding site.
T
D
(iii)
Head binding induces ADP release. The strain provides gating.
T
(iv)
ATP hydrolysis relieves strain.
D

Figure 2.2. Schematic representation of Kinesin-1 and the mechanochemical cycle of the motor. (a) schematic representation showing the cargo binding light chains, the coiled-coil stalk domain, the neck linker, and the motor or head domain of the kinesin motor. Figure adapted from Bachand et al.[45] and reprinted with permission from John Wiley & Sons, Inc. (b) Proposed ‘hand-over-hand’ cycle of kinesin[86]. (i) The leading head undergoes a conformational change due to ATP binding, resulting in movement of the trailing head towards the plus end of the microtubule. (ii) The trailing head reaches the next binding site (~ 16 nm). (iii) Binding to the microtubule leads to ADP release from the new leading head, further straining the neck linker region and causes the two head domains to experience gating in different states. (iv) The strain is relieved upon ATP hydrolysis releasing a phosphate from the now trailing head, and the cycle repeats in which the new leading head binds ATP. Figure reprinted from Agarwal and Hess[14] with permission from Elsevier.

Kinesin-1 is a tetramer of two identical “heavy chains”, and two associated “light chains” (Figure 2.2a). The heavy chains fold into two globular heads at one end, attached to a stalk in the middle, and a tail (light chains) at the other end[87]. Crystal structures revealed invariant folds in divergent kinesins, indicating the head is highly conserved[88,89], and contains both the polymer-binding (MT or actin) and ATP-binding sites[69]. The coiled-coil stalk contains a flexible region known as the “hinge”, which permits the tail to fold back onto the head to inhibit motor binding to MTs and also coordinates the heads to allow for movement along MTs[90] . The 50 nm, highly flexible tail domain[91] of Kinesin binds to cellular cargo, where the selectivity of binding is controlled by specific functional marker molecules and binding proteins[28,92]. Further, the tail enables transport, and can serve as an inhibitory regulator, however, it has been less well studied than the head and stalk[40,69,75].

These motor proteins rely on adenosine triphosphate (ATP) for energy source, and are capable of converting its chemical energy (ATP) into linear motion with an efficiency exceeding 50% (measured by the ratio between performed work and free energy of ATP). [28,93] These proteins possess a sense of direction, where their morphology defines which direction they move on the filaments [28]. Kinesin-1, for example, moves towards the plus end of the microtubules, while Kinesin-14 (c-terminal motors) moves towards the minus end[45].

Kinesin-1 is a highly “processive” motor protein, in which at least one head is attached at any point in time while the motor ‘walks’, allowing the motor to follow a filament or MT in a continuous, uninterrupted motion. Such processive movement allows for a traveled distance of several micrometers, more than hundred steps each time a single motor binds to an MT before detaching.[13,28,94–96] Because of its high degree of processivity, a single kinesin molecule is able to propel MTs along a surface[13]. Although the exact sequence of events of the mechanochemical cycle of kinesin is still debated[14], several studies have confirmed that Kinesin-1 walks along microtubules by an alternating head or ‘hand-over-hand’ mechanism, depicted in Figure 2.2b. The motor’s head domain undergoes a small conformational change in the ATP binding site upon hydrolysis to ADP while the head is attached to the filament. The conformational change is then amplified by the lever arm ‘neck’ [97], and results in the movement of the trailing head forward and towards a specific direction (minus end for Kinesin-1) along the filament. After this ‘power stroke’, the head detaches and binds to the next available binding site on the filament[14,69].

Each head takes 16-nm steps, thus moving the entire molecule 8 nm (consistent with the spacing of αβ tubulin dimers) in a single step for each molecule of ATP it hydrolyses, resulting in long excursions towards the microtubule plus-end, as mentioned previously[98–105]. The force associated with the kinesin stepping has been reported at approximately 6 pN per step, which translates to approximately 48 pN nm of energy expended, with high thermodynamic efficiency (~50%) as previously discussed[45]. Kinesin motors have been reported to walk along microtubules at speeds of 1 µm/s *in vitro*, saturating ATP concentrations, with a stall force of approximately 8 pN (independent of ATP concentration)[40].

Biomolecular transport systems in nanotechnology

Motor proteins and their associated cytoskeletal filaments have captured much interest in biotechnological applications, and have been used in synthetic environments [23,106–108]. The linear micrometer sized structures formed from individual tubulin monomers can dynamically self-assemble in a reversible manner, and such properties have been explored for templating of nanostructured, inorganic materials [109–116]. For motor proteins, bioengineering applications have been centered around mimicking their roles in biological systems, such as detecting analytes, modulating mechanical properties of materials, aiding in nanoscale assembly, and in particular, their function as nanoscale transport systems.[1,14]

Motor proteins offer many advantages for synthetic devices, including the similarity in function *in vivo* and *ex vivo*, the immense knowledge available, and the ability to produce significant quantities of the protein through recombinant methods. However, limitation of devices based on motor proteins is inevitable since proteins need to be maintained in conditions similar to their native environment (i.e. cytosol). Some limitations include pH, salt content, temperature, denaturing substances, concentration of ATP, synthetic surface properties (can lead to denaturation of the protein), and degradation of protein if not frozen or lyophilized. [13,28,117,118] A major breakthrough to overcome such challenges came about through the development of *in-vitro* ‘motility’ assays[23]. Motility assays employ two different geometries, called the ‘bead assay’ (filaments stationary, motors moving), and the ‘gliding assay’ (filaments moving, motors stationary), in which both approaches have been utilized to mimic the biological applications of motor proteins[14].

Bead Geometry

In the bead geometry, the MT filament is typically adsorbed and immobilized onto a surface (e.g. glass), and the motor protein attached to a polystyrene microsphere (i.e. “bead”) walks along the filament. This minimalistic reconstruction that mimics the intracellular architecture has been used for many specific technological applications. For example, the walking mechanism of molecular motors was explored by determining the displacement of the bead over time using optical tweezers to exert force on the bead[14,101,105,119–124]. This geometry can also be applied to multiple motors of the same or different kind, attached to a bead, to explore transport properties similar to overcrowding in cellular environment[14,125,126]. Although this geometry offers many advantages, it also possesses limitations such as size of tracks being limited to tens of microns (length of MTs), and it doesn’t allow for simple organization of filaments into complex architectures necessary to realize more complex applications[45].

Gliding Geometry

The majority of nanotechnological applications involving cytoskeletal transport have adapted the “gliding” or “inverted” motility geometry. The gliding geometry uses surface immobilized biomolecular motors, in which the tails of the motors are adsorbed to the surface and the motor heads transport the filaments, much like crowd surfing at a rock concert (Figure 2.3). This geometry offers many advantages including long run lengths that depend on availability of ATP, and allows for functionalization of cytoskeletal filaments with biological and/or synthetic cargos[45]. Additionally, unlike the bead geometry, it is not limited by run lengths, but instead allows filaments to move for centimeters without interruption with sufficient surface coverage of motors. The length scale of motion is also enhanced because of the simultaneous interaction of multiple motors with the filament[14,127], which decreases the likelihood of the filament detaching from the surface.

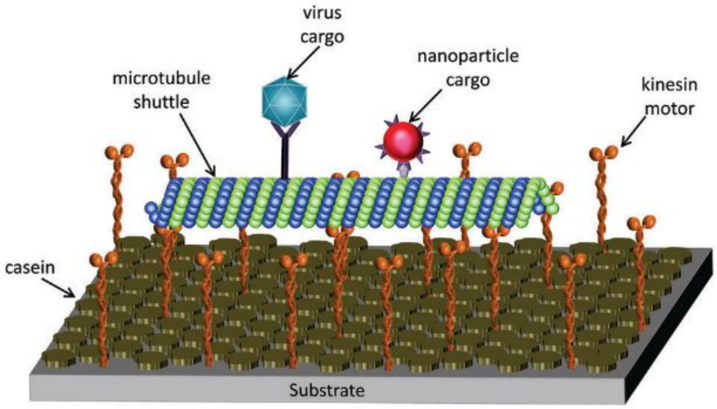

Figure 2.3. Schematic representation of the gliding (inverted) motility assay. Microtubules transporting cargo (e.g. nanoparticles) attach and are propelled over the surface by surface-bound kinesin motors in the presence of ATP. Figure reprinted from Bachand et al.[45] with permission from John Wiley & Sons, Inc.

The work in the following chapters uses the gliding geometry, and therefore, it is essential to briefly describe the setup of this geometry. Gliding assays are achieved in “flow cells” assembled using a glass slide and a glass coverslip separated by spacers of approximately 100 µm height[108]. Such an assay is usually performed in the following order[28]: (1) A protein monolayer is first adsorbed onto the surface through a flow-through of a solution containing casein or albumin to reduce denaturation and to enhance motor activity following non-specific adsorption[108,128], (2) exchange of solution containing the molecular motors allows the motors to adhere to the pretreated surface, (3) third solution flow-through to adsorb the filaments to the motors, and finally (4) imaging with fluorescence microscopy.

Guiding of molecular shuttles

Mastering the fast and precise positioning of nanoscale objects has been greatly advanced through strides in nanotechnology methods. However, limitations such as low compatibility of biological molecules with harsh nano-structuring methods continues to hinder some applications. Biomolecular motors, such as Myosin V or Kinesin-1 have evolved in nature specifically for intracellular transport, making them of prime interest to integrate into devices to power nanoscale transport systems[1,40].These molecular shuttles offer the advantage of overcoming limitations of diffusive transport over long distances, and can carry large cargo particles. Over short distances, they offer directed transport capable of handling the load without detour, allowing for increased delivery speed, dependent, of course, on the size of cargo loading and unloading areas[129].

Typically, on planar surfaces coated with motor proteins, cytoskeletal filaments perform persistent random walks. The paths result from the Brownian motion of the advancing tip of the filament as it finds the next motor. The trajectory path is then modeled as a worm-like chain, with stochastic properties characterized by the persistence length[14,130,131]. Although random movement of shuttles is advantageous to some devices, guiding along predetermined paths is highly desirable to specify direction for transport along a path, ideally including the ability to switch between alternative paths.[14] For example, microfabrication methods have been used to control the spatial distribution of the protein tracks, while external forces such as electric, magnetic fields, light or heat have been used to guide or control their position[1].

Surface topography to guide the molecular shuttles

Barriers to physically confine motility of filaments have been achieved by using surface topography. When the MT shuttles collide with the inflexible sidewalls of the barriers, the large guiding forces of motors pushing the tip are then transformed into bending forces for the filaments. This then results in the guiding along the direction of the channel walls (Figure 2.4a).[14,27,132–134] Simple ridges and grooves were one of the first designs of physical barriers for both the actomyosin and kinesin-MT system, but the widths and heights of these ridges were not easily controlled.[26,135] This limitation was mitigated by fabricating replica-molding of polyurethane channels, with easily reproducible features.[27] Although many of these guiding channels are deep enough (i.e. > 200 nm) to prevent filaments from physically escaping the walls, the guiding approach angle remains the main factor in guiding efficiency upon filaments colliding with the channel sidewalls.[136–138]

The bidirectional movement of shuttles along the filaments' tracks is made possible due to the adsorption of filaments in random directions on the guiding channels. As such, unidirectional movement was enabled by utilizing “rectifier” tracks. For example, an ‘arrowhead’-shaped rectifier permitted unidirectional movement with a 70% success rate, allowing for the development of advanced rectifier designs to improve rectification efficiency and mechanisms. The introduction of an undercut at the bottom of the guiding channel wall (Figure 2.4b) prevented the filaments from climbing the sidewall, and such confinement enabled the preferential movement of filaments in the undercut region. This, combined with various other rectifier designs, allowed for efficient guiding and enabled unidirectional motion.[14,139–145] Furthermore, completely capped microfluidic channels have been employed for the kinesin-MT system, providing three-dimensional confinement.

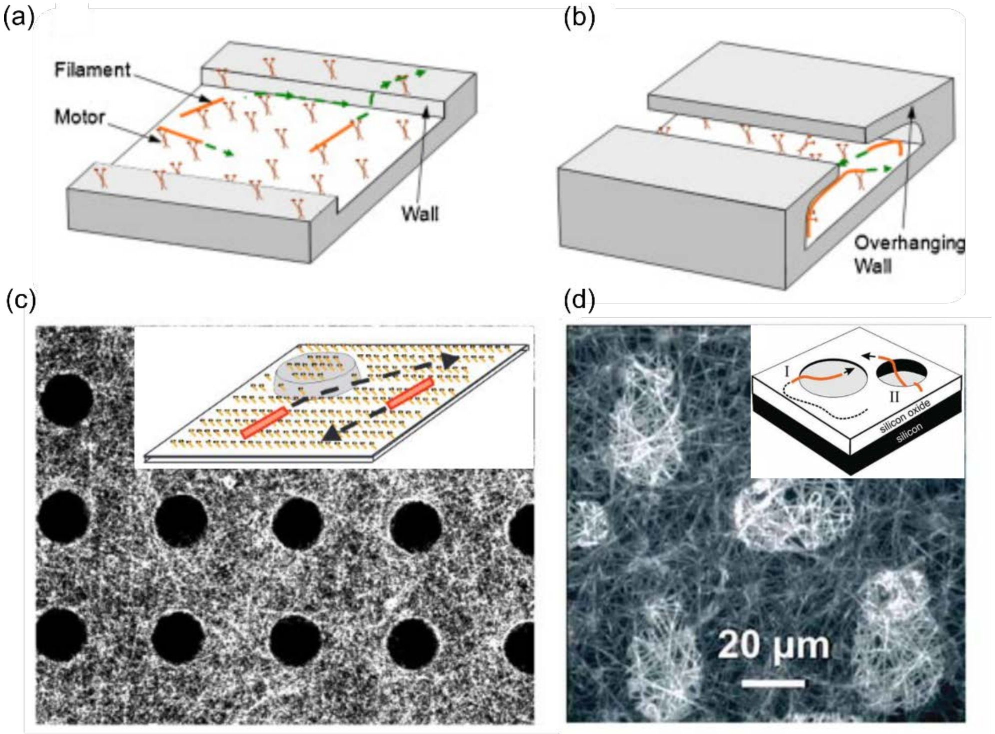

Figure 2.4. Guiding of molecular shuttles and investigation of surface properties and topography. (a) Guiding using surface topography, in which the walls act as a normal force and bend the filaments along the wall. This approach however,

enables MTs to escape by climbing the wall (depending on approach angle) and attaching to motors adhered to the wall. (b) Guiding in the presence of an undercut below the wall, in which the filaments are redirected back into the region between the channels once they climb the wall. Figures (a) and (b) were adapted from Agarwal and Hess[14] with permission from Elsevier. (c) Surface topography can be revealed using microtubules that move randomly on the surface in a time-integrated image. Figure adapted from Hess et al.[146] and reprinted with permission from American Chemical Society © 2002. (d) Quantitative information of topographical features using the kinesin-MT system can be obtained by fluorescence-interference contrast (FLIC) wide-field microscopy. Figure adapted from Kerssemakers et al.[138] with permission from John Wiley & Sons, Inc.

Topographical features also enabled the probing and characterization of surfaces using MT-Kinesin biomolecular system. For instance, fluorescent MTs randomly sampled a topographically structured surface that consisted of elevated portions. Hundreds of fluorescence images were successively acquired and overlaid to reproduce the surface, which resulted in dark spots where MTs did not pass over the elevated portions of the surface[146] (Figure 2.4c). Additionally, using fluorescence-interference contrast wide-field microscopy (FLIC), reproduction of the surface topography using these molecular shuttles was achieved[138]. FLIC microscopy uses interference effects from excitation and emission light, and in this case, enabled height information with nanometer resolution for fluorescent MTs situated above the reflecting silicon oxide surface, further allowing for imaging in three dimensions to reconstruct the surface. In this study, MTs propelled by kinesin motors cross shallow and deep pits. At high motor densities, the trajectories of MTs enabled the reproduction of surface topography from fluorescence intensities (Figure 2.4d), providing an alternative to macroscopic cantilever probes of scanning force microscopes[14,138].

Surface chemistry to guide the molecular shuttles

Patterns in motor density and/or functionality created through surface chemistry patterns on layers that support adsorption of motor proteins provided an alternative to physical barriers that forced filaments into a desired direction. Such patterns enable the biasing of the Brownian motion of the filament tip in the direction of the track, shown in Figure 2.5a. Here, an overhanging filament tip emerges due to lack of attachment to a motor when the filament reaches the region that is motor-free or has inactive motors. The tip at this point either grows in length until it detaches from the surface, or it bends back to the motor-rich area as a result of Brownian motion[14]. If the filament is held by a motor at the edge of the region, the likelihood of the filament returning to motor-rich area is very high because it can swivel around the motor axis[91]. Additionally, a small approach angle of the filament, as well as low filament stiffness, enable the return of the filament tip to the track[14,133,134]. It is however important to point out that although patterns in kinesin density and/or functionality are achieved, a major challenge is the requirement of a casein coating layer for the motility assay, which can inevitably shield kinesin from the surface. One solution to this problem was to support MT motility through a variety of surfaces, for example, non-fouling coating that aid in suppressing the adsorption of both casein and kinesin[133,147].

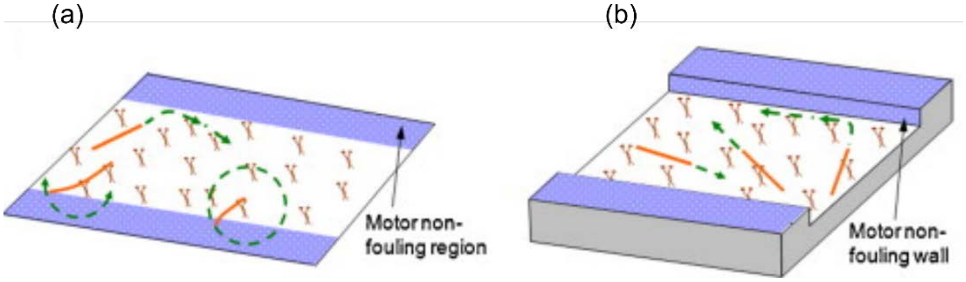

Figure 2.5. Guiding of molecular shuttles using surface chemistry and the combination of surface topography and chemistry. (a) Guiding of microtubules using surface chemistry was achieved by generating contrasts in motor functionality between two regions. Once the MTs crossed the track edge, an overhanging MT tip emerges that fluctuates due to thermal forces until it binds to a motor in the motor-rich region. MT bound to motor at the edge can rotate more freely since motors can swivel around their axis. (b) Guiding using the combination of surface chemistry and topography, in which the walls can interfere with binding or functionality of motors, and filaments are redirected at small approach angles along the walls. This combination makes this guiding approach more reliable as compared to surface topography or surface chemistry alone approaches. Figure adapted from Agarwal and Hess[14] with permission from Elsevier.

Further, biotinylated kinesin motors have been attached to biotinylated self-assembled monolayers (SAMs) through specific interactions, where SAMs were attached to nanometer-scale gold lines within walls of micrometer-sized chambers. The biotinylated kinesin motors attached to the SAMs through the direct interaction between streptavidin and intermediate layers of biotinylated albumin. In this case, the protein multilayer consisting of biotinylated BSA were used to enhance the number of available biotins to bind the kinesin motors, as well as limit the MT gliding to the tracks on the walls of the chamber[148]. Additionally, kinesin tracks have been formed using filaments as stamps to bind and transfer kinesin motors to planar surfaces. Once motors were deposited on surface and released the filament templates, nanometer wide tracks of motors were left behind enabling the binding and propelling of filaments in either direction of the tracks[14,149].

Guiding using the combination of surface topography and chemistry

Early on, it was evident that issues with surface and chemical topography would arise, and were indeed reported[14]. Topographical confinement still allowed for kinesin attachment to sidewalls, further enabling filaments to climb the sidewall and escape. With chemical confinement, filaments that crossed the boundaries would detach from the surface due to lack of redirection of filament motion by a wall[25,27]. Such outcomes are problematic, as it is evident that there would be loss of filaments in both cases, especially due to strong dependency on approach angle of filaments to the boundary, as well as filament stiffness[133]. One possible solution to overcome these issues was to combine both chemical and topographical confinement (Figure 2.5b), and to limit motor attachment to the bottom surface (glass) of the guiding channels [14].

The newly integrated guiding approach was first demonstrated by constructing non-fouling channel walls using Triton X-100 (nonionic detergent)[143]. Further, non-fouling channel walls were also constructed using pluronic F108 physioadsorbed onto hydrophobic SU-8 or fluorosilane coated walls[133,150]. Further, guiding was also achieved on gold patterns, that were also functionalized with poly(ethylene glycol) chains, where patterns were etched into SiO_2 surface[151].

Cargo loading and unloading

The ability to load cargo onto cytoskeletal filaments has been successfully achieved, in which recent developed techniques have been integrated into many device applications. Here, we briefly discuss the importance of cargo loading and unloading on these molecular shuttles and their implications in nanotechnological applications.

In vivo, specifically vesicle transport in neurons, kinesin can bind to vesicle transmembrane proteins either directly or through a scaffold protein [28]. These specialized scaffolding proteins create a connection between the kinesin tail, which is well adapted to grasping cargo, and the specific cargo[14,152].Reproducting specialized scaffolding proteins, however, is not an easy task to replicate *in vitro*, due to limited information and difficulty of reconstituting the system for cargo binding[28]. Ideally, a specific and reversible yet strong connection between transporter and cargo is desired, and this has been achieved using the gliding geometry discussed previously. The gliding geometry made it possible through different engineered approaches to connect and disconnect from various types of cargo, while also offering durability and the ability to adapt to different types of cargo without interfering with gliding motion of filaments[14,27].

MTs tend to have advantages in the aspect of cargo loading as opposed to other filaments such as actin filaments. MT's with suitable polymerization conditions that end up with 13 protofilaments tend to align parallel to the microtubule axis and do not rotate while being propelled by kinesin motors, as opposed to the axial rotation of actin filaments, which has been proposed to interfere with the actin-myosin interactions[14,53,153,154].

The first reported cargo attachment to kinesin-propelled biotinylated MTs was achieved by attaching streptavidin-coated polystyrene microspheres[27]. Then other methods of attachments followed using avidin[155], streptavidin-coated quantum dots[156], ferritic particles[157], DNA[158–161], and carbon nanotubes[162]. However, MT conjugation with different cargo before being introduced into the flow cell posed a problem, as the functionalized filaments were unable to bind to the surface-adhered motors[14,27,155–157]. One solution to this problem was to define cargo binding and motor binding regions in which the filaments were biotinylated in segments[14,156,163].

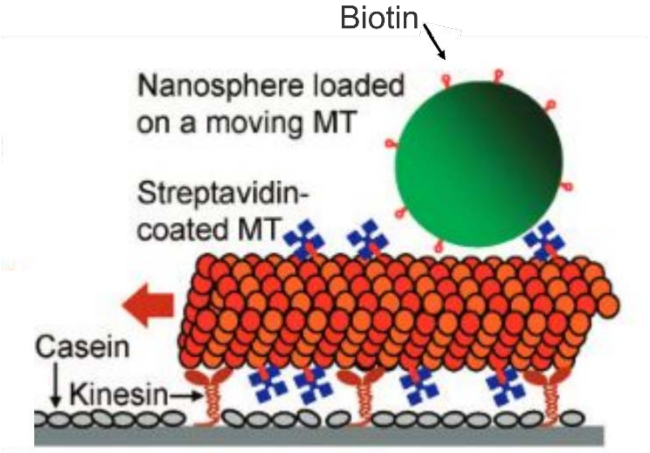

Figure 2.6. Cargo loading. Biotinylated microtubules coated with streptavidin can attach to biotinylated cargo, such as biotinylated polystyrene nanospheres (~ 40 nm diameter), as the microtubules are translated by surface-bound kinesin motors. Figure adapted from Agrawal et al.[164].

Cargo can be conjugated to filaments through covalent or non-covalent chemistries. However, non-covalent attachment techniques (ex. antibody/antigen bonds) are preferable due to selectivity and reversibility. The strong non-covalent interaction of biotin and streptavidin is very commonly used due to the commercial availability of biotinylated filaments, and hence, has been extensively integrated into molecular shuttle systems[14]. Additionally, cargo can be attached to filaments bound to surface-adhered motors through buffer exchanges. This technique aided in determining attachment kinetics of streptavidin to biotinylated MTs, as well as size and concentration of different types of cargos, which inevitably became critical in active self-assembly applications of these filaments[14,32,33,165–169].

Cargo loading without the biotin/streptavidin functionalization has also been accomplished by antibodies attached to the filaments[166,170]. Additionally, double-antibody-sandwich enabled cargo loading of cowpea mosiac virus (CPMV) onto moving shuttles has been used, which inspired multi-analyte assays and biosensor applications of the biomolecular system[171–173].

Cargo unloading would also be beneficial because it would allow for cargoes to be transferred between different stations, and the shuttles could be used multiple times[174,175]. Since unloading would require breaking the bond between the cargo and shuttle, it is vital to do so in a controlled manner because such force will inevitably test the integrity of the polymer structure. Various mechanisms can be employed to unload the cargo including the release of certain chemicals and enzymes, changes in pH, DNA, and even UV-light[28]. For instance, MTs conjugated with malachite green demonstrated the ability to capture and release malachite green aptamers simply by adding excess malachite green to the motility solution[176].

Nanomaterials assembly

Self-assembly is the process in which components spontaneously organize and form structures, either through passive or active assembly processes.[167,177–180] Passive self-assembly uses thermal fluctuations to move components into place through diffusive processes. Although this process is highly parallel, and therefore fast, diffusion is slowed down with increasing particle size, and the mismatch between interaction and thermal energies hinders accuracy of the process[1,180]. On the contrary, active self-assembly uses non-thermal energy to transport the isolated components, and as such, has captured much interest to build structures not easily attained through traditional passive self-assembly or fabrication methods. Active-self-assembly offers many advantages over passive, such as harnessing external sources of energy to overcome the speed limitations of diffusion-driven "passive" assembly to move parts, resolve mismatched connections, and form non-equilibrium structures.[1,167,177,179–181]

Molecular shuttles have shown promising applications in terms of the assembly of nanoscale and microscale components into larger structures. Active self-assembly driven by molecular motors has been shown to offer many advantages such as faster assembly time, assembly of larger building blocks into large complex structures, and most importantly, allows for structure assembly not easily attainable through diffusion-driven self-assembly processes[167,180]. In the following sections, we review the types of structures attained using molecular motor-driven self-assembly.

Bundles and network structures

Active transport of kinesin motors adhered to a surface in a gliding assay leads to collisions between biotin and streptavidin functionalized MTs[182]. The propelled MTs collide with each other, align and subsequently non-covalently crosslink to one another. Such collisions ultimately lead to bundles composed of several filaments (Figure 2.7), which vary in length depending on the number of bundled filaments because of the random attachment process. Further, the bundles may grow (in length and thickness) and could result in other structures as the filaments continue to be translated in the flow cell.

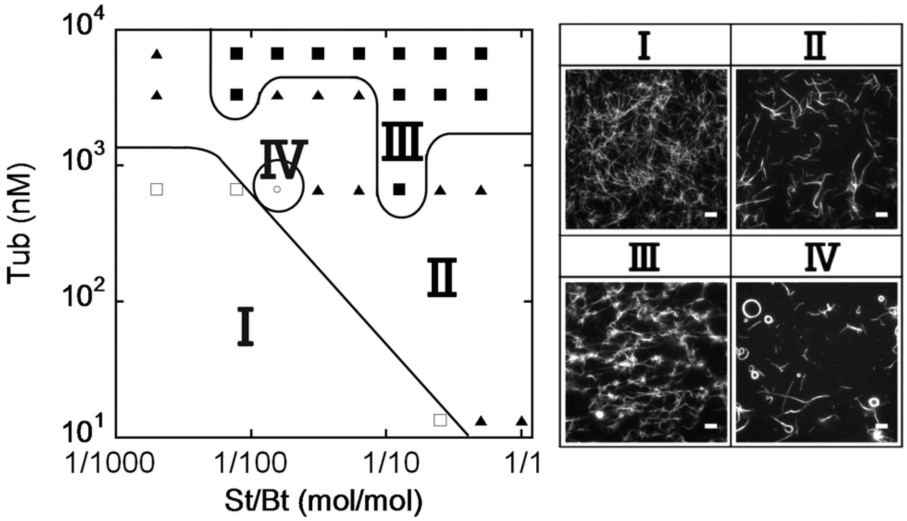

Figure 2.7. Phase diagram for the morphology of self-assembled microtubule structures as a function of cross-linker ratio (streptavidin/biotin or St/Bt) and tubulin concentration (Tub). I-IV (left) represent the varying morphological phases of assembled structures depending on the ratio of St/Bt and Tub ratios, consisting of single MT phase (I), bundle phase (II), network phase (III), and ring structures (IV), with corresponding fluorescence microscopy images (right). Scale bars: 10 µm. Figure adapted from Tamural et al.[183] with permission from the Royal Society of Chemistry.

MT bundles (or “wires”) have been extensively explored using active self-assembly processes, in which factors such as filament rigidity, density, velocity of MTs, and motor density influenced their formation. For instance, stiffer MTs that were prepared with guanylyl-(α, β)-methylene-diphosphonate (GMPCPP) resulted in favorable formation of linear bundles. The formation of longer bundles required more building blocks and hence required higher initial density of MTs. Further, the gliding velocity of MTs affected the length of the formed bundles, in which slow MT gliding velocity (0.1 µm s^{-1} compared to maximum gliding speed of ~ 0.5 µm s^{-1}) resulted in the longest MT bundle. Interestingly, some studies showed that higher kinesin densities resulted in longer bundles, however, other studies suggested high kinesin concentration could result in breakage of the MT bundles into shorter linear arrays. In this aspect, there were experimental conditions that were different among the studies which could have resulted in these contradictory results, and therefore, further investigations are essential in the future to determine how motor density might affect the MT bundle size[32,169,180,184–189]. MTs can also join end-to-end to form wires rather than bundles through electrostatic effects, without the aid of molecular motors. However, these wires are not as long as ones created through motor-driven-assembly and tended to form over much longer timescales through diffusion. Further, bundles that formed through electrostatic interactions can be made polar using cross-linkers (e.g. synthetic polymer caring positive charge such as poly (L-lysine)). In the presence of motor proteins, the motile polar bundles showed velocity dependency on the degree of polarity [50,180,185,190–192]. In this case, one major drawback to the active self-assembly of MTs is the inability to implement polarity on MT gliding assays.

Furthermore, osmotically assembled MTs were combined with oligomeric kinesin (two or more kinesin motors bound together), which resulted in structures that resembled the core structure of eukaryotic cilia and flagella. The addition of ATP activated the motors causing the resulting bundles to transition into a nonequilibrium phase that mimicked the wave-like beating of axonemes[45,193,194]. Such structures demonstrate the ability of these systems to self-assemble into functional biomimetic devices that possess molecular motion[45]. Future developments to control the structural manipulation of bundles over many length scales, as well as bundle size and location, may be advantageous to fabrication methods for futures devices, specifically for directed transport of cargo in micro- or nanofluidics[180].

Network structures can also form in the gliding assay at larger values of the ratio of streptavidin conjugated MTs to biotin and high MT density (Figure 2.7). The high streptavidin coverage on MTs enables the motile MTs to bind to each other at isolated points rather than along their lengths, and as such, MTs cannot align[180]. Further, the MT networks that are formed exhibit swarming behaviors and can organize at high and low densities with distances ranging up to several tens of micrometers[180,183]. Additionally, stable MT networks can self-organize by manipulating the interactions (e.g. depletion forces) among neighboring highly dense MTs that lack cross-linking agents[180,195].

Rings and spools

Rings and spools have been of interest due to their ability to transform linear translational motion of motors into rotational motion. Further the ordered arrangement of these structures driven by cross-linking reagents decrease the entropy of the system, even when the filaments are under considerable amounts of strain. Further, such systems enable the self-assembly of non-equilibrium structures in which motors allow access to a store of chemical energy[180]. Great strides have been made in terms of controlling spool features, and these properties will be discussed below.

As mentioned previously, the inverted assay is ideal to construct nanostructures in a bottom-up fashion. Here, we consider structures other than the linear bundles and network structures mentioned above, specifically rings and spools that also arise from the active self-assembly of motor-driven MT filaments[4,168]. A "ring" typically consists of a single filament bundle that cross-links to itself in a closed loop, while a spool forms from multiple filaments that join lengthwise[180].

Gliding MTs in these assays adapt tightly bent or buckled configurations in which their radii of curvatures far exceeds the natural curvature of free, fluctuating MTs[45,196,197]. MT's persistence length is on the order of millimeters, and therefore, are under considerable strain, storing of up to 10^5 k_BT of bending energy[4]. The strain induced by the surface-adhered kinesin motors enable non-equilibrium, nanoscale structures to actively self-assemble. For instance, nanospools and nanorings can self-assemble from biotinylated MTs that are translated by kinesin motors in the presence of streptavidin or streptavidin-coated nanoparticles[31,32,35,168,169,184,192,198–200] (Figure 2.7 and 2.8). Such phenomena occur due to the collective work of kinesin motors that overcome the bending energy of such stiff filaments, which also results in the polar alignment of overlapping MTs by breaking opposed contacts between mis-oriented MTs[45].

It has been suggested through various studies that the small radii of MT spools are a result of strain-relaxation of cross-linked MTs into helices, closed loops, or pinning of MTs due to defects, as opposed to thermal fluctuations[168,180,189,192,201,202]. Pinning has been shown to result in the tightest spools due to motor proteins exerting force on the MT that results in buckling of the stiff MT. Further, it has been suggested that pinning is the dominant mechanism for the initiation of MT spooling which determines the size distribution of the spools[189]. However, Vandelinder et al. have recently demonstrated the earliest events (nucleation) that drive subsequent nanocomposite assembly, and identified the dominant mechanism to be collision events between crosslinked gliding MTs when photoinduced inactivation of kinesin motors is minimized[31]. Here, three events were observed: pinning, collisions, and induced curvature. Pinning occurs when two MTs bundle together and form a spool when the leading tip becomes pinned by a dead motor. Collisions are driven by multiple MTs that collide and eventually form a spool. Induced curvature occurs when a bundle of MTs travel in a persistent curved trajectory until the ends interact and form a closed spool. These formation mechanisms affected the inner diameter and rotation direction of the resultant rings and spools. Pinning resulted in the smallest average ring diameters (~2.7µm), collisions resulted in intermediate diameters (~ 6.2 µm), while induced curvature resulted in the largest inner ring diameters (~ 32 µm), and all showed bias of rings rotating counterclockwise.

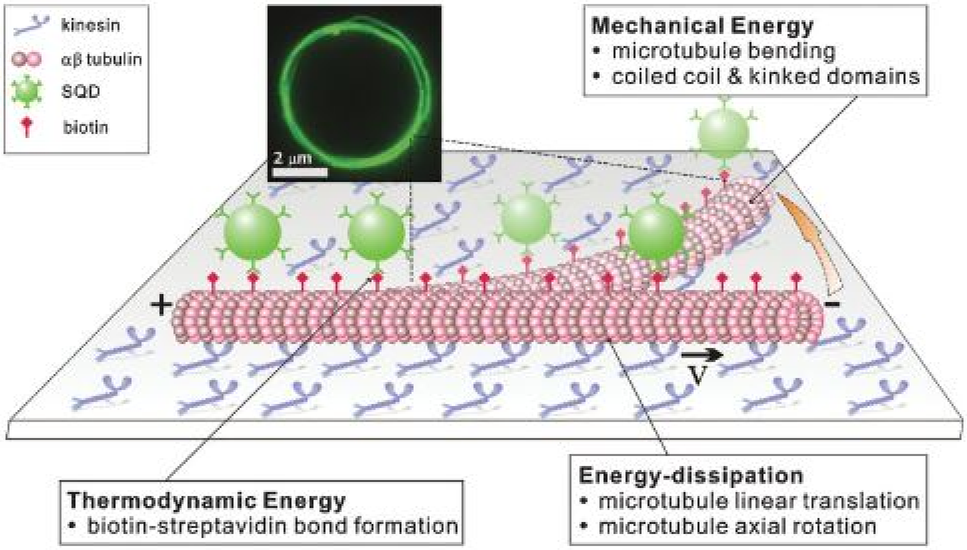
kinesin
αβ tubulin
SQD
biotin
2 μm
Mechanical Energy
• microtubule bending
• coiled coil & kinked domains
+
-
v
Thermodynamic Energy
• biotin-streptavidin bond formation
Energy-dissipation
• microtubule linear translation
• microtubule axial rotation

Figure 2.8. Assembly of nanocomposite spools. Surface-adhered kinesin motors attach and translate biotinylated microtubules with attached streptavidin-coated quantum dots (sQDs). Kinesin motors dissipate chemical energy by ATP hydrolysis, along with linear translation and axial rotation of the microtubules. The introduction of sQDs into the gliding assay introduces thermodynamic energy into the system, resulting in biotin-streptavidin non-covalent bonds. The bending of the microtubules stores mechanical energy, along with formation of collided coil and kinked domains within the assembled nanocomposite structures. figure adapted from Liu et al.[168] with permission from John Wiley and Sons, Inc.

The motor-assembled MT nanocomposites in the presence of streptavidin-coated nanoparticles (Figure 2.8) have shown invaluable materials properties in which: 1) stored elastic energy of the spools can exceed 33,000 k_BT, and 2) MTs with twisted protofilaments (i.e. any MT that has more or less than 13 protofilaments) mechanistically drive ring formation[45,168]. Depending on assembly conditions, specifically during self-assembly of tubulin dimers into MTs, the number of protofilaments can vary in which 12- and 14- protofilaments MTs possess right- and left-handed supertwists, respectively[203]. Since kinesin motors follow along the protofilament's axis, MTs that possess 12- or 14- protofilaments transported by surface-bound kinesin motors result in axial rotation with respect to the direction of the supertwist. Further, it has been shown that during the assembly process of nanospools, adjacent MT filaments form strained coiled-coil domains that follow the oligomerization of MTs that contain a supertwist[45,168]. The supertwist of the MTs enables the control of rotational direction of the rings and spools, in which the rotation of the rings can bias clockwise (right-handed twist) or counterclockwise (left handed twist).[168,169,180,199,202,204] Length and rigidity of the MTs along with the type of kinesin motor used in the flow cell have been shown to affect the rotational direction of the nanocomposites[205]. Further, controlling the thermodynamic contribution and rate of energy-dissipation, and microscale confinement further allows for modulating assembly of such structures[35,45,168,198].

Characteristic features of the spools have been shown to be controlled through motor density, length and rigidity of filaments[180,189,192,205,206]. For instance, higher motor densities resulted in tighter spooling of MTs, while stiffer MTs prepared with GMPCPP resulted in larger diameters. Further, longer MTs resulted in larger spool diameters. The successive addition of MTs in stages into flow cell enabled the tuning of spool thickness (characterized by the difference between the outer and inner diameter of the spool)[200].

Rings and spools are not limited to crosslinked agents as described above, but rather can self-organize transiently (driven by continuous flow of energy rather than active assembly that uses energy flow to form the structures) into rings, spools and vortices by interactions with neighboring filaments at high filament densities[201,207]. MT rings and spools can also form at air-buffer interfaces without the crosslinking agents streptavidin and biotin, relying upon the hydrophilicity of the protein surface to cause the MT to curve away from the air-buffer interface. Such structures formed at the air-buffer interfaces, however, tend to have smaller circumferences and narrower size distributions as compared to spools created in traditional flow cells.[180,204]

Conclusions

The integration of biomolecular transport systems (e.g. kinesin-MT) into artificial environments enables the advancement of nanotechnology. Particularly, the unique characteristics of these motor proteins prove to be an excellent template for nanoscale transport in cells, and hence, makes them ideal to be used in many nanotechnological applications involving motor-driven self-assembly and transport. The incredible capacity of biomolecular motors to achieve the efficient conversion of chemical energy into mechanical work motivates their integration into nanoscale devices. Although the incorporation of these motor proteins into useful technological devices is still limited, our growing understanding of their biophysics allows for their use as nanomachines, and the ability to produce and modify them on a large scale enables their integration and assembly of functional devices. With the current advanced techniques and tools, a variety of mechanisms to demonstrate cargo loading (e.g. biotin and streptavidin), as well as guiding of these molecular shuttles through patterned physical and chemical surfaces have been studied. Moreover, motor protein-based transport enables the dynamic self-assembly and organization of non-equilibrium nanostructures with emergent behaviors (e.g. self-healing) through the dissipation of chemical energy.

Chapter 3

How building block composition affects the active assembly of microtubule spools

Haneen Martinez, [a] Virginia VanDelinder, [a] Zachary Imam,[a] Erik D. Spoerke,[b] and George D. Bachand *[a]

[a] Center for Integrated Nanotechnologies, Sandia National Laboratories,
Albuquerque, NM USA
[b] Electronic, Optical, and Nano-Materials, Sandia National Laboratories,
Albuquerque, NM USA

This chapter is a draft of a manuscript submitted to Nanoscale.

Abstract

Defects can determine and influence various properties of materials, and many technologies rely on the manipulation of defects (e.g., semiconductor industries). Defect management is a survival mechanism in many biological organisms (e.g. DNA repair), which has inspired materials scientists to design artificial nanomachines that mimic the ability to detect defects and repair damage. Biological motors have captured considerable attention in developing such capabilities due to their ability to convert chemical energy into directed motion in reponse to environmental stimuli, which maximizes their ability for detection and repair. The objective of the present study was to develop an understanding of how chemical and structural heterogenities (defects) in building blocks affect the kinesin-driven, active assembly of microtubule (MT) spools. Segmented MT building blocks were formed through an annealing process that resulted in alternating, micron-scale bonding (i.e., biotin-containing) and non-bonding (i.e., biotin-free) domains. Here, the introduction of these MT building blocks that contain non-bonding domains into a kinesin gliding motility assay along with streptavidin-coated quantums resulted in the active assembly of spools with altered morphology but retained functionality. Moreover, it was noted that non-bonding domains were autonomously and preferentially released from the spools over time, representing a mechanism by which defects may be removed from these structures. Overall, our findings demonstrate that this active assembly system employs quality control mechanisms to overcome constraints caused by

defects in the building blocks, which can be potentially expanded to a wide range of applications such as material self-regulating and the healing active materials.

Introduction

Defects represent disruptions or interruptions of order, structure, or homogeneity in a material. They are found in nearly all materials to varying extents, and the nature and behavior of defects can dramatically impact materials properties and performance. For example, n-type and p-type dopant “defects” in silicon semiconductors provide the critical electronic properties fundamental to modern microelectronics.[208,209] Oxygen defects in ceramic oxides impact ion transport properties key to solid oxide fuel cells.[210] Inclusions can degrade optical properties in glasses, while metallic dopants in alumina give rubies their vibrant color.[211] Dislocation densities and metal carbide inclusions in steel can drastically affect its strength and robustness, which is why annealing or hot working (e.g., forging) is used to redistribute, segregate, or remove defects and impurities from metals.[212] Although the influence and dynamic behavior of defects is often considered in these types of structural and technological materials, relatively little attention has been given to defects in bio-inspired supramolecular materials.

Biological organisms have evolved into highly-optimized functional systems, displaying remarkable abilities such as self-regulation and self-repair in the presence of defects or damage, further increasing the organism’s lifetime. Such tasks require the cells to respond to stimuli in their environment, and most importantly, to convert chemical energy into mechanical work.[213–216] In the cell, kinesin motors harness the energy from ATP hydrolysis to actively transport intracellular components (e.g., vesicles, chromosomes) along cytoskeletal networks composed of microtubule (MT) filaments, with high efficiency

(~50%).[28,45,217–219] Such intriguing cellular functions inspired researchers to create nanomachines capable of mimicking and/or co-opting biological materials for the development of dynamic, synthetic materials.[220,221] Because biomolecular motors offer the ability to respond to different environmental stimuli through their regulated collective movement, they are of prime interest as a template in developing nanomachines that could sense defects and repair damage.[216,222–227] Other researchers have sidestepped the problem of creating nanomachines by using kinesin motors for many *ex vivo* applications, such as powering novel analytical, diagnostic, and computational devices,[2,68,173,228] as well as driving active self-assembly of non-equilibrium, nanostructured materials.[29,30,45,68]

To date, the possibility of using kinesin motors to repair defects in *ex vivo* materials has not been explored. MTs, however, are able to self-repair mechanically induced defects in the tubulin lattice through the incorporation of tubulin subunits from solution.[50,229,230] Although this ability demonstrates the robustness of the MTs *ex vivo*, much less is known about the formation and effects of defects in dynamic and active self-assembly materials involving the kinesin-MT transport system. One example of kinesin-driven active self-assembly involves the formation of rings and spools, where a ring is defined as single filament that cross-links to itself to form a closed loop, and a spool consists of multiple filaments that join lengthwise. [4,29–33] In this system, biotinylated MTs serve as the fundamental building blocks, and the binding of streptavidin or streptavidin-coated quantum dots (sQDs) drives their spontaneous assembly into rings and spools. While serving as an interesting model of active assembly, the formation of rings and spools may also be used as a sensing element. For example, label-free detection of microvesicles was recently reported based on the formation of spools.[231]

While fluorescent imaging suggests that the spools are well-ordered, electron microscopy reveals that these structures are topographically and morphologically diverse including twisted and kinked domains, as well as in-plane and out-of-plane loops.[35,168] These observations suggest spools can tolerate a certain level of structural heterogeneity, but the question remains as to whether they can compensate for MT building blocks that have large (e.g., micron-scale) domains that lack biotin and are unable to bind sQDs. The large number of biotin-streptavidin bonds that are formed among MTs and sQDs during assembly is critical to stabilizing the high bending energy (~30,000 kT per turn) stored in these structures.[168,198,232] As such, the tolerance of active assembly and the resulting spools should be strongly dependent on the relative size and frequency of the domains that lack biotinylated tubulin.

To test this hypothesis, we characterized the active assembly of MT spools using MT building blocks composed of varying lengths and frequency of “bonding” and “non-bonding” domains. Herein, we define bonding domains and MTs as those containing biotinylated tubulin and therefore “compliant” in their ability to form biotin-streptavidin bonds. In contrast, non-bonding domains and MTs are defined as those polymerized in the absence of biotinylated tubulin and thus represent “defects” due to their inability to form biotin-streptavidin bonds. Using these MT building blocks, we observed the incorporation of bonding and non-bonding domains and MTs into spools, but also the preferential removal of non-bonding domains and MTs from spools over time. We hypothesize that this phenomenon is related to the inability of these domains and MTs to balance high bending energy with covalent bond formation, as well as mechanical strain due to mismatches in kinesin motor velocities. Overall, this work provides new insights into the influence and behavior of defective building blocks in dynamic supramolecular materials that may have important implications for the future engineering of self-regulating and "healing" nanomaterials.

Materials and Methods

Lyophilized unlabeled tubulin, Hilyte Fluor 488 (Hilyte 488) labeled tubulin, aminomethyl coumarin acetate (AMCA) labeled tubulin, and biotin labeled tubulin purified from porcine brain were purchased from Cytoskeleton Inc. (Denver, CO) and used according to manufacturer's instructions without further modification or purification. Streptavidin conjugated quantum dots (sQDs, 655nm) were purchased from ThermoFisher Scientific (Waltham, MA). All chemicals were purchased from Sigma Aldrich unless otherwise noted.

Preparation of motor proteins

Full-length *Drosophila melanogaster* kinesin-1 from the pPK113 expression plasmid[98] was expressed in *Escherichia coli* BL21 (DE3) pLysS cells. Briefly, when the culture reached an OD_{600nm} of ~0.7, protein expression was induced through the addition of 0.5 mM isopropylthio-β-galactoside (IPTG). Cells were harvested by centrifugation at 9000×g, and lysed using BugBuster® with Benzonase® (EMD Biosciences, Inc., Billerica, MA) and 100 mM AEBSF (4-(2-

Aminoethyl) benzenesulfonyl fluoride hydrochloride (Sigma-Aldrich Inc., St. Louis, MO). Kinesin was then purified by Ni-NTA chromatography as previously described[98,156]. Protein concentration was determined by standard bicinchoninic (BCA) assay to be 4 µM. Aliquots of the protein were snap frozen in liquid nitrogen and stored at -80°C.

Preparation of Microtubules

Fluorescent, biotinylated, and unlabeled MTs were prepared by resuspending lyophilized tubulin in BRB80 buffer (80mM PIPES pH 6.9, 1 mM $MgCl_2$,1 mM EGTA) containing 1mM GTP and 10% glycerol to a final tubulin concentration of 5 mg ml^{-1}. AMCA labeled tubulin was combined with biotinylated and unlabeled tubulin at a molar ratio of 1:1:2, respectively, for both experimental and control population of 0% defects. Hilyte 488 tubulin and unlabeled tubulin were mixed at a molar ratio of 1:1 for experimental and control population of 100% defects. MTs were polymerized at 37 °C for 30 minutes and stabilized against depolymerization using BRB80 solution containing 10 µM paclitaxel for a final tubulin concentration of 0.1 mg ml^{-1}. Segmented MTs were achieved by mixing biotinylated AMCA MTs with Hilyte 488 MTs at the following defect percentages: 20, 33, 50, 66, and 80. All populations mixed at different percentages, as well as the control population were incubated at room temperature for two days to allow for sufficient fusion.

Motility assays

Inverted kinesin motility assays were performed by constructing a capillary flow cell on a glass slide using double-sided tape and a coverslip, with average channel dimension of ~20 mm long, 5 mm wide, and 0.2 mm deep. Kinesin was diluted to 8 nM in 80mM PIPES with 2 mg mL^{-1} casein and 2 mM adenosine 5′-(β,γ-imido) triphosphate (AMP-PNP), a nonhydrolyzable form of ATP used to immobilize the MTs. This solution was added to the flow chamber and incubated for 5 minutes. The flow cell was then washed using motility solution (BRB80 containing 0.2 mg mL^{-1} casein, 1 mM AMP-PNP, 0.02 mg mL^{-1} glucose oxidase, 0.008 mg mL^{-1} catalase, 20 mM D-glucose, and 1 mM DTT) to remove unbound motors. Paclitaxel stabilized MTs diluted in motility solution were infused into the flow cell and incubated for 5 minutes to allow MTs to bind to the kinesin coated surface. The flow cell was washed with motility solution to remove any unbound MTs. sQDs were diluted to a final concentration of 10 nM in motility solution as described above except substituting 1 mM ATP for AMP-PNP to facilitate MT mobility, and supplementing with 1 mM Trolox to optimize photoprotection[233]. The sQD solution was added to the flow chamber and incubated for 5 minutes to allow sufficient sQD attachment to the biotinylated MT segments, followed by several wash steps using motility solution containing ATP to remove excess sQDs.

Fluorescence Microscopy

The flow cells were mounted on an Olympus IX-71 inverted fluorescence microscope equipped with a 100 W mercury fluorescence lamp (Osram) and an ORCA-3CCD digital camera (Hamamatsu). Olympus filter sets U-MWU2 (AMCA), U-MWIB3 (488 fluorophores), and Chroma dual-band filter set U-N51009 (simultaneous visualization of 488 fluorophores and sQD 655) were used. Fluorescence images were acquired using 60× and 100× oil immersion objectives. Image processing and tracking of ring formation were performed in Fiji[234]. Lengths and number of MTs were measured before and after the addition of sQDs using the Neurite Tracing function[235] in Fiji. Statistical analyses and plotting were performed using SigmaPlot 13.0 (Systat Software, San Jose, CA).

Calculation of fraction defect MTs in spools

The expected fraction of non-bonding MTs in spools, F_d, (orange line in Fig. 3.3) was calculated by the following. The total length of non-bonding MTs expected in the spools is $L_d = f_d \cdot n_s \cdot \bar{l}_s$, where f_d is the fraction non-bonding in segmented MTs, n_s is the number of segmented MTs, and $\bar{l}_s$ is the average length of the segmented MTs. All of these parameters were measured experimentally for each relative non-bonding level (Fig. A3.2). Similarly, the total length of bonding MTs expected in spools is $L_c = f_c \cdot n_s \cdot \bar{l}_s + n_c \cdot \bar{l}_c$, where f_c is the fraction bonding in segmented spools (f_c=1-f_d), n_c is the number of bonding MTs, and $\bar{l}_c$ is the average length of bonding MTs. Then the fraction non-bonding in spools is $F_d = L_d/(L_d + L_c)$. At low non-bonding MT levels, almost all the non-bonding MTs are in segmented MTs, with very few purely non-bonding MTs. At higher relative non-bonding levels, more of non-bonding domains are in pure non-bonding MTs and fewer are in segmented MTs. For the green line in Fig. 3.3, the ratio of green to red fluorescence intensity in the spools were measured. After background subtraction, the ratio of bonding (red) and non-bonding (green) MTs in spools was calculated using a standard curve generated from the intensity ratios and fraction of non-bonding MT by length.

Results and discussion

The relative ratio of biotinylated (i.e. bonding) tubulin and sQDs regulates the active self-assembly of spools; bonding MTs will form spools at concentrations of biotinylated tubulin as low as 10%,[198] ~160 biotinylated dimers per micron. Consequently, bonding MTs will have small regions free of biotinylated tubulin (i.e., tens of nm), which have a negligible effect on the structural nature of the spools. To more fully understand the structural assembly of the spools, we formed segmented MT building blocks through the directed self-assembly (i.e., annealing) of bonding and non-bonding MTs[50,236,237] at varying ratios.

Two populations of MTs were independently polymerized and subsequently combined together to anneal end-to-end MTs with varying levels of defect (Fig. 3.1a). Bonding MTs (blue) were formed by polymerizing unlabeled, biotinylated, and aminomethylcoumarin (AMCA)-labeled tubulin; non-bonding MTs (green) by polymerizing unlabeled and HiLyte® 488-labeled tubulin. Directed self-assembly yielded annealed, segmented MTs that had alternating bonding (blue) and non-bonding (green) domains (Fig. 3.1b) of varying sizes and frequency. The resulting MTs were introduced into the gliding motility assay (Fig. 3.1c, top), followed by the introduction of sQDs (Fig. 3.1c, middle and bottom) to initiate the active assembly of spools, which were characterized by fluorescence microscopy.

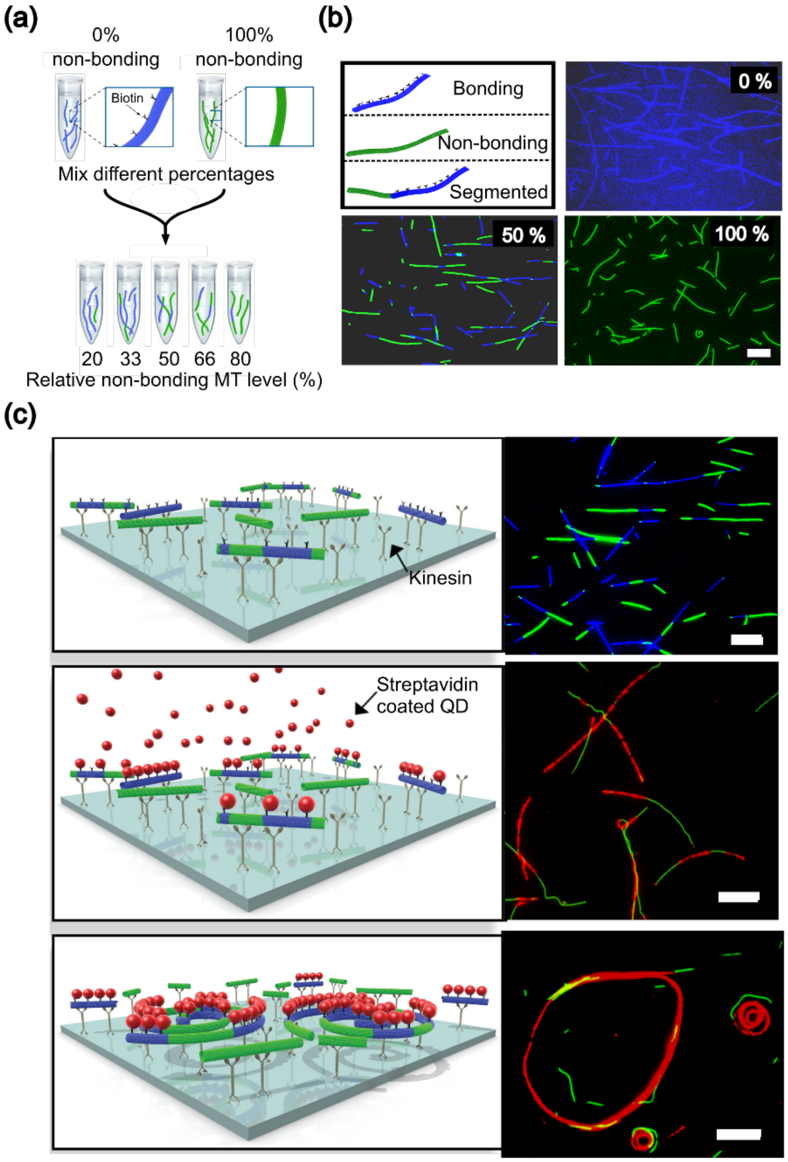
(a)
0%
non-bonding
100%
non-bonding
Biotin
Mix different percentages
20 33 50 66 80
Relative non-bonding MT level (%)
(b)
Bonding
Non-bonding
Segmented
0 %
50 %
100 %
(c)
Kinesin
Streptavidin
coated QD

Figure 3.1. Assembly of spools using segmented MTs. (a) Formation of segmented MTs by mixing various ratios of bonding (blue) and non-bonding (green) MTs. (b) Photomicrographs showing the resulting three types of MTs: blue, bonding MTs, green, non-bonding MTs, and blue-green segmented MTs consisting of bonding and non-bonding domains. (c) Schematic illustration of the in vitro gliding motility assay used to assemble the spools in which surface-bound kinesins translate the MTs (top panel); the addition of streptavidin-coated QDs (middle panel) results in the formation of spools (bottom panel). Scale bars = 10 µm.

The morphology of the spools revealed qualitative changes based on the introduction of MTs containing non-bonding domains. When only bonding MTs were present, the resulting spools generally adopted an oval or circular shape with densely packed MT layers and occasional structural variants in the form of loops and spirals (Fig. 3.2a, 0%), consistent with prior reports.[32,168,169,205] With segmented MTs, the spools adopted more irregular shapes characterized by a decrease in the packing MT density, as well as larger gaps and loops that were primarily associated with non-bonding domains (Fig. 3.2a). We also observed unbound 'tails' consisting of non-bonding (green) domains of the segmented MTs (Fig. 3.2a, 80%). Overall these observations demonstrate the ability of kinesin motors to drive the assembly of stable spools from segmented MT building blocks.

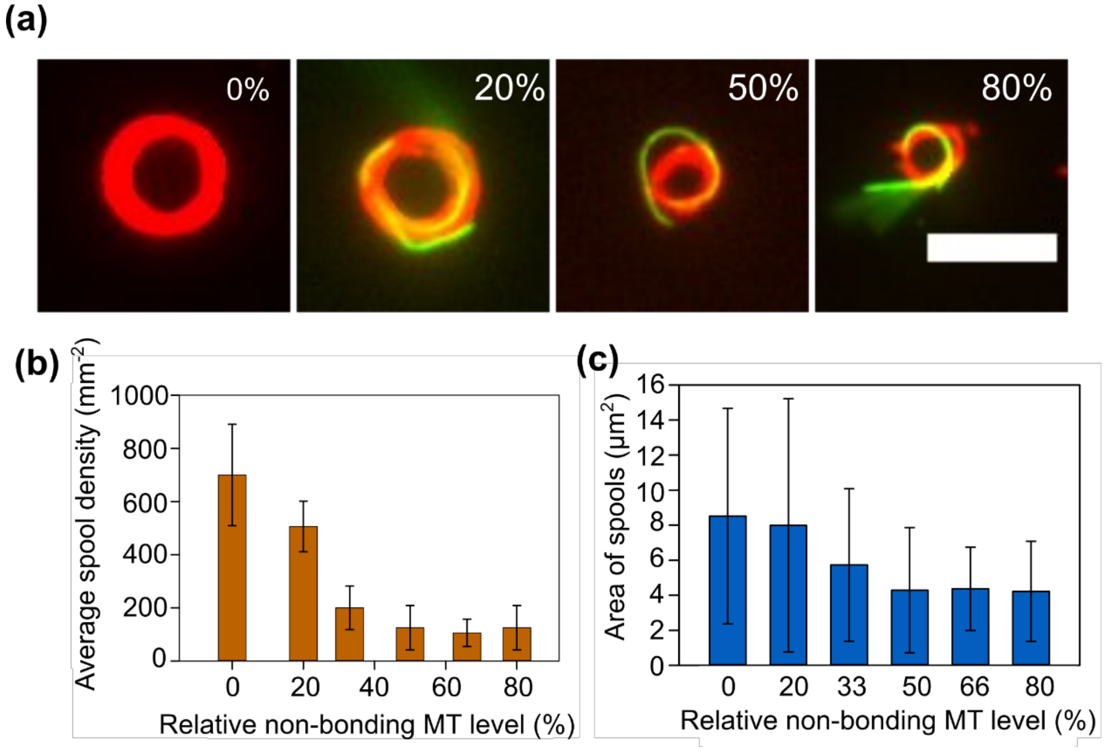

Figure 3.2. Spool morphology and size. (a) Fluorescence micrographs of spools showing structural differences across the different percentages of non-bonding MT domains. Scale bar = 5 µm. Average (b) density and (c) area of spool for different levels of non-bonding MTs. Error bars = standard deviation. Number of measurements (n) used to determine spool density was 10 fields of view for each

treatment; n used to determine spool areas was 98, 101, 44, 29, 20, and 26 for 0, 20, 33, 50, 66, and 80% non-bonding domains, respectively.

We assessed the quantitative differences between the bonding and segmented spools by measuring the inner diameter of MT spools as it is strongly dependent on the nucleation mechanism.[31] The average inner diameters (Fig. A3.1a) formed from bonding and segmented MTs were similar, 2.3 ± 2.2 μm (mean ± standard deviation) and 2.1 ± 1.5 μm, respectively ($P = 0.481$), and suggest that spools formed from both types of building blocks assembled by a combination of pinning and simultaneous collision.[31] The density of spools (i.e., number of spools per area) was also evaluated at 30 min post-introduction of sQDs. Here, a decrease in the density of spools was observed when comparing bonding and segmented MTs, 700 ± 190.5 and 212.5 ± 79.1 spools per mm^2, respectively ($P < 0.001$). Further, the density of spools exhibited an inverse correlation with respect to percentage of non-bonding domains (Fig. 3.2b; $r = -0.895$; $P = 0.02$), which intuitively may be explained by the reduction in bonding domains capable of nucleating the formation of a spool.

The subsequent growth of the spools may be characterized by the thickness and/or area of a spool. These properties are a product of (*i*) the growth process in which colliding MTs are sequentially added to the outer perimeter of the existing spools,[168,200] and (*ii*) the loss of any MTs from the rotating spools. The average thickness of spools (Fig. A3.1b) formed by segmented MTs (0.6 ± 0.3 μm) was smaller than those formed by bonding MTs (0.9 ± 0.4 μm; $P < 0.01$). Further, the thickness of the spools was inversely correlated to the percentage of non-bonding MTs (Fig. A3.1b; *r* = -0.973; *P* < 0.002). The mean area of a spool formed from segmented MTs (6.3 ± 5.8 μm^2) was also smaller than that observed for bonding MTs (8.5 ± 6.2 μm^2; *P* <0.001), and inversely correlated with the percent of non-bonding MTs (Fig. 3.2c; *r* = -0.925; *P* = 0.008). Collectively these results suggest that the presence of non-bonding MTs has an adverse effect on the growth of spools.

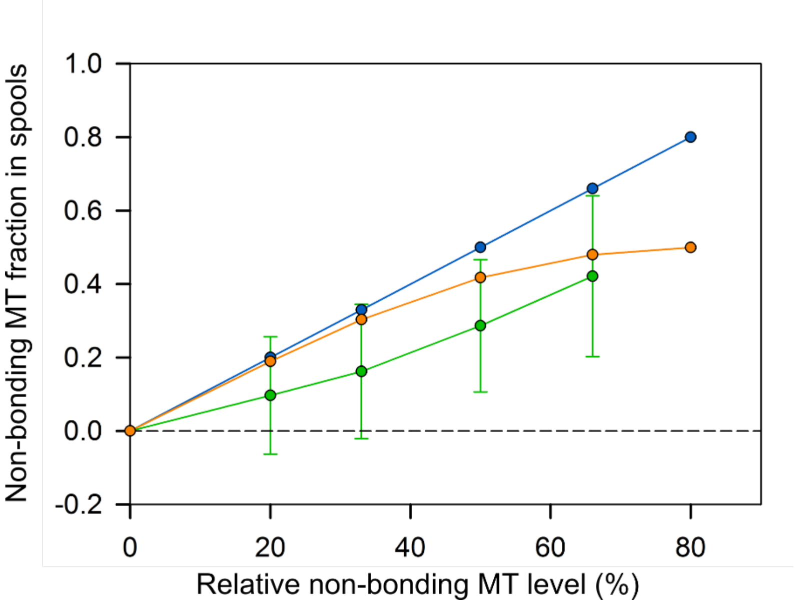

Figure 3.3. Theoretical vs. measured fraction of non-bonding MTs in spools. The blue line shows the fraction of non-bonding MTs that would theoretically be expected in spools assuming that all types of MT building blocks were incorporated at an equivalent rate. The orange line extends this theory with the assumption that only bonding and segmented MTs are incorporated into spools. Here, measured experimental data of the initial MT counts and length distributions were used in the theory to predict the fraction in spools. The green line shows the measured fraction of non-bonding MTs in spools based on fluorescence images Error bars = standard deviation. Note: (80% defects data excluded due to insufficient number of observations and large variability).

Examing the fraction of non-bonding domains and MTs in spools can offer important insights as to how domains that cannot form biotin-streptavidin bonds are managed during the assembly and growth processes. If one assumes that all MTs are incorporated at equivalent rates, the fraction non-bonding domains and MTs expected to be incorporated into spools may be estimated simply by the ratio of the two different MT types (Fig. 3.3, blue line). Because non-bonding MTs lack biotin, it is assumed that their incorporation into spools should be minimal and may be removed from the theory by excluding purely non-bonding MTs (Fig. 3.3, orange line). Here, measured experimental values of number and lengths of non-bonding MTs (Fig. A3.2) were used in the modified theory. These estimates were then directly compared with experimental data in which the fraction of non-bonding MTs in spools was measured via fluorescent intensity at 30 min, (green line; note that data for 80% defects were excluded due to a low number of observations and high variability). Details of these calculations are provided above in the Experimental section. The measured fraction of non-bonding MT in the spools (green line) shows deviation from both the theoretical predictions (blue and orange lines), which may be explained by two potential mechanisms. First, although the segmented MTs can incorporate into spools, the frequency of incorporation may be lower due to the presence of non-bonding domains. Alternatively, the non-bonding domains of the segmented MTs that were initially incorporated into the spools may be broken and released due to the high bending energy in the spool and inability of non-bonding domains to compensate for this energy with stabilizing biotin-streptavidin bonds. In addition, because spools rotate at a constant angular velocity, the kinesin motor transport MTs at different linear velocities depending on where they are in the spool,[198] which can lead to additional strain between adjacent MTs in a spool. The latter hypothesis (i.e., removal of non-bonding domains) is exemplified in Fig. 3.4a, where a non-bonding "tail" is severed from a spool. As these tails are not stabilized through lateral bonding to adjacent MTs, sharp kinks and bends may form as the spool rotates; during such events, the tail segment forms a bend that exceeds the critical radius of curvature (~0.6 μm)[238] at which point the non-bonding domains of the segmented MTs break, and are released from the spool. This behavior is a direct result of the dynamic character of this motor-driven, non-equilibrium system.

Breakage and release of the non-bonding domains of the segmented MTs over time should result in an overall increase in the number of non-bonding MTs moving freely in the gliding motility assay (i.e., green MTs not associated with spools). Thus, the release of non-bonding domains of the segmented MTs may be quantified by measuring the density of unattached defect MTs at various time points (Fig. A3.3a). Indeed, we observed an average increase of ~190% in the number of non-bonding MTs across the different non-bonding MT levels (20-80%) over a thirty-minute period. As shown in Fig. 3.4b, this effect was dependent upon the ratio of non-bonding in segmented MTs, with the greatest increase in density of unattached non-bonding MTs was observed at 20% defects (421% increase), and the smallest increase was observed at 50% defects (86% increase). These data support the hypothesis that segmented MTs are preferentially broken into bonding and non-bonding MTs, and that the non-bonding MTs are disproportionately released from the spools due to the lack of stabilizing biotin-streptavidin bonds. To ensure that the observed increase was not simply caused by random shearing or breakage of MTs, we also quantified the change in length of non-bonding MTs over the same period (Fig. 3.4b and S3b). Here, a ~36% decrease in length was observed for non-bonding

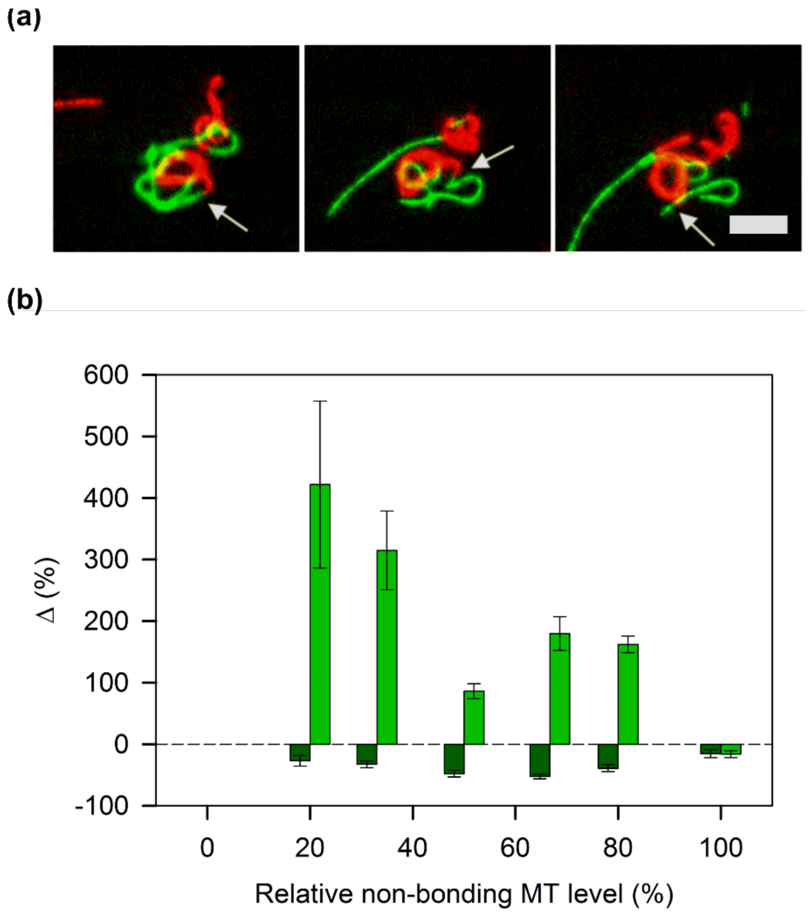

Figure 3.4. Breakage and release of non-bonding MTs. (a) Time-lapse micrographs demonstrating breakage and release of a non-bonding MT domains. Scale bar = 5 µm. (b) Change in average density (🟩) and average length (🟩) of free non-bonding MTs as a function of the relative non-bonding MT level (t= 30 min). Number of measurements (*n*) used are listed in Fig. A3.4 & A3.5. Error bars = propagated standard errors.

MTs (20-80% defect levels). It is likely that non-bonding domains removed from spools experience shortening, as the breakage that releases these domains will not occur solely at the interface of non-bonding and bonding domains, but also in the middle of non-bonding domains. The change in density and length of bonding and segmented MTs was also measured to confirm that the release of non-bonding MTs was indeed preferential, relative to the bonding MTs. These data suggest that bonding and segmented MTs are released from spools, but at a much lower level (Fig. A3.4 and A3.5). Thus, we conclude that defect, non-bonding domains and MTs are autonomously and preferentially removed as part of the active self-assembly of MT spools.

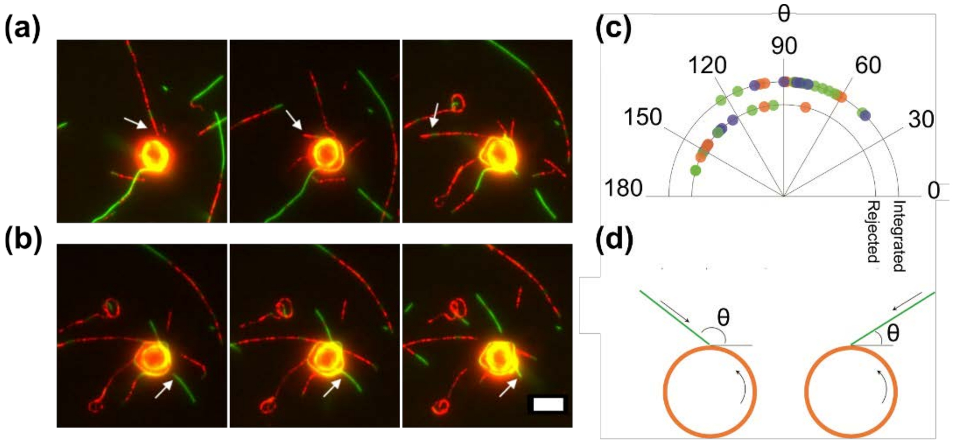

Figure 3.5. Spools integrate or reject MTs upon collision. Time-lapse micrographs showing (a) rejection of bonding MT (red), and (b) integration of non-bonding MT (green) into the spool. Note: the spool is rotating counter-clockwise. Scale bar = 5 µm. (c,d) Collision angles of unattached non-bonding (●),bonding(●), and segmented (●) MTs that integrated into (outer) or were rejected from (inner) spools. d) Diagrams of an MT encountering spools at angle θ greater than (left) and less than (right) 90˚.

We also assessed how non-bonding domains and MTs affected the incorporation of MT building blocks during spool growth. Fig. 3.5a shows an example of a bonding MT being rejected from a spool, while Fig. 3.5b shows a non-bonding MT being incorporated into the same spool. We observed that the collision angle (θ) determined whether an MT building block would either be incorporated into or rejected by the growing spool. Specifically, MTs colliding with rotating spools displayed a significantly greater probability of being incorporated when $\theta < 90°$ ($P < 0.0001$; Fig. 3.5c, d). Incorporation was independent of the MT type; i.e., all three MT types displayed similar rates of incorporation at $\theta < 90°$. While this observation may appear inconsistent with regard to non-bonding MTs, the incorporation of non-bonding MTs into spools is transient and likely results from being sterically trapped in gaps/loops in the spool. Collisions at $\theta > 90°$ largely result in rejection of the MT building blocks due to the shear force generated by MTs moving in opposing directions.

By segregating and eliminating the non-bonding defective domains of the segmented MTs, the energy dissipated during assembly effectively parallels the action of defect annealing or hot-working in metals, where thermal or mechanical energy is used to redistribute or remove defective domains from a material. In effect, the active assembly process is prioritizing functionality, and eliminating MTs that fail to meet the functional standard of this system. Collectively, this knowledge establishes a critical foundation upon which more advanced biomolecular and hybrid nanomaterials may be designed and developed based on active assembly processes.

Conclusions

Here, we described how defect, non-bonding domains in MT building blocks affect the active assembly and behavior of motor-driven MT spools. Active assembly of spools was observed using segmented MT building blocks consisting of alternating bonding (biotinylated) and non-bonding domains with varying lengths and frequencies. Use of these building blocks resulted in spools with altered morphologies, reduced densities, and reduced areas. Moreover, we observed the autonomous and preferential removal of the non-bonding domains from spools over time, which may be attributed to the lack of bond formation necessary to offset the mechanical strain induced during the dynamic rotation of the spools. Furthermore, the ability of free MTs (segmented, bonding, and non-bonding) to incorporate into the spools was shown to be strongly contingent on the collision angle ($\theta < 90°$). Overall, our findings provide fundamental insights into how energy dissipation can be used to regulate the composition of actively assembled structures, particularly with respect to quality control of defective building blocks. These observations will guide future development of nanostructured materials with adaptive and self-healing behaviours.

Conflicts of interest

There are no conflicts to declare.

Acknowledgements

We thank Jacquilyn Weeks and Dr. Brad Jones for their critical review and insightful discussion regarding this paper. This work was supported by the U.S. Department of Energy, Office of Basic Energy Sciences, Division of Materials

Sciences and Engineering (BES-MSE). Kinesin synthesis and fluorescence microscopy were performed, in part, at the Center for Integrated Nanotechnologies, an Office of Science User Facility operated for the U.S. Department of Energy (DOE) Office of Science (User Project 2017AU0006; PI: Martinez). Sandia National Laboratories is a multi-mission laboratory managed and operated by National Technology and Engineering Solutions of Sandia, LLC., a wholly owned subsidiary of Honeywell International, Inc., for the U.S. DOE’s National Nuclear Security Administration under contract DE-NA-0003525. This paper describes objective technical results and analysis. Any subjective views or opinions that might be expressed in the paper do not necessarily represent the views of the U.S. Department of Energy or the United States Government.

Appendix

How building block composition affects the active assembly of microtubule spools

Haneen Martinez, [a] Virginia VanDelinder, [a] Zachary Imam,[a] Erik D. Spoerke,[b] and

George D. Bachand *[a]

[a] Center for Integrated Nanotechnologies, Sandia National Laboratories,
Albuquerque, NM USA
[b] Electronic, Optical, and Nano-Materials, Sandia National Laboratories,
Albuquerque, NM USA

Corresponding Author: George D. Bachand (gdbacha@sandia.gov).

This chapter is a draft of a manuscript submitted to Nanoscale.

Supporting information

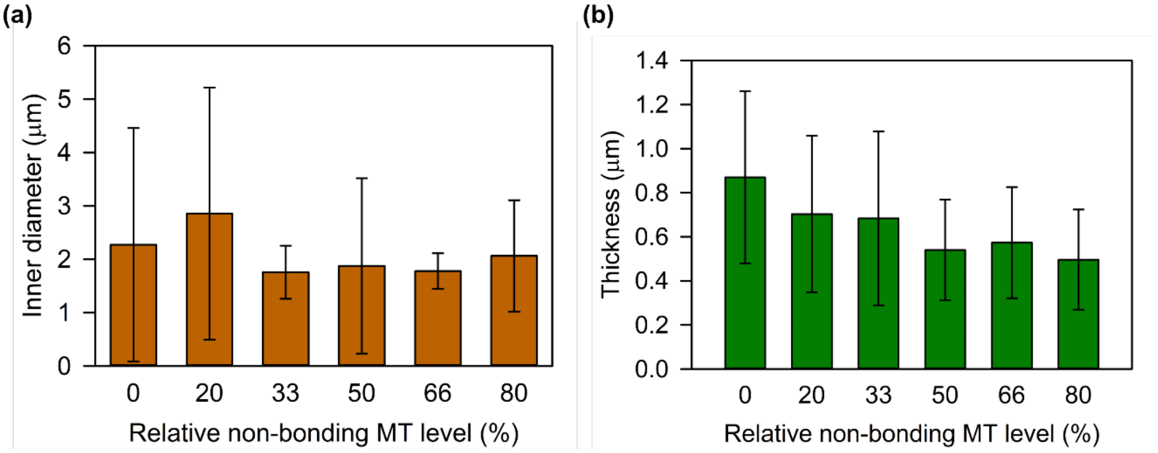

Figure A 3.1. Average inner diameter and thickness of spools. (a) Average inner diameter of spools for each non-bonding MT level. (b) Average thickness of spools as measured by the difference between outer and inner radii. Number of measurements (n) was 98, 101, 44, 29, 20, and 26 for 0, 20, 33,50, 66, and 80% levels of non-bonding MTs, respectively. Error bars= standard deviation.

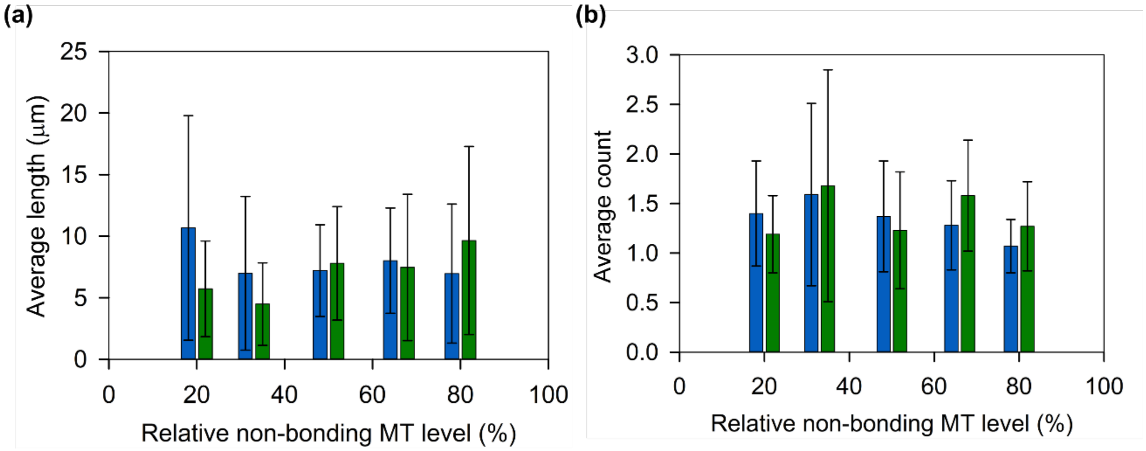

Figure A 3.2. Average length and count of MT domains within the segmented MTs. Average (a) length and (b) count of bonding (blue bars) and non-bonding (green bars) MT domains in segmented MTs as a function of percent non-bonding MT level. Number of measurements for (a): blue bars =80, 70,70, 69 ,81 and green bars=68, 73, 64, 90, 95 for 0, 20, 33,50, 66, and 80% levels of non-bonding MTs, respectively. Number of measurements for (b) for blue and green was 7,44, 51, 56, 76 for 0, 20, 33,50, 66, and 80% levels of non-bonding MTs, respectively. Error bars = standard deviation.

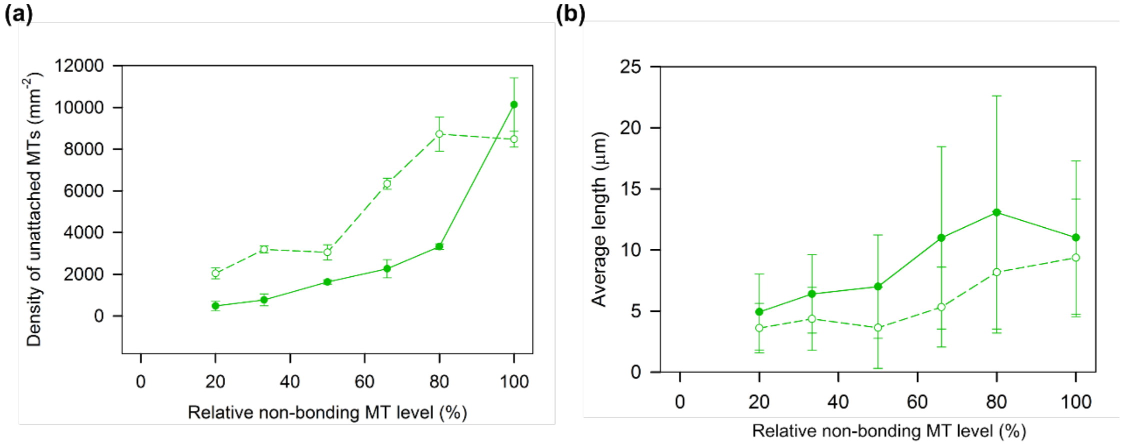

Figure A 3.3. The average density and length of unattached non-bonding MTs (i.e., not in spools) as a function of percent non-bonding MTs. (a) average density and (b) length were measured prior to (solid lines/closed circles, t=0) and after adding sQDs (dashed lines/open circles, t=30min) for non-bonding MTs. Number of measurements for each data point in (a) was 5 images. Number of measurements for (b) was: (i) solid line= 44,74,104,142,111,102; dashed line = 98,104,89,100,108,102 for 0, 20, 33,50, 66, and 80% levels of non-bonding MTs, respectively. Error bars= standard deviation.

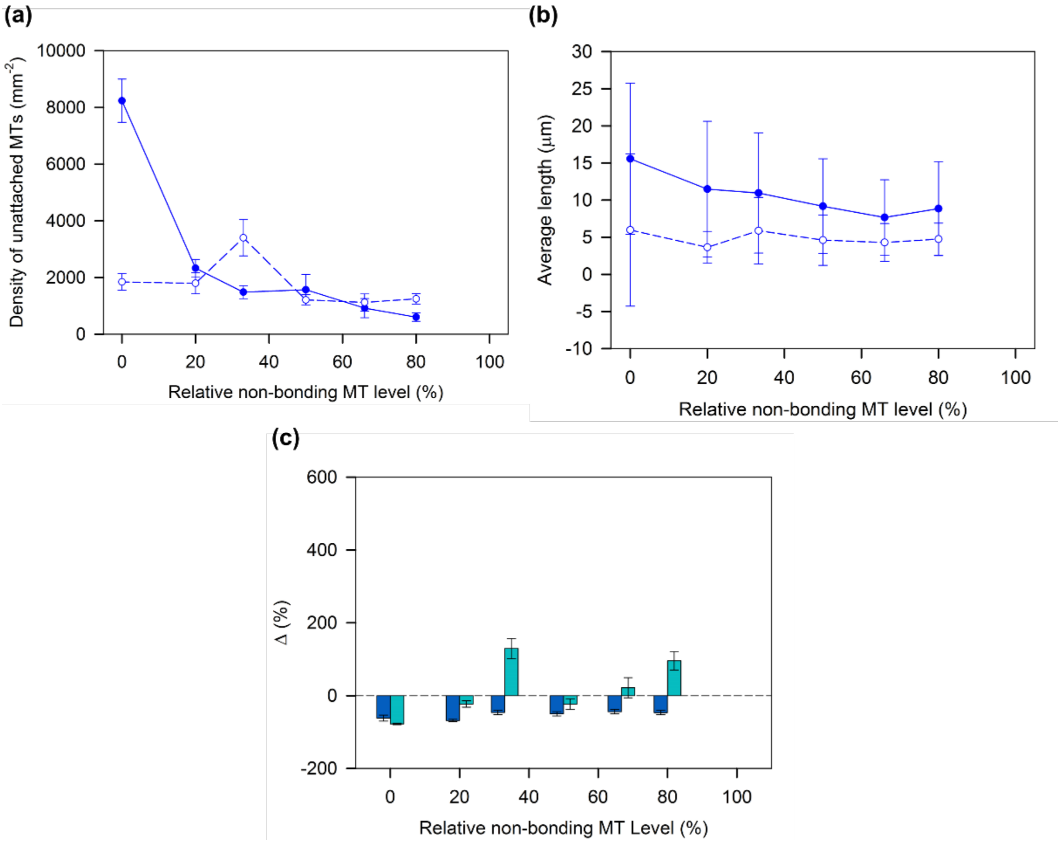

Figure A 3.4. Average change in density and length of bonding MTs as a function of non-bonding MT level. Average (a) density and (b) length were measured prior to (solid lines/closed circles, t=0) and after adding sQDs (dashed lines/open circles, t=30 min) for bonding MTs. Number of measurements for each data point in (a) was 5-6 images. Number of measurements for (b) was : (i) solid line = 90,80,74,85,74,58; dashed line = 74,88,129,75,77,54 for 0, 20, 33,50, 66, and 80% levels of non-bonding MTs, respectively. Error bars for (a) and (b)= standard deviation. (c) Change in the average density (■) and length (■) of unincorporated bonding MTs as a function of the non-bonding defective MT level. Number of measurements is the same as (a) and (b). Error bars= standard error of the mean.

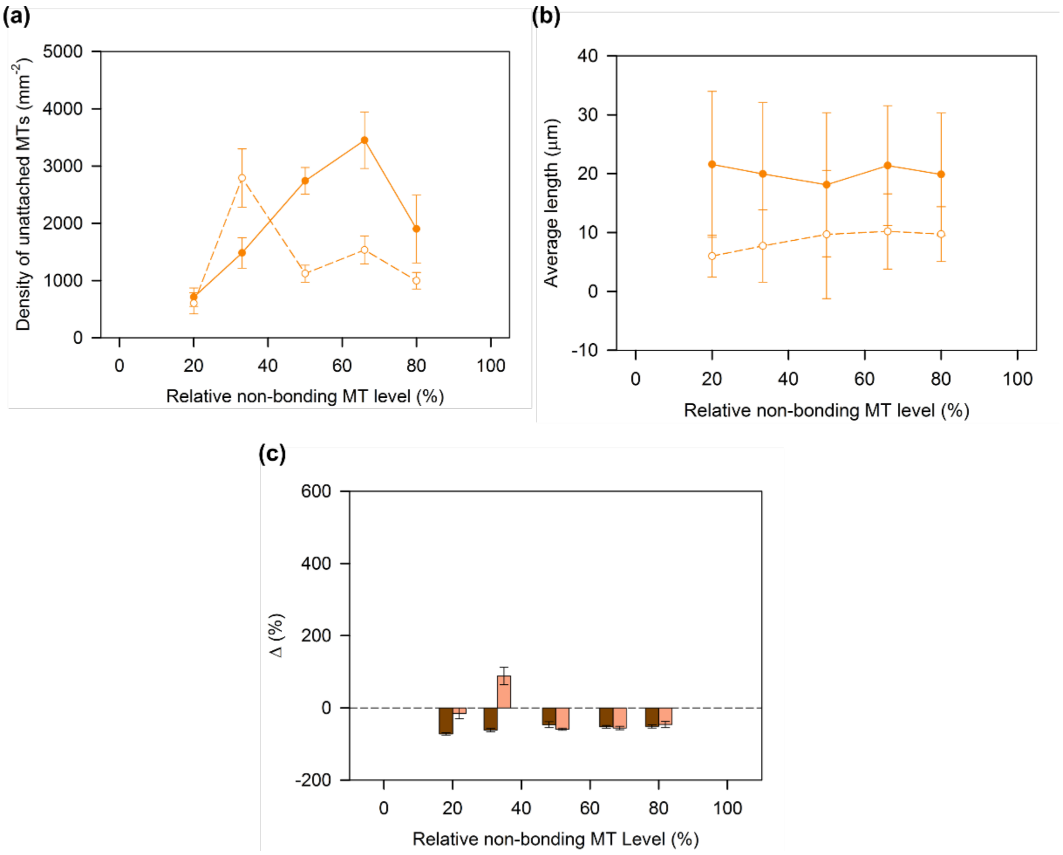

Figure A 3.5. Average change in density and length of segmented MTs as a function of non-bonding MT percent. Average (a) density and (b) length were measured prior to (solid lines/closed circles, t=0) and after adding QDs (dashed lines/open circles, t=30 min) for segmented MTs. Number of measurements for each data point in (a) was 5-6 images. Number of measurements for (b) was: (i) solid line=57,69,89,105,75; dashed line =58,76,75,79,47 for 0, 20, 33,50, 66, and 80% levels of non-bonding MTs, respectively. Error bars for (a) and (b)= standard deviation. (c) Change in the average density (🟧) and length (🟥) of segmented MTs as a function of the non-bonding defective MT level. Number of measurements is the same as (a) and (b). Error bars= standard error of the mean.

Chapter 4

Biomolecular probes navigate through chemical and topographical landscapes

Haneen Martinez [†], Nicholas J. D. Martinez [†], Jimin Guo [‡], Victoria R. Lujan [†], Jessica Depoy [†], Michael T. Brumbach [†], C. Jeffery Brinker [†, ‡], and George D. Bachand [, †]*

[†] Sandia National Laboratories, Albuquerque, New Mexico 87185, United States

[‡] Department of Chemical and Biological Engineering, University of New Mexico, Albuquerque, New Mexico 87131, United States

This chapter is under revision to be submitted to ACS AMI.

Abstract

Nanoscale transport using the kinesin-microtubule (MT) system has been successfully used in many nanotechnological applications including self-assembly, nanofluidic transport, and biosensing. These applications commonly use lithography to create physical or chemical patterns to guide MT motion in the gliding motility geometry, in which surface-adhered kinesin motors attach and propel MT filaments across a planar surface. However, these patterning techniques have been shown to limit the MT trajectories, where MTs can escape the barriers and lead to stalling or complete loss of MTs in the assays. In the present work, we prepared biocompatible substrates to explore the regulation of MT transport behaviors by: (i) chemically modifying surfaces using ω-functionalized alkanethiol self-assembled monolayers (SAMs) on gold with three (amine, carboxyl, and methyl) different functionalities, (ii) depositing fetal bovine serum (FBS) proteins on SAMs with varying secondary structures modulated by underlying functional groups of the SAMs and (iii) silicifying the layers to preserve the surface. Each layer was characterized using X-ray photoelectron spectroscopy (XPS), water contact angle, atomic force microscopy (AFM), and scanning electron microscopy (SEM) was used for the FBS layer only. We characterized the effects of surface chemistry and roughness of each layer on MT motility by tracking MTs to determine their velocities, trajectories, and displacement. Among all the modified surfaces, silicified surfaces revealed excellent properties supporting kinesin adhesion and MT transport, and hence, could be used as a potential model surface to guide motion on complex

substrates. Overall, this work establishes novel patterning techniques capable of supporting kinesin-based transport and provide valuable insights regarding biomolecular transport on complex nanostructures for future development of biosensing and probing applications.

Introduction

Miniaturization of lab-on-a chip devices to micro- and nanoscale dimensions necessitates hybrid systems integrating biological components[239]. Recently, attention has been geared towards using biological motors to power such devices since motor technologies based on silicon or related material are still in their infancy[240–243]. In cells, active transport is achieved by motor proteins capable of efficiently transporting cargo along cytoskeletal filaments via energy dissipation in the cytoplasm. One specific example is the motor protein kinesin-1, capable of carrying cell organelles and macromolecules over long distances along microtubule filaments[244]. Microtubules (MTs) are hollow polymeric protein filaments with a diameter of ~ 25 nm and tens of micrometers in lengths that form a 3D transportation network within the cell[239]. Kinesin motors can transport cargo at rates of ~ 12 $\mu m\ s^{-1}$ with energy efficiency of ~ 50% [11,245].

The intriguing properties of kinesin-based transport of molecular shuttles (MTs) made them of prime interest for applications in hybrid nanoscale systems. For example, this transport system has been used for molecular cargo pick-up and drop off, molecular cargo assembly, assembly of MT spools, and a prototype smart-dust biosensor[173,174,189,246]. These systems have been largely achieved using the well-established *in vitro* “gliding assay”, in which surface-adhered kinesin motors attach and propel MTs across a planar surface (Figure 4.1). Propulsion events in these assays enable the free end of the leading tip of the gliding MT to undergo thermal fluctuations until it locates and binds to a motor, and the remaining part of the MT stays anchored to the other motor proteins, a “search-

and-catch" mechanism that inspired the integration of such system into actively probing topographical and chemical properties of a surface[129,146,173,247–249].

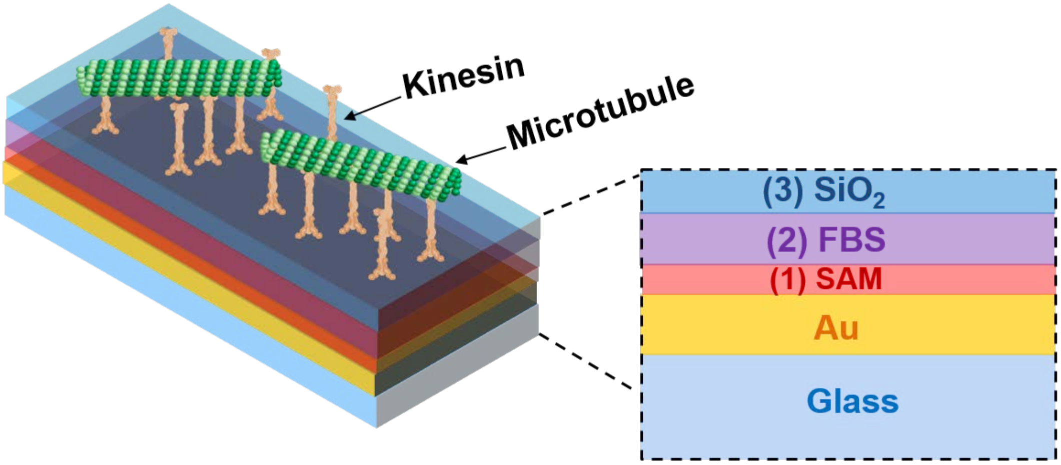

Figure 4.1. Schematic of the *in vitro* gliding motility assay on top layer (SiO_2). Kinesin motors attach and translate MTs via ATP hydrolysis on: (1) alkanethiol self-assembled monolayer (SAM), in which MT motility was evaluated on each of the following functional groups: CH_3, COO^-, and NH_3^+, (2) Fetal bovine serum (FBS) coated SAMs, and (3) silicified FBS on SAMs.

The production of nanoscale devices necessitates the development of nanofabrication processes that enable the integration of motor proteins without impacting their functionality[243]. Thus far, many nanofabrication processes are capable of creating structures with dimensions comparable to motor proteins and MTs, however, device fabrication techniques require chemistries that tend to be incompatible with biological materials[243,250]. For example, patterning using biological constituents such as proteins and cells has been explored in many applications including biosensor technology, tissue engineering, as well as fundamental studies of cell biology[251–257]. One very common and extensively used technique to attain such patterns is photolithography. This technique, however, possesses limitations including high costs of equipment, requirement for clean room access, and hindering of specific chemical and ligand functionalization onto surfaces for bio-specific adsorption[251]. Such techniques have also been shown to be problematic to the kinesin-MT system in which low quality of motility has been reported using lithographically nanostructured surfaces, MTs tend to get stuck and block transport paths, eventually causing MT detachment and loss. As such, a more biocompatible alternative is necessary, and one very commonly used technique for protein and cell patterning as an alternative to photolithography is to pattern a surface by altering the chemistry of the surface using self-assembled monolayers (SAMs)[251].

SAMs on a metal substrate are routinely used to investigate the influence of surface-chemistry induced cellular responses, as they have been shown to be excellent model systems for controlled surfaces[258–263]. SAMs offer many advantages that include a wide variety of chemical functionalities and chain lengths that can be easily synthesized with tunable surface properties, efficient self-organization into nanoscale thickness layers on gold without the requirement of external stimuli, and amenability to excellent characterization at the molecular level[264–268]. The ability to control the functional groups presented on the SAMs' surfaces renders them suitable to study specific and non-specific protein adsorption to surfaces[251]. We have previously shown that the combination of topographic patterns and surface chemistry (i.e. SAMs) affect adhesion of kinesin motors, further influencing MT motility and self-assembly of nanostructures[35]. In the present work, SAMs with three different functional groups (COO^-, NH_3^+, and CH_3) were used as model surfaces, and served as the first layer to explore the effect of substrate chemistry on microtubule motility (Figure 4.1).CH_3-SAMs are hydrophobic, while COO^- and NH_3^+ are relatively hydrophilic. At physiological pH (7.4), the COOH SAM displays a negatively charged surface, whereas NH_2 SAM displays a positively charged surface[269,270].

In vitro assays involving kinesin-MT studies, glass is typically the substrate of choice for its hydrophilic properties, where it allows for deposition of proteins necessary for bioactivity of the assays. Previous studies revealed that the interaction of internal hydrophobic domains of proteins with surfaces leads to changes in the secondary structures of the proteins[271,272]. These studies inspired us to explore the dominating effects of biomolecular motor protein interaction on protein patterns that exhibit various orientation and structures driven by surface functionality (i.e. SAMs with alternating charge and hydrophobicity). Our goal was to vary the resulting structures on the surfaces using proteins not directly involved with the assay. Here, MT motility was explored on serum proteins adsorbed on these modified surfaces (i.e., second layer), in which SAMs of each functional group was incubated separately in fetal bovine serum (FBS) prior to motility assay studies (Figure 4.1).

The first set of experiments focused on the effects of surface charge and secondary protein structures on MT motility using SAMs and FBS-coated SAMs, respectively. The next step was to maintain surface roughness using a well-established silicification process to better understand how the underlying surface features affect MT movement. As the predominant biomineralization method in nature, the biosilicification process resulting in silica under mild physiological conditions has attracted biologists, chemists, and materials scientists due to its ability to construct exquisite architectures with great structural control over nano- to millimeter length scales[273–277]. Cellular biosilicification is a self-limiting biomolecular surface-directed silica assembly process that results in nearly an exact replica of external and internal cellular architecture in the form of nanometer (<10 nm) thick silica layers[273–275]. Brinker et al.[273–276] reported that under mild acidic solution conditions, silica deposition is restricted to proteinaceous biomolecular surfaces, which serve as silica condensation catalysts. Once the catalytic sites are occluded, deposition is terminated, resulting in precise replication of inter- and intracellular heterogeneity. Cellular biosilicification also causes mechanical stabilization even after simple drying of the samples without significant dimensional changes. As such, a silicification process (i.e., third layer) was conducted on protein-coated (i.e., FBS) SAMs to maintain variation in the surface roughness to investigate the effect of the underlying topography of substrates on MT motility (Figure 4.1).

Overall, this work demonstrates the effects of surface chemistry and roughness on biomolecular motor protein adhesion and transport by using a set of “bottom-up” biocompatible fabrication techniques for future development of bioassays and molecular sensors.

Materials and methods

All chemicals were purchased from Sigma-Aldrich unless otherwise noted.

Fabrication of self-assembled monolayers (SAMs)

Round 15mm glass cover slips (26021, Ted Pella Inc.) were coated with gold and used as substrates for self-assembled monolayer (SAMs) formation. Coverslips were etched for 30 min prior to gold deposition in Piranha solution [70% (v/v) concentrated H_2SO_4, 30% industrial grade H_2O_2 (Fisher Scientific)] rinsed with diH_2O, and blown dry with N_2. Gold coating was conducted by sequential electroevaporation of optically transparent films of a chromium adhesion layer (2 nm; High Vacuum Evaporator Systems), followed by gold (30 nm, 99.99% purity; Plasmaterials). Metal deposition was accomplished at 2 nm/s using a Thermionics VE-90 vacuum Evaporation System (TLI Enterprises) with chamber pressures at or below 1×10^{-5} Torr. Freshly prepared gold substrates were immersed in 1mM ethanolic alkanethiol solutions [1-dodecanthiol (471364); 11-mercaptoundecanioc acid (450561-5G); 11-amino-1-undecanethiol, hydrochloride 1 N NaOH (A423-12, Dojindo Laboratories)] and SAMs were allowed to assemble for 12 h. Etched cover glass and gold-coated cover glass were incubated alongside SAMs in absolute ethanol. Before use or characterization, samples were cleaned of unbound thiols in absolute ethanol and dried with N_2.

Protein deposition

To permit silicification of SAMs surfaces, non-specific protein deposition was accomplished by incubating SAMs in buffered media (Dulbecco's Modified Eagle Medium (DMEM, Gibco) with 10% fetal bovine serum (FBS, Gibco) for 1 hour. Samples were rinsed with 1X phosphate buffered saline (PBS) and di-ionized water for salt removal and dried with N_2.

Silicification

For silicification, protein coated SAMs samples were rinsed with 1X PBS (Life technologies, Carlsbad, CA) and deionized water, then immersed in a silicification solution containing 100 mM tetramethyl orthosilicate (TMOS, ≥99%), 150 mM Sodium Chloride (NaCl) and 1.0 mM Hydrochloric acid for 24h at room temperature. After 24h silicification, samples were dehydrated by sequential rinsing in deionized water, 30% ethanol, 50% ethanol, 70% ethanol, 90% ethanol, and 100% ethanol (KOPTEC) for 5 min in each solution and allowed to air dry for 24h before storing at room temperature for further use.

Contact angle measurements

Static contact angles and images were evaluated using the sessile drop technique on a Model 100-00-115 Advanced goniometer (ramé-hart Instrument Co.). Briefly, 5 µL of ultrapure water was pipetted onto the sample surface and the contact angles were measured immediately after drop formation to minimize the effect of dynamic surface wetting and evaporation. Contact angle measurements between the water droplet and the sample surface were determined using DROPimage Standard software (ramé-hart Instrument Co.). This procedure was repeated three times at different sites on the same surface, and the contact angle of sample was expressed as the mean ± standard deviation of the three contact angle measurements.

X-ray photoelectron spectroscopy (XPS)

Elemental compositions of the surfaces were determined by XPS using a Kratos AXIS Supra. Base pressure of the system was less than 5 x 10^{-9} Torr. A monochromatic Al Kα (1486.7 eV) operating at 75 W was used as the source. In general, three spots on each sample were analyzed, and analysis region sizes were 300 x 700 microns elliptically. Survey spectra were recorded at 160 eV pass energy with 1.0 eV step sizes and 100 millisecond dwell times. High resolution scans were performed with 20 eV pass energy, 50 meV step sizes, and 200-600 millisecond dwell times depending on the signal of the core line of interest. Charge neutralization was provided from low energy electrons from a filament above the sample. Data was processed using CasaXPS (Casa Software Ltd.) using the built-in Kratos relative sensitivity factors for quantification.

Atomic force microscopy (AFM)

A Bruker (formerly Veeco) Dimension 5000 was used to scan and measure the surface topography of the samples. Three 10 μm^2 regions on the sample surface were scanned with tapping mode, using Bruker TESP-HAR tips, with a scan rate ranging from 0.2 Hz to 0.5 Hz. Slower scan rates were used for the samples with varied topography, while the faster scan rates were suitable to the more uniform surfaces. Image processing was limited to one dimensional flattening, and root mean square surface roughness analysis on the flattened images was done using Nasoscope software from Bruker.

Scanning Electron Microscopy (SEM)

The sample slides were mounted on SEM stubs (Ted Pella, Inc.) using conductive adhesive tape (12 mm OD PELCO Tabs, Ted Pella, Inc.). Samples were then sputter coated with a 10-nm layer of gold using a Plasma Sciences CrC-150 Sputtering System (Torr International, Inc.). SEM images were acquired under high vacuum, at 20-30 kV, using an FEI Quanta 3D FEG, (FEI, Hillsboro, OR, USA).

Preparation of motor proteins

Full-length *Drosophila melanogaster* kinesin-1 from the pPK113 expressing plasmid[98] was expressed in *Escherichia coli* BL21 (DE3) pLysS cells. Briefly, when the culture reached an OD_{600nm} of ~0.7, protein expression was induced through the addition of 0.5 mM isopropylthio-β-galactoside (IPTG). Cells were harvested by centrifugation at 9000×g, and stored at -80°C. Cells were lysed using BugBuster® with Benzonase® (EMD Biosciences, Inc., Billerica, MA) and 100 mM AEBSF (4-(2-Aminoethyl) benzenesulfonyl fluoride hydrochloride. Kinesin was then purified by Ni-NTA chromatography as previously described[98,156]. Protein concentration was determined by standard bicinchoninic (BCA) assay to be 4 µM. Aliquots of the protein were snap frozen in liquid nitrogen and stored at -80°C.

Preparation of Microtubules

Lyophilized unlabeled tubulin and Hilyte Fluor 488 labeled tubulin purified from porcine brain were purchased from Cytoskeleton Inc. (Denver, CO) and used according to manufacturer's instructions without further modification or purification. Fluorescent and unlabeled microtubules (MTs) were prepared by resuspending lyophilized tubulin in BRB80 buffer (80mM PIPES pH 6.9, 1 mM $MgCl_2$, 1 mM EGTA) containing 1mM GTP and 10% glycerol to a final tubulin concentration of 5 mg ml^{-1}. HiLyte™ Fluor 488 tubulin and unlabeled tubulin were mixed (25: 75 molar ratio), then polymerized at 37 °C for 30 min, and stabilized against depolymerization using BRB80 solution containing 10 µM paclitaxel for a final tubulin concentration of 0.1 mg ml^{-1}. MTs were incubated at room temperature for three days to fuse.

Motility assays

Inverted kinesin motility assays were performed by constructing a capillary flow cell on a glass slide using double-sided tape and a coverslip containing the designated layer, with average channel dimension of ~20 mm long, 5 mm wide, and 0.2 mm deep. Kinesin was diluted to 8 nM in 80mM PIPES with 2 mg mL^{-1} casein and 2 mM Adenosine 5′-(β,γ-imido) triphosphate (AMP-PNP), a nonhydrolyzable form of ATP used to immobilize the microtubules. This solution was added to the flow chamber and incubated for 5 minutes. The flow cell was then washed using motility solution (BRB80 containing 0.2 mg mL^{-1} casein, 1 mM AMP-PNP, 0.02 mg mL^{-1} glucose oxidase, 0.008 mg mL^{-1} catalase, 20 mM D-glucose, and 1 mM DTT) to remove unbound motors. Paclitaxel stabilized MTs were diluted in motility solution as described above except substituting 1 mM ATP for AMP-PNP to facilitate MT mobility. MTs were infused into the flow cell and incubated for 5 minutes to allow MTs to bind to the kinesin coated surface. The flow cell was washed with motility solution containing ATP to remove any unbound MTs.

Fluorescence Microscopy

The assays were imaged with two different microscopy systems: (1) Olympus IX-71 inverted fluorescence microscope with a 60x 1.42NA oil immersion objective, Orca3CCD digital camera (Hamamatsu), and U-MWIB3 (488 fluorophores) filter set, and (2) Lecia DMI3000 B inverted fluorescence microscope with a 63x

1.518NA oil immersion objective and Hamamatsu C11440 Orca flash 4.0 digital camera.

Image and Statistical Analysis

Image processing and manual tracking of MTs using MTrackJ were performed in Fiji[234]. Statistical analysis and plotting were performed using Sigmaplot 13.0 (Systat Software, San Jose, CA). Krushal-Wallis ANOVA (analysis of variance) on Ranks using Dunn's or Mann-Whitney post-test were used for data analysis. Differences were indicated by p-values < 0.05. All results were expressed in mean ± standard error of the mean.

Results and discussion

Characterization of modified substrates

Surface properties for (*i*) SAMs, (*ii*) FBS-coated SAMs, and (*iii*) silicified, FBS-coated SAMs were characterized by X-ray photoelectron spectroscopy (XPS) to detect the elemental composition near the outermost surface (~10 nm depth), contact angle measurements to determine surface wettability, and Atomic Force Microscopy (AFM) to evaluate surface topology and roughness. Each layer was characterized prior to MT motility studies, and results are summarized in Table 4.1, Figure 4.2, and Figure A4.1. To demonstrate changes in surface upon layer addition, characterization results are discussed for each layer separately.

Characterization of self-assembled monolayers (SAMs)

Previous studies have shown the quality of SAMs is highly dependent on the cleanliness of the substrate, purity of reagents, intrinsic stability of SAMs, and adventitious contamination caused by self-assembly and storage processes.[278–282] Therefore, since many factors can influence the SAM adsorption/arrangement on the surface, further influencing the following added layers and the MT motility results, we characterized the ultra-thin SAMs layer using multiple characterization methods, and further applied the testing procedure as a routine check to the added layers to determine changes on the surface.

Substrate	**Atomic composition (%)**					**Contact angle (°)**
	Au(4f)	C(1s)	N(1s)	O(1s)	Si(2s)	
Glass	0(0)	14.6 (0)	1.0 (0)	60.7 (72.1)	21.7 (26.2)	29.3 ± 2.2
Glass + FBS	0	47.0	10.0	32.0	9.0	46.2 ± 3.7
Glass + FBS + SiO_2	0	35.9	2.4	44.2	16.6	56.5 ± 6.0
Au	71.6 (100)	25.9 (0)	0 (0)	1.7 (0)	0.6 (0)	73.9 ± 1.2
Au + FBS	28.8	47.9	1.03	12.0	0.5	51.8 ± 1.6
Au + FBS + SiO_2	11.1	37.4	4.1	37.3	8.8	59.1 ± 0.7
CH_3	61.3(53.8)	37.8 (46.1)	0 (0)	0 (0)	0.8 (0)	100.7 ± 2.0
CH_3 + FBS	23.3	53.9	7.8	10.5	4.0	76.7 ± 6.5
CH_3 + FBS+ SiO_2	10.3	36.7	3.1	36.4	13.3	47.2 ± 2.2
COO^-	57.6 (51.8)	36.1 (40.7)	0 (0)	5.5 (7.4)	0 (0)	36.3 ± 0.1
COO^- + FBS	29.5	51.0	8.1	11.1	0.03	52.5 ± 2.8
COO^- + FBS + SiO_2	11.8	36.2	1.3	37.2	11.9	47.3 ± 0.4
NH_3^+	40.0 (53.8)	51.3 (42.3)	1.8 (3.85)	4.0 (0)	1.2 (0)	49.2 ± 1.1
NH_3^+ + FBS	28.1	52.3	8.2	10.1	0.7	56.1 ± 5.2
NH_3^+ + FBS + SiO_2	10.2	36.0	2.1	38.6	12.0	52.6 ± 3.9

Table 4.1. X-ray photoelectron spectroscopy atomic composition and static water contact angles (n=3; values are mean ± SEM) of SAMs, FBS coated SAMs, and silicified SAMS following FBS coating**.** Numbers in parentheses are theoretical values*.*

Contact angle measurements of the SAMs, shown in table 4.1, were in agreement with those reported in literature for similar SAMs.[259,283–286] As expected, the SAMs with polar groups tended to increase wettability (θ < 90°), whereas hydrophobic/nonpolar groups decreased wettability (θ > 90°). The untreated glass substrate was the most hydrophilic (θ = 29.3 ± 2.2°), while the gold-coated glass

(Au) was moderately hydrophilic (θ = 73.9 ± 1.2°). The difference in water contact angles between the Au and the SAMs/Au further confirms the presence of the varying functional groups on SAMs. Specifically, the COO^- and NH_3^+-SAMs exhibited hydrophilic characteristics (θ = 36.3 ± 0.1°, 49.2 ± 1.1°, respectively), while the CH_3-SAM had the highest contact angle (θ = 100.7 ± 2.0°) due to the hydrophobic nature of the monolayer.[280,285,287]

Complementarily, composition results from XPS analysis shown in Table 4.1 confirmed the wettability measurements. The values obtained for the SAMs were in general agreement with expected theoretical compositions (shown in parenthesis in Table 4.1) based on molecular structures of the alkanethiols used in this work. COO^- and NH_3^+ SAMs were easily confirmed by the presence of oxygen (5.5 at %) and nitrogen (1.8 at %). Carbon was detected on untreated glass and Au, which is indicative of organic contamination on these surfaces, along with oxygen on NH_2-SAM, which might have been the result of oxidized sulfur species.[279,288,289]

Surface morphology and roughness (root mean square) of all layers obtained using the AFM method are shown in Figure 4.2 and Figure A4.1. The 3D AFM images demonstrated surface morphologies with nanoscale roughness for the SAMs (Figure 4.2c, and Figure A4.1a) compared to glass (Figure 4.2a). Au (Figure 4.2b), COO^- (Figure 4.2c), and NH_3^+ (Figure A4.1a) had similar smooth topography, however, NH_3^+ had additional dispersed tall peaks on the surface. In contrast, CH_3 displayed considerably large peaks and valleys on the surface (Figure A4.1a).

Figure 4.2f shows the roughness values (mean ± SEM) for SAMs (grey bar), and higher roughness values for SAMs as compared to glass and Au indicated surface modification with thiolated SAMs. Glass surface roughness was similar to previously reported value[290] of 1.5 ± 0.1 nm, while Au had rougher surface of 4.9 ± 0.06 nm. Such high roughness value of Au could be attributed to defects that occurred during the deposition process, which led to island-like nanoclusters on the surface as opposed to the desired continuous metal film. Considering the nature of the SAMs used in our study, specifically the similarity in chain length, synthesis method, and their ability to assemble into a well-ordered thin film, we

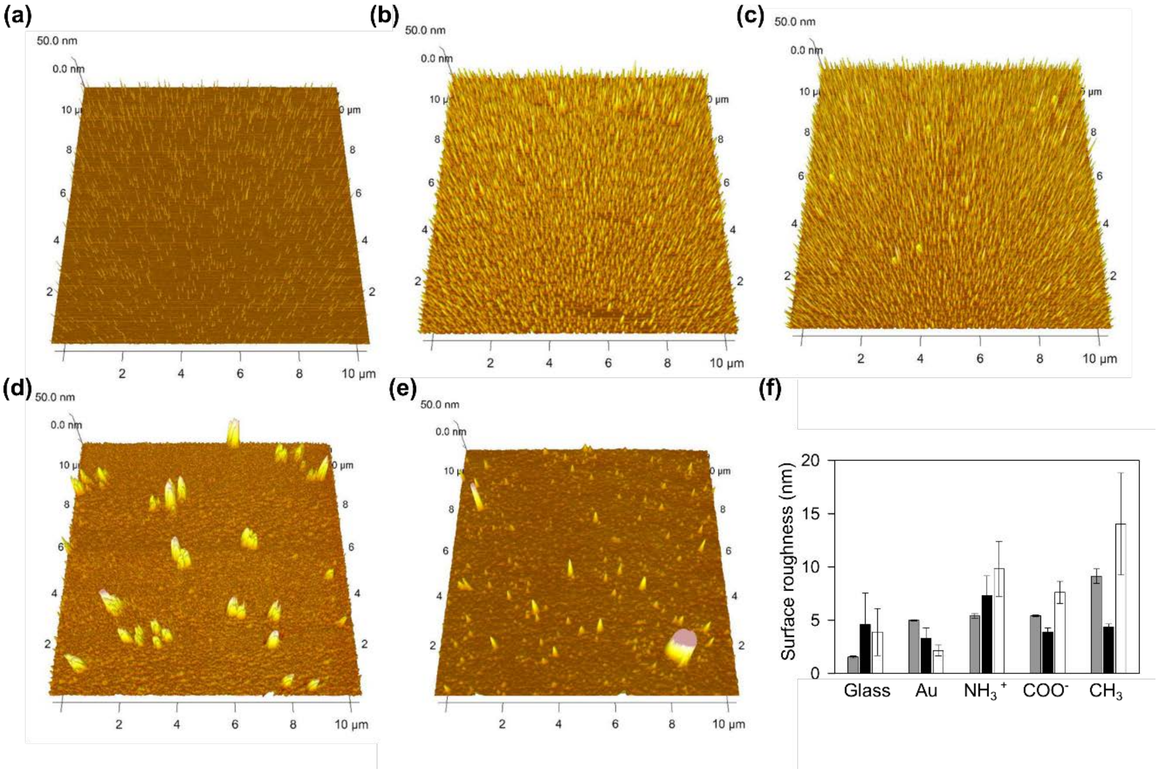

Figure 4.2. Atomic force microscopy (AFM) topography images of a) glass, b) Au, c) COO^-, d) COO^- + FBS, e) COO^- + FBS + SiO_2. Only COO^- terminated SAM is shown to demonstrate change in topography due to added layers, remaining AFM images are in Figure A 4.1f) Average surface roughness (n = 3 regions on the same sample) of SAMs (grey), FBS coated SAMs (black), silicified FBS coated SAMs (white). Error bars= standard error of the mean.

expected the roughness to be similar and smooth for all three end groups. Indeed, we found similar roughness values for COO^- and NH_3^+ of 5.42 ± 0.07 nm, and 5.41 ± 0.2 nm, respectively, which indicated deposition of smooth, tightly packed layers. Surprisingly, CH_3 had the roughest surface, attributed to the topographic tall peaks, with a roughness of 9.14 ± 0.7 nm, almost double the roughness of COO^- and NH_3^+.

It has been previously demonstrated that SAM surfaces can become unstable over time, and specifically, CH_3-SAMs can undergo partial desorption from the surface[291–296]. The desorption of CH_3-SAMs could have left voids in place of the desorbed thiol and exposed the underlying Au layer, which resulted in higher roughness than COO^- and NH_3^+. Additionally, a difference in the morphology and/or roughness could be due to disordering of the tail groups on the SAMs associated with their occupied space and deionization/ionization characteristics. COO^- SAMs can form a partial bi-layer or a compact monolayer with a mixture of diverse morphologies and slightly ordered domains, NH_3^+ is relatively disordered or may form a partial double-layer, and CH_3 forms well-ordered SAMs.[259,279,280,287,297–299]

Considering the wettability results together with the XPS and AFM measurements, we conclude the ω-functionalized alkanethiols were chemisorbed to gold with the terminal functional group at the outermost layer exposed. Additionally, the synthesized SAMs exhibit appropriate chemical functionality to explore the influence of surface chemistry on MT motility, and the subsequent addition of a protein layer.

Characterization of Fetal Bovine Serum (FBS) coated SAMs

Surface chemical and physical properties (e.g., wettability, roughness and topology) can regulate protein adsorption, adsorbed mass, and protein structures[259,300–305]. Frequently, protein adsorption on modified surfaces results in conformation and/or orientation changes, leading to protein unfolding and exposing internal regions to form additional contacts with the surface. Such processes (i.e., protein denaturation) are often associated with loss of secondary or tertiary structures that lead to irreversible adsorption.[272,306–308]

We used FBS, a supplement for *in vitro* cell culture of eukaryotic cells, as the primary source of proteins in our studies. FBS consists primarily of bovine serum albumin (BSA, ~66 kDa) i.e. 35-50 mg/ml[300]; as such, we hypothesized that most of adsorbed protein was BSA, with preferential denaturation/irreversible adsorption to hydrophobic surface (i.e. CH_3) as compared to other adhesive proteins (Fibrinogen (~340 kDa), Fibronectin (~ 440 kDa), and Vitronectin (~75 kDa)) present in FBS.[271,300,302,309–315] While we anticipated that most adsorbed proteins to be BSA, several studies have demonstrated preferential adsorption (i.e. Vroman effect[316]) of other adhesive proteins to hydrophilic SAMs (COO^- and NH_3^+), since BSA tended to adsorb weakly and was displaced by other adhesive serum proteins.[259,311,317–320]

SAMs were transferred to FBS culture medium immediately after removal from the thiol solution to mitigate contamination of surfaces. FBS served as the second layer to test MT motility, in which samples were first assessed by contact angle goniometry. For FBS-glass, FBS-COO^-, and FBS-NH_3^+, an increase in θ was detected. Conversely, a significant reduction in *ɵ* was seen for FBS-Au and FBS-CH_3. These results agree with previously reported reductions in *ɵ* for hydrophobic SAMs (CH_3), and increases for the hydrophilic SAMs (COO^-) due to incubation in culture medium containing FBS[291]. Overall, these results suggest that a moderately hydrophilic surface is attained through incubation in FBS due to protein adsorption on the surface.

The protein samples provided very similar atomic compositions obtained through XPS (Table 4.1). Carbon, oxygen and nitrogen atomic % increased and resulted in similar atomic composition due to the amine and carboxyl groups present in the peptide bonds and other trace elements from amino acid side chains in proteins[272,321–325], all of which indicated sufficient protein adsorption on the surface. The atomic % of oxygen decreased on FBS-glass as compared to glass, and this may be due to the low oxygen concentration in proteins compared to oxygen content of glass. Surprisingly, FBS-Au showed small atomic % for nitrogen that could be due to instrumental error. Additionally, the atomic % of Au decreased significantly for all samples due to denser layer of proteins on the surface.

Next, the morphology of the surface was evaluated with the added FBS layer through AFM, and a dramatic change was detected due to protein presence on the surface. FBS-glass had the smoothest topography (Figure A4.1b) with some dispersed peaks, followed by incrementally rougher surfaces of FBS-Au, FBS-CH_3, and FBS-NH_3^+(Figure A4.1b). FBS-COO^- (Figure 4.2d) showed very distinct and dispersed peaks compared to all FBS coated SAMs, while the surface around those peaks appeared smooth.

To better understand the nature of these surfaces, we performed Scanning Electron Microscopy (SEM) on the samples (Figure A4.2). Indeed, FBS-glass was the smoothest, while the remaining samples contained round structures on the surface (diameter ~50-70 nm). The round structures showed a more dispersed tendency on the hydrophilic SAMs (COO- and NH_3^+) and were more tightly packed and slightly smaller structures on FBS-Au and FBS-CH_3, with additional rod-like structures on FBS-CH_3. Differences in surface topography are attributed to the specific proteins that might have adsorbed from FBS onto the SAM surface, or the degree of denaturation, as discussed previously.

Further, we determined the roughness of the surfaces through AFM analysis, and results are summarized in Figure 4.2f (black bars). Results showed similar roughness values, except for FBS-NH_3^+, which had the highest average roughness of 7.3 ± 1.8 nm. This is clearly visible on the AFM images, where FBS-NH_3^+ (Figure A4.1b) appears to have the roughest surface compared to the remaining FBS coated SAMs (Figure 4.2d and A4.1b). FBS-glass and FBS-NH_3^+ (Figure 4.2f, black bars) increased in roughness as compared to their underlying layers (Figure 4.2f, grey bars), which possess hydrophilic properties. Interestingly, FBS-COO- (Figure 4.2f, black bar) with a hydrophilic underlying layer did not follow this trend. Instead, FBS-COO^- with sufficient protein adsorption of significant heights (Figure 4.2d) had a similar effect as FBS-CH_3 and FBS-Au (Figure 4.2f, black bars) that possess slightly more hydrophobic underlying layers, where roughness decreased as compared to their previous layers (Figure 4.2f, white bars). This could be due to areas around the proteins on FBS-COO$^-$ that are smooth enough to affect the RMS measurements of AFM.

Our results support protein adsorption on the SAMs surfaces, with surface modification supported by change in wettability to overall moderate hydrophilic surfaces and change in surface composition as compared to SAMs. Variations in surface topography and roughness were achieved by employing the ability of proteins to conform upon adsorbing to chemically modified surfaces. Overall, this method allowed for non-specific patterning of proteins with varying characteristics, in which MT motility will be evaluated on, followed by silicification of the layer.

Characterization of silicified FBS coated SAMs

The final and third layer to test MT motility was the silicified protein layer present on SAMs. The purpose of silicifying the second layer is to preserve the overall structure of proteins and underlying SAMs, and to provide a surface that has been well established for MT motility (i.e. glass), with additional roughness due to the underlying second layer.

As mentioned previously, under mild acidic conditions, silica deposition is limited to proteinaceous biomolecular surfaces that serve as silica condensation catalysts, however, without any cationic amine, self-condensation of silica precursors are suppressed. However, when this solution is added to the cells or proteinaceous biomolecular surfaces, the amine groups present on the surface could serve as silica condensation catalyst, inducing the silica formation. Once the catalytic sites are occluded by redundant silica, condensation is terminated, resulting in precise replication of biomolecular features. Here, we used the amine groups present on the serum proteins to serve as condensation catalysts to successfully silicify and preserve the underlying layer. Like previous layers, wettability measurements were implemented to determine change in surface, and θ values (Table 4.1) changed from the previous second (FBS coated SAMs) layer. However, θ remained moderately hydrophilic for all, including controls, and varied within 10° for the silicified surfaces. SiO_2-CH_3 showed a significant decrease of ~ 29° as compared to FBS-CH_3, and compared to the remaining silicified surfaces, rendering this layer to be the most affected through wettability measurements. Next, XPS analysis (Table 4.1) was conducted on samples to determine if there was a change in surface composition, and we expected an increase in silica and oxygen atomic % for all samples with successful silicification. The Si and oxygen atomic % significantly increased for all and varied within 10%, further supporting the addition of outermost SiO_2 layer. With the SiO_2 layer on top, it is inevitable to detect a change in the atomic % for the remaining elements. Indeed, mostly a decrease in atomic % was detected for Au, carbon, and nitrogen (except for SiO_2-Au, due to low atomic % for nitrogen in FBS-Au to compare to, as discussed in previous section) and resulted in similar atomic % among the different samples for these elements, further supporting the silicification of underlying layers.

Once we confirmed the SiO_2 layer was present on all samples, we evaluated the surface morphology and roughness of the added layer through AFM. Starting with controls, SiO_2-glass had dispersed, needle-like structures, while SiO_2-Au showed a very smooth surface (Figure A4.1c). Additionally, roughness decreased for both controls (Figure 4.2f, white bars), compared to FBS coated controls (Figure 4.2f, black bars), which indicated that silicification process smoothed out surfaces lacking the SAMs first layer. This is further supported by the obvious rough topography seen on the remaining surfaces with underlying SAMs of SiO_2-COO^- (Figure 4.2e), SiO_2-NH_3^+ and SiO_2-CH_3 (Figure A4.1c). Moreover, these surfaces with underlying SAMs also showed higher average roughness values (Figure 4.2f, white bars) as compared to the previous layer of FBS coated SAMs (Figure 4.2f, black bars), and much rougher than the Si-coated controls (i.e., Au and glass) (Figure 4.2f, white bars).

These results support the presence of the third SiO_2 layer, in which wettability measurements significantly changed from the previous FBS layer. Additionally, θ for the SiO_2 layer was moderately hydrophilic and similar (within 10°) for all SiO_2 coated substrates, further supporting sufficient coating of SiO_2 layer. This was further supported by the increase in Silicon and oxygen atomic composition. Interestingly, silicification smoothed out the substrates lacking the first SAMs (i.e. glass and Au), and rendered the substrates with underlying SAMs to be the roughest of all characterized substrates.

Effect of substrate modification on microtubule velocity

Cytoskeletal transport applications in hybrid systems necessitates the ability to actively steer and control transport, as well as manipulate the velocity of biomolecular motors[45]. With regard to the latter, regulation of transport velocity methods has been employed simply by altering the concentration of fuel in the system, for example via an ATP generation system and the photo-activated release of caged-ATP[326,327]. Other methods using interfacial properties of a surface have also been explored for controlling velocity such as switching the charge state of a conductive polymer, and changing the charge state of an azobenzene monolayer (photocontrol) resulting in reversible presentation of cationic amine groups[328–330].

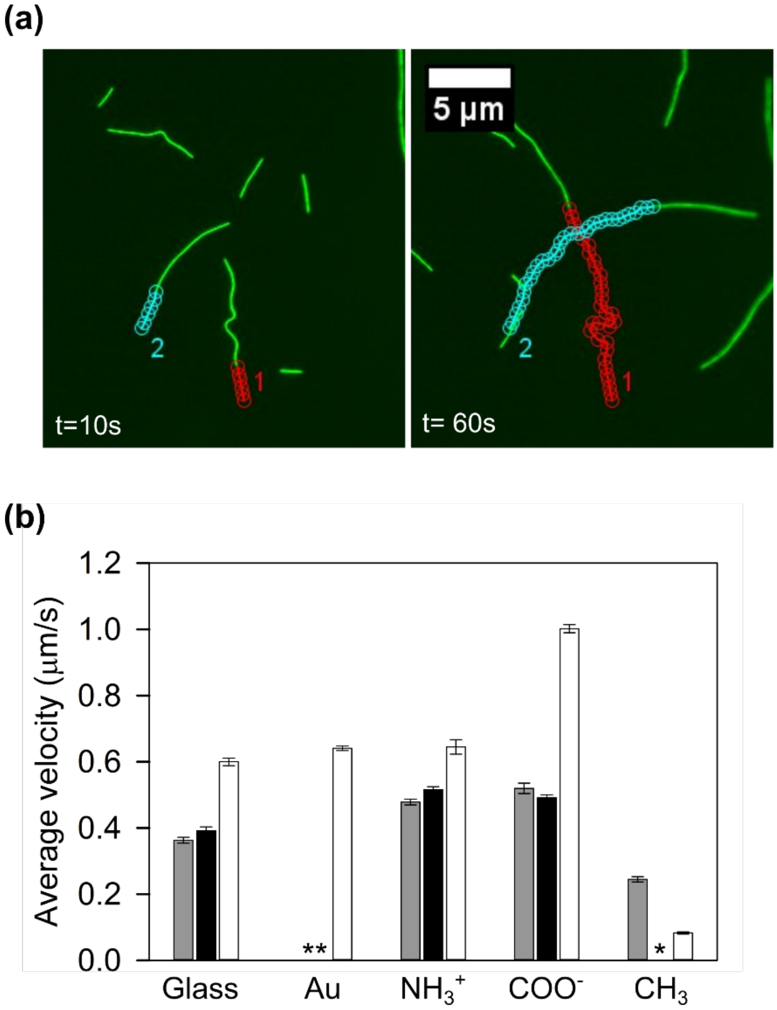

Figure 4.3. MT tracking to determine and average gliding velocity. (a) Time lapse images showing example tracks of fluorescently labeled MTs during active transport on control (glass) sample to determine velocity, trajectory, and displacement of MTs on each substrate. b) Average velocity of SAMs (grey), FBS coated SAMs (black), silicified FBS coated SAMs (white). Error bars= standard error of the mean. * = lack of motor/MT attachment and motility on surface.

To analyze the effects of interfacial and physical properties of our modified surfaces on the transport and velocity of MTs in the inverted motility geometry, we characterized their movement by tracking the MTs translated by surface bound kinesin motors. Here, mobile MT filaments were captured in sequential fluorescent photomicrographs with a 2-s time interval at a fixed location in the chamber, where the tip position for MTs (n = 7-10) was tracked over a time of approximately 120 s. Examples of two MTs tracked after 10 s and after 60 s are shown for control samples (Figure 4.3a). Figure 4.3b compares the average MT velocity (± SEM) for all modified surfaces; data sets are grouped by SAMs surface. Within each surface grouping, the data is further separated into SAMs treatment: uncoated SAMs (grey bars), FBS coated SAMs (black bars), and silicified FBS coated SAMs (white bars). Note that for Au, FBS coated Au, and FBS coated CH_3, MTs were not seen in the sample, therefore, MT velocities could not be measured. In these three cases, the surface was absent of motors for the MTs to attach and travel along. The distribution of the measured velocities for all modified surfaces along with average velocity values (± SEM) are shown in Supplemental Figure A 4.3.

In figure 4.3b, starting with the first layer of SAMs (grey bars), MT velocities varied on the different surfaces, except for COO^- compared to NH_3^+ (Supplemental Table A4.1). When SAMs receive FBS coating (Figure 4.3b, black bars), there is no nominal change in average velocity compared to the first layer of SAMs; differences, however, were observed among the FBS treatments ($p < 0.05$; Supplemental Table A4.1). Once the FBS layer was silicified (i.e. third layer), the SAMs surface, organic and inorganic, display an increase in velocity (Figure 4.3b, white bars). MT motility on the CH_3-SAMs did not follow this trend, which may be attributed to the significant surface roughness that was observed in AFM analysis.

For this surface, the MTs were observed to be fully blocked at the front end, causing the middle of the MT to build up tension and snap the front end to a new location.

Aside from the CH_3 surfaces, all velocities benefited from silicification. In fact, the Au surface, which saw no MT motility without surface treatment, had an average velocity comparable to the other SAMs surfaces after silicification. In the case of the COO^- surface, the average velocity almost doubled. Interestingly, silicifying the FBS second layer, independent of starting SAMs surface, produced a surface amenable to motor attachment and MT motility, even with increased roughness for the majority of the treatments. Additionally, we compared the average velocities for the silicified treatments, and both silicified control groups (Au and glass) did not indicate significant difference ($p > 0.05$), as well as no significant difference was seen for NH_3^+ vs. glass (Supplemental Table A4.1).

Further, the velocity measurements were compared at each treatment step to the preceding added layers, with results summarized in Supplemental Table A4.2. Au only had motility on the silicified surface, and therefore could not be evaluated. Glass and COO^- showed a similar trend of MT velocity, homologous to the initial SAM first layer and the following FBS second layer ($p > 0.05$). No significant difference was seen for MT velocity on the FBS-NH_3^+ vs. the silicified FBS-NH_3^+. These findings are interesting because, as roughness changes with added layers, we would expect to observe a difference in MT velocity with the addition of FBS and silicification. In this case, however, changes in roughness did not impact the overall MT velocity on the modified surfaces mentioned above.

Effect of substrate modification on microtubule trajectory and displacement

Several methods have been developed to directly control kinesin-based active transport in the inverted motility geometry. Some of these methods include chemical patterning and anti-fouling coating to control adsorption of kinesin to specific regions, physical patterns consisting of walls, overhangs, and microfabricated channels to direct transport of MTs, as well as magnetic and electric fields to manipulate velocity and direction of movement[133,136,143,144,331]. Additionally, guiding of MT transport was also achieved using a thermo-responsive polymer poly(*N*-isopropylacrylamide) (PINIPAM) that undergoes phase transition on heated gold electrodes, in which MT access to kinesin motors is regulated in the gold junctions[332]. These approaches of cytoskeletal transport show promise in ‘autonomous’ analytical and sensing applications, mostly because they require little to no external input, however, they limit the ability to observe and manipulate large number of MTs[45]. Our work, on the other hand, is not affected by such limitations, and as such, it was critical to address the effect of surface modification on MT transport by evaluating the MT trajectories and displacement on the various types of substrates.

Effect of SAMs substrates on MT trajectory and displacement

Microtubule trajectories were quantified for multiple substrates. Despite additional sampling, some SAMs surfaces were not amenable to kinesin adhesion and, thus, motility was not seen. For surfaces where displacement was measured, surface topography played a major role in impeding displacement. Microtubule motility on SAMs surfaces are shown in Figure 4.4: glass (control), NH_3^+, COO^-, and CH_3. Motility was not observed on the Au substrate. 10 MTs within the field of view were selected and their displacement was catalogued over a 120-s observation window. 3-dimensional surface plots for each SAM was done to highlight general trends, such as random and impeded displacements. The insets for each SAM surface show displacement normalized to a common origin, with the total displacement taking place in 120 s. These two methods of illustrating MT movement aid in identifying factors that enhance and impede displacement.

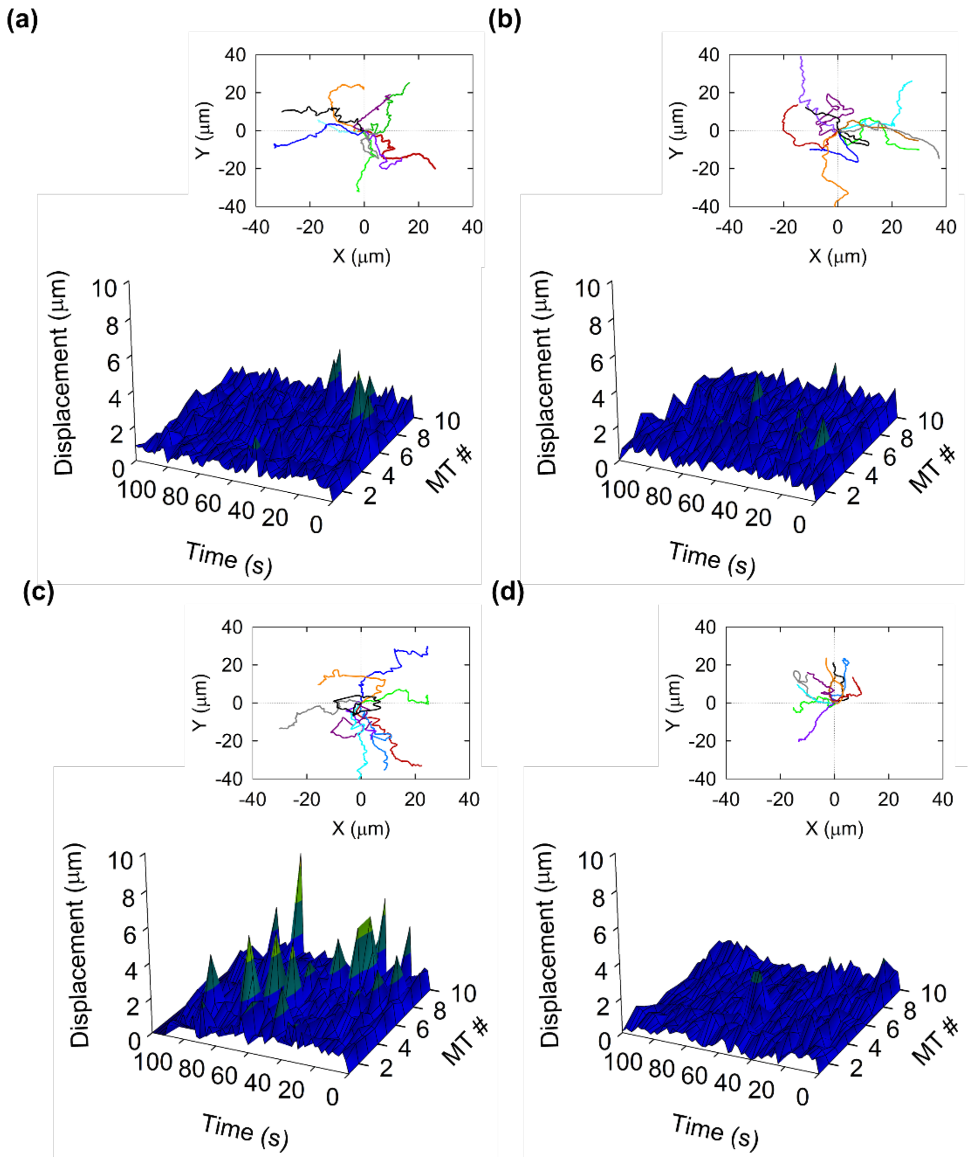

Figure 4.4. MT motility on various SAMs surfaces. Displacement-time plots for ten MTs on (a) glass, (b) NH_3^+, (c) COO^-, and (d) CH_3. No motility observed on Au surface. (Inset) Trajectories of the ten MTs with two second time interval. Each color corresponds to a different filament. The initial position for trajectory of each filament was normalized (x = 0, y = 0) so that filaments appear to emanate from an origin.

In Figure 4.4a, glass surface, the inset illustrates the MTs performing the expected ‘random walk,’ with no distinct pattern in any one direction. The 3D graph compares the speed of each MT, showing high speed, or large displacement, for MTs #8 and #10 around 20-40 s. In general, the MT speed was consistent over the 120 second observation time, approximately 0.4 µm s^{-1}. In Figure 4.4b inset, NH_3^+ surface, the same stochastic displacement was observed in the inset, with consistent displacement over time seen in the surface plot.

In Figure 4.4c inset, COO^- surface, random behavior was observed. However, in the surface plot, there are multiple instances for all the MTs where the displacement far exceeded the average, with some instances reaching 10 µm displacement in 2 s. The large instances of displacement correlates to sections in the microtubule movement, as shown in the inset, where the MT can travel in a somewhat constant direction, with little to no impedance in movement. This is the only notable case where the surface is smooth enough to reach higher displacement values, without silicification. The large instances in displacement are attributed to smooth, open areas where COO^- islanding did not form. Conversely, the abrupt transition in direction, and drop in displacement, is where the MT is colliding with one of these carboxyl islands.

Lastly, very minimal movement was observed from origin for MT motility on CH_3 surfaces (Figure 4.4d). Similarly, in the surface plot, the average displacement is constant over the 120 s, which can be attributed to roughened surface observed by AFM (Figure 4.2f and A4.1a). Although uniform, the CH_3 surface is too rough for the MTs to achieve any appreciable displacement. All CH_3 surfaces, regardless of precursors, exhibited minimal displacement, or no displacement at all, due to the roughness of the surface. Lastly, due to inconsistencies in organic layer deposition, some features permeated through the layers, causing pronounced barriers with which the MTs would collide. Therefore, to avoid adversely biasing the displacement measurements, only MTs that never impinged towards the pronounced feature were used for analysis.

Effect of FBS coated SAMs substrates on MT trajectory and displacement

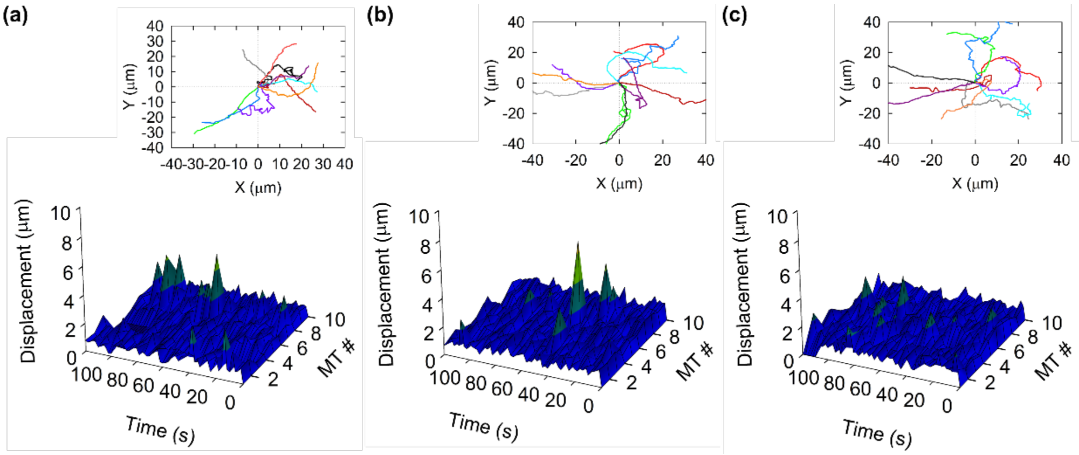

Figure 4. 5. MT motility on FBS coated SAMs. SAMs were incubated in fetal bovine serum (FBS) for protein deposition. Displacement-time plots and trajectories (inset) with two second time interval for ten MTs on (a) glass, (b) NH_3^+, and (c) COO^-. No motility observed on Au and CH_3 surfaces.

Figure 4.5 displays microtubule displacement on FBS-coated SAM surfaces. As previously discussed, movement on only three SAMs with FBS were observed: glass, NH_3^+, and COO^-. In Figure 4.5a, FBS-glass, the inset shows continued random behavior, with the surface plot showing similar average velocity as the untreated glass (Figure 4.4a). In Figure 4.5b, FBS-NH_3^+, there is a subtle increase in displacement for a few MTs; the average displacement, however, is consistent with the other SAMs, with and without FBS coating. Figure 4.5c, FBS-COO^- shows consistency in average displacement, with the peaks in displacement corresponding to an open area with no notable roughness, where the MT filaments could proceed unperturbed in a straight path. Note the FBS does not promote a stable adhesion layer for the kinesin motors, with only three of the surfaces promoting MT motility.

Effect of silicified FBS-coated SAMs substrates on MT trajectory and displacement

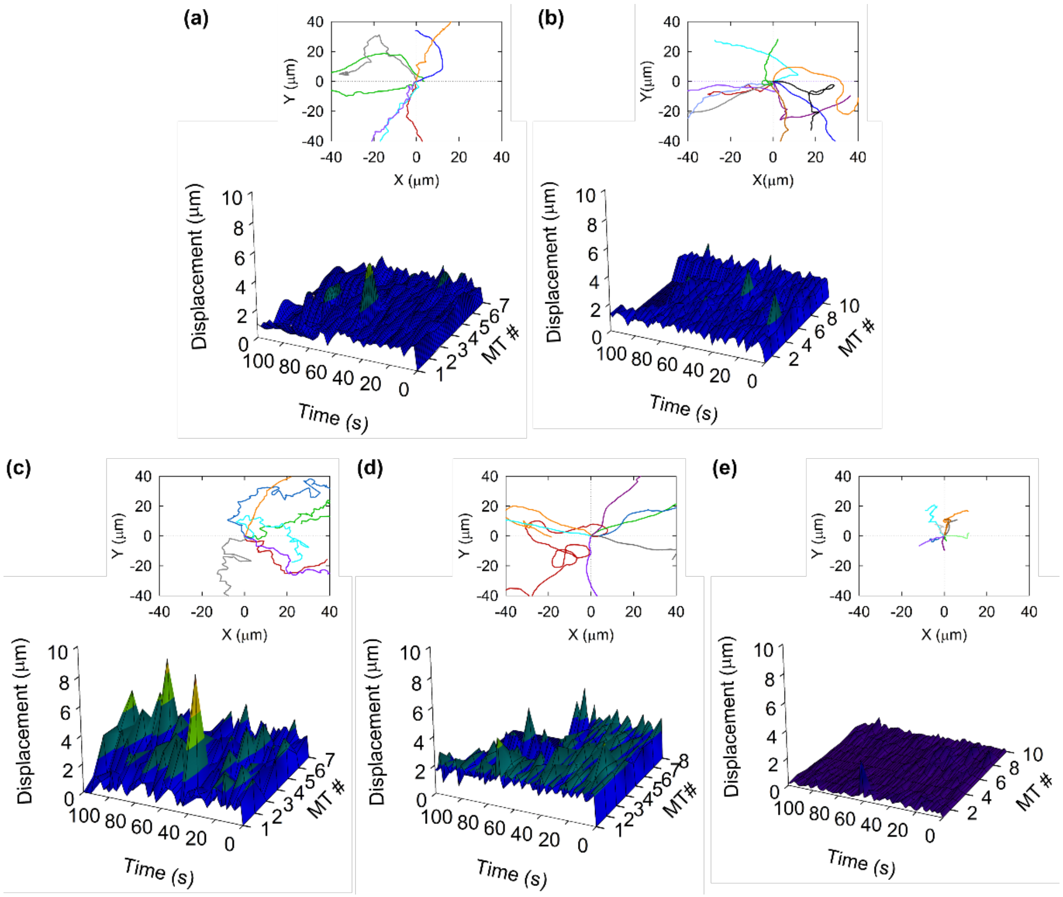

Figure 4.6. MT motility on silicified, FBS coated SAMs. SAMs were incubated in FBS, then surface was neutralized and preserved through silicification process. Displacement-time plots and trajectories (inset) with two second time interval for MTs (7<n<10) on (a) glass, (b) gold, (c) NH_3^+, (d) COO^-, and (e) CH_3.

Figure 4.6 encompasses data of MT motility where the FBS is silicified after being coated onto the SAMs. MT motility for SAMs surfaces with silicified FBS are seen in Fig. 4.6. MT motility was observed for all 5 SAMs: glass, Au, NH_3^+, COO^-, and CH_3. In Figure 4.6a, SiO_2-glass, the data are consistent with the previous

SAM surfaces, with and without FBS coating sets. However, the displacement has a notable general grouped direction, in this case, to the left. An underlying feature was also observed in the field of view, requiring the analysis of MTs that did not run into it. This gives explanation as to why all the measured MTs seem to all be translating in the same direction, but in fact, it’s the topological feature that limits us from using MTs that were traveling to the right during analysis.

The divergence of MT motility from the origin is random for SiO_2-Au surfaces, with consistent displacement over the 120 s (Figure 4.6b), which contrast the high, yet sporadic, displacement on SiO_2-NH_3^+ surfaces (Figure 4.6c). Further real-time examination of the MT displacement showed the MTs unable to maintain a constant direction. This is due to the surface roughness, where the surface was able to have kinesin adhesion, but not able to have it in an appreciable density. Therefore, the head of the MT would either run into a motor-vacant region, or a raised surface, impeding further displacement along that direction. The attenuated displacement is confirmed in the inset of Figure 4.6c, where the MTs are observed to have trouble maintaining a direction, and often stop at the front end completely. Because the rest of the MT is continuing forward, a bend forms, building up potential energy in the body of the MT, and finally snapping the front end in a new direction so it can continue moving.

In Figure 4.6d, SiO_2-COO^-, the trajectories are very smooth in the inset. Several of the MTs completely moved out of the field of view during observation for the 120 s. In addition, the average displacement, or velocity, is also higher by nearly 2x. Previously, the un-silicified surfaces allowed short bursts of displacement, but topography was rough enough to inhibit continual high displacement. Here, with SiO_2-COO^-, the silicification process has smoothed out the topography, lending to the highest average velocity in this work.

Lastly, in Figure 4.6e, SiO_2-CH_3, again the microtubules are observed to have minimal displacement. The inset of Figure 4.6e shows there is actual movement of the MTs, albeit the least amount of any measured SAMs. AFM shows a rougher surface, but with also larger variation in topography. From the surface images, the MTs are stalling in the micro-valleys of the rough surface, working to take the path of least resistance in a field of resistive paths. So, although they are able to move along slowly, there is no potential energy built up to redirect it onto another, more suitable, path. In all instances, other than for SiO_2-CH_3, all the MTs benefited from a higher average displacement, nearly doubling in all instances.

Conclusion

MT motility was explored on biocompatible surfaces consisting of three different layers: 1) nanoscale modified surfaces using self-assembled monolayers (SAMs) with varying functional groups, 2) fetal bovine serum (FBS) proteins adsorbed onto SAMs to create secondary structures with varying roughness, and 3) silicified FBS-coated SAMs to preserve the underlying layers. All three layers were characterized prior to motility studies using XPS, water contact angle, AFM, and SEM was used for FBS-coated SAMs layer. MTs were tracked on each of the three layers, and their overall trajectories, velocities, and displacement were evaluated to determine the effect of each presented layer on Kinesin-MT transport. Carboxyl-terminated SAMs impacted MT transport the most for all three layers, displaying reliable motor adhesion and MT transport at highest for the silicified FBS-coated layer. MTs on methyl terminated SAMs had the smallest velocity, with impeded MT movement, hence making it the least supportive for MT transport for any of the experimental layers. The FBS-SAMs (second) layer showed least attachment of all three layers, while the silica (third) layer proved to be amendable for motor attachment and MT motility. Overall, our results demonstrate the robustness of the kinesin-MT transport system in complex environments, and we conclude that silicified surfaces are ideal for potential use in future applications involving more complex surface features for development of hybrid biosensing and probing devices.

Associated content

Supporting Information

The following files are available free of charge.

AFM images of SAMs, FBS coated SAMs, and silicified FBS coated SAMs; SEM images of FBS coated SAMs; Figure showing histograms of microtubule gliding velocities for SAMS, FBS coated SAMS, and silicified FBS coated SAMs; Statistical analysis of MT velocity (PDF).

Author information

Corresponding Author

*Email: gdbacha@sandia.gov.

Notes

The authors declare no competing financial interest.

Acknowledgments

This work was supported by the U.S. Department of Energy, Office of Basic Energy Sciences, Division of Materials Sciences and Engineering (BES-MSE). This work was performed, in part, at the Center for Integrated Nanotechnologies, an Office of Science User Facility operated for the U.S. Department of Energy (DOE) Office of Science. Sandia National Laboratories is a multimission laboratory managed and operated by National Technology & Engineering Solutions of Sandia, LLC, a wholly owned subsidiary of Honeywell International Inc., for the U.S. Department of Energy's National Nuclear Security Administration under contract DE-NA0003525. This paper describes objective technical results and analysis. Any subjective views or opinions that might be expressed in the paper do not necessarily represent the views of the U.S. Department of Energy or the United States Government.

Appendix

Biomolecular probes navigate through chemical and topographical landscapes

*Haneen Martinez [†], Nicholas J. D. Martinez [†], Jimin Guo [‡], Victoria R. Lujan [†], Jessica Depoy [†], Michael T. Brumbach [†], C. Jeffery Brinker [†, ‡], and George D. Bachand *, [†]*

[†] Sandia National Laboratories, Albuquerque, New Mexico 87185, United States

[‡] Department of Chemical and Biological Engineering, University of New Mexico, Albuquerque, New Mexico 87131, United States

This chapter is under revision to be submitted to ACS AMI

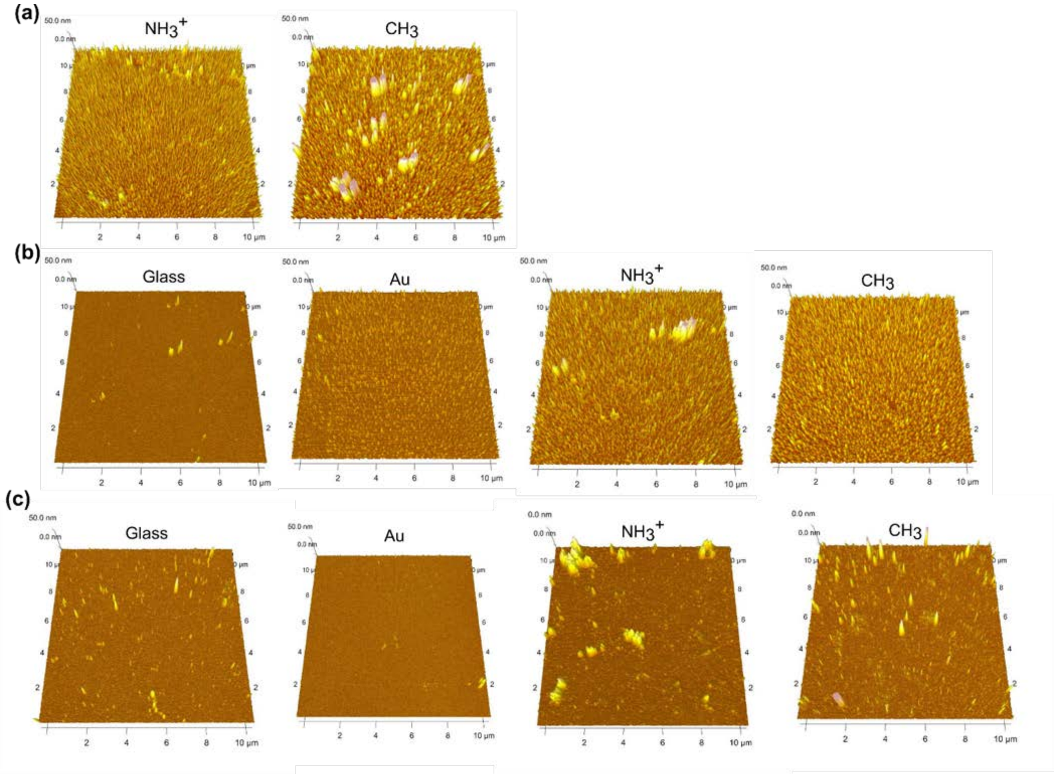
(a)
50.0 nm
0.0 nm
NH3+
CH3
(b)
Glass
Au
NH3+
CH3
(c)
Glass
Au
NH3+
CH3
2
4
6
8
10 µm

Figure A 4.1. Surface topography using atomic force microscopy (AFM) of (a) functionalized SAMs, (b) FBS coated SAMs, and (c) silicified FBS coated SAMs.

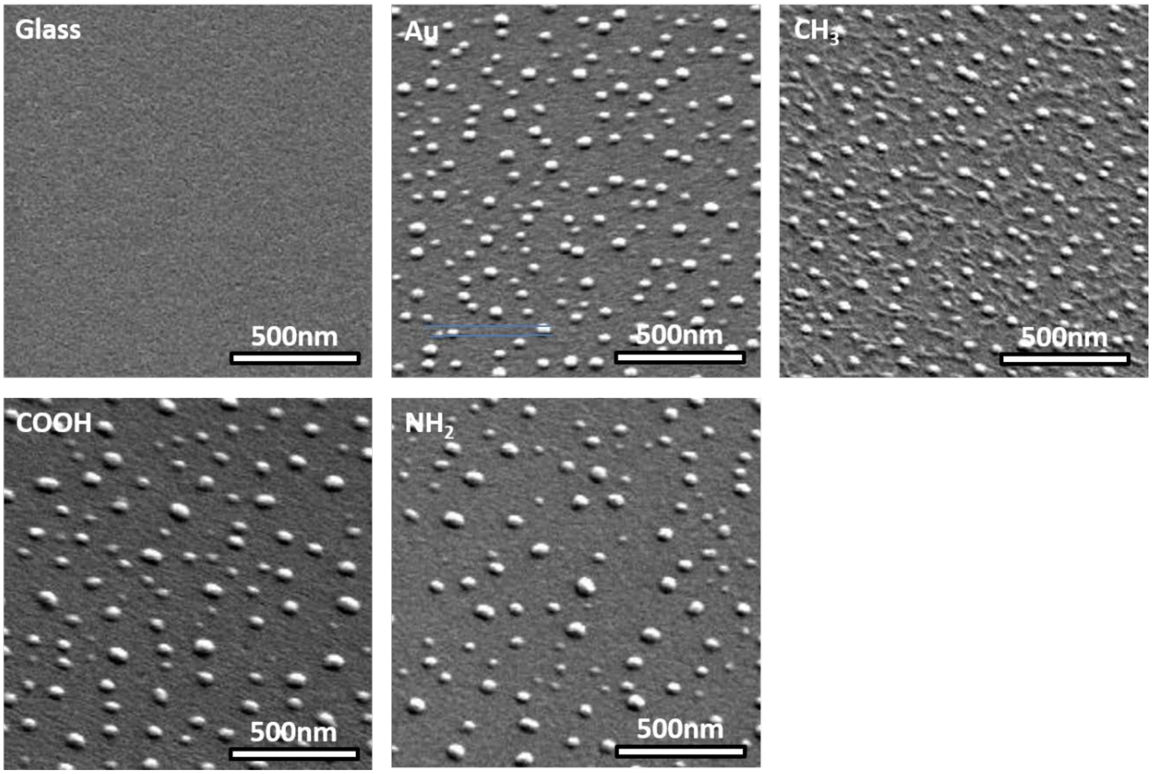
Glass
500nm
Au
500nm
CH_3
500nm
COOH
500nm
NH_2
500nm

Figure A 4.2. SEM images of FBS coated SAMs

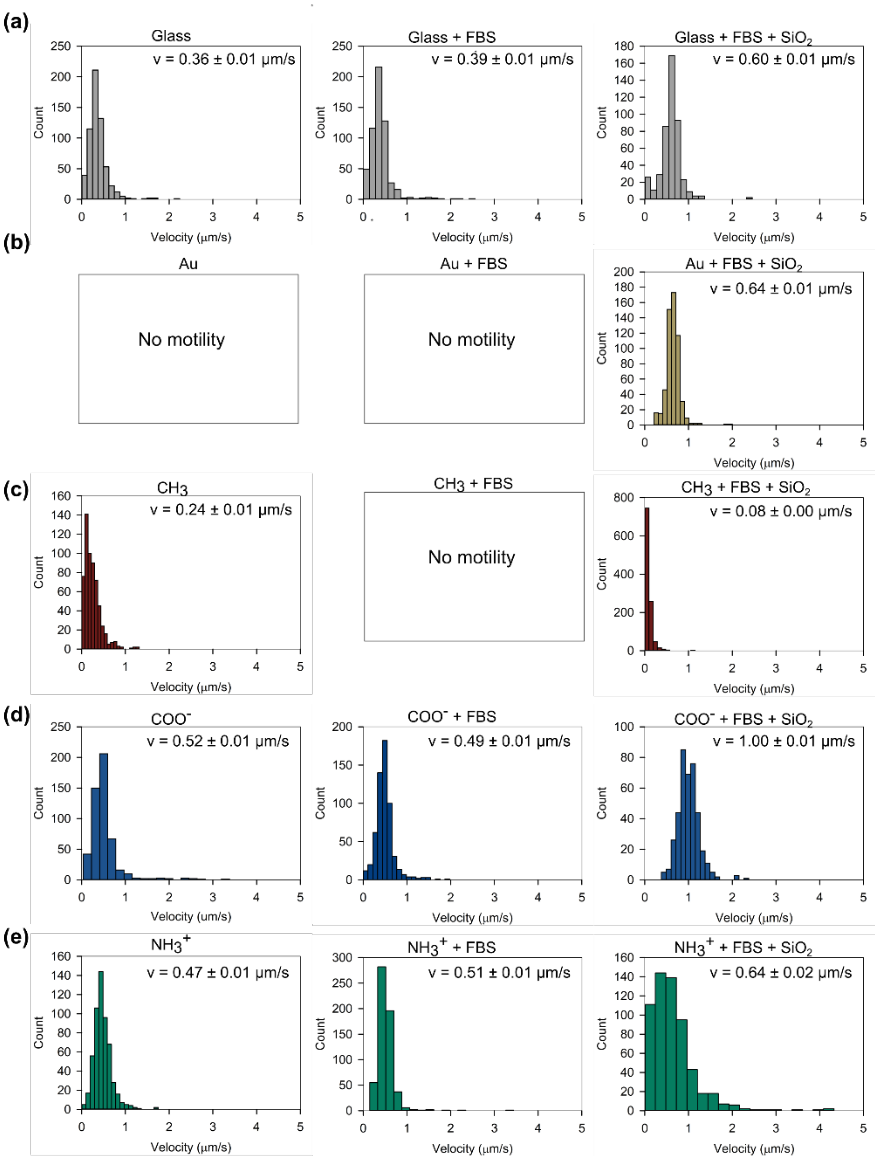

Figure A 4.3. Histograms of microtubule gliding velocities for SAMs, FBS coated SAMs, and silicified FBS coated SAMs for (a) glass, (b) gold, (c) CH_3, (d) COO^-, and (e) NH_3^+. v = Mean velocity ± SEM.

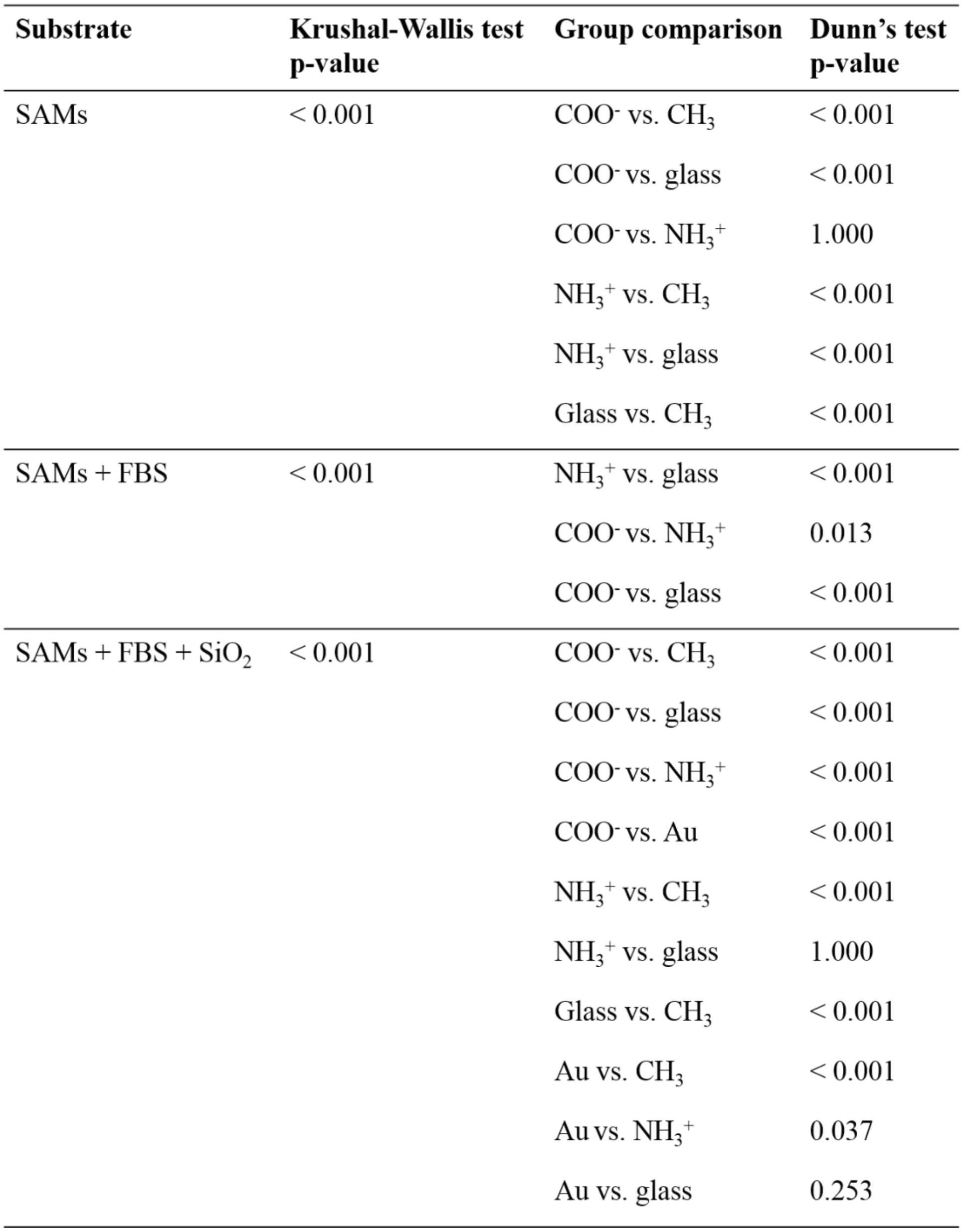

Substrate	**Krushal-Wallis test p-value**	**Group comparison**	**Dunn's test p-value**
SAMs	< 0.001	COO^- vs. CH_3	< 0.001
		COO^- vs. glass	< 0.001
		COO^- vs. NH_3^+	1.000
		NH_3^+ vs. CH_3	< 0.001
		NH_3^+ vs. glass	< 0.001
		Glass vs. CH_3	< 0.001
SAMs + FBS	< 0.001	NH_3^+ vs. glass	< 0.001
		COO^- vs. NH_3^+	0.013
		COO^- vs. glass	< 0.001
SAMs + FBS + SiO_2	< 0.001	COO^- vs. CH_3	< 0.001
		COO^- vs. glass	< 0.001
		COO^- vs. NH_3^+	< 0.001
		COO^- vs. Au	< 0.001
		NH_3^+ vs. CH_3	< 0.001
		NH_3^+ vs. glass	1.000
		Glass vs. CH_3	< 0.001
		Au vs. CH_3	< 0.001
		Au vs. NH_3^+	0.037
		Au vs. glass	0.253

Table A 4.1. Statistical results comparing velocity of gliding MTs on the various substrates using Krushal-Wallis One Way Analysis of Variance (ANOVA) on ranks, followed by a Dunn's post-test. Significance is indicated by p-values < 0.05.

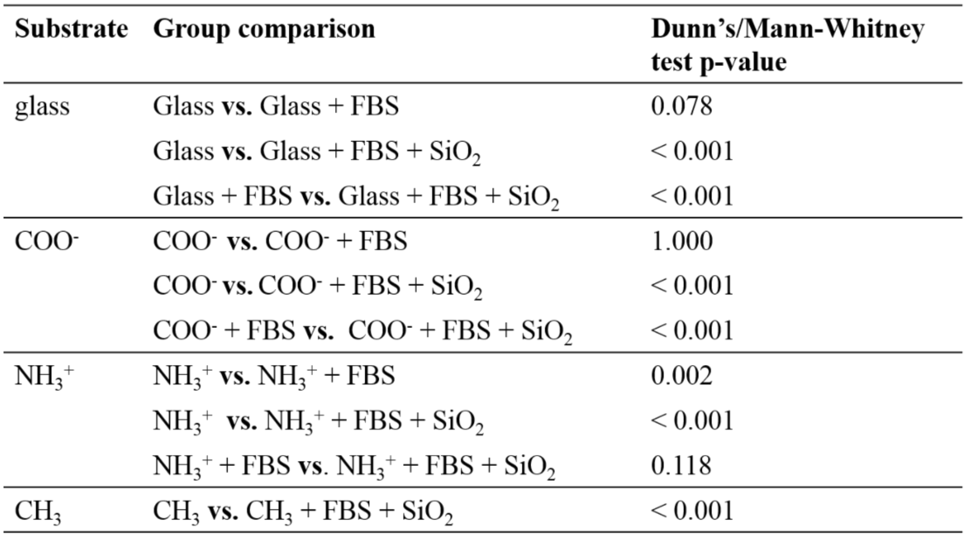

Substrate	Group comparison	Dunn's/Mann-Whitney test p-value
glass	Glass **vs.** Glass + FBS	0.078
	Glass **vs.** Glass + FBS + SiO_2	< 0.001
	Glass + FBS **vs.** Glass + FBS + SiO_2	< 0.001
COO^-	COO^- **vs.** COO^- + FBS	1.000
	COO^- **vs.** COO^- + FBS + SiO_2	< 0.001
	COO^- + FBS **vs.** COO^- + FBS + SiO_2	< 0.001
NH_3^+	NH_3^+ **vs.** NH_3^+ + FBS	0.002
	NH_3^+ **vs.** NH_3^+ + FBS + SiO_2	< 0.001
	NH_3^+ + FBS **vs**. NH_3^+ + FBS + SiO_2	0.118
CH_3	CH_3 **vs.** CH_3 + FBS + SiO_2	< 0.001

Table A 4.2. Statistical results comparing MT velocity on the various SAMs functional groups using Krushal-Wallis ANOVA on ranks, followed by a Dunn's or Mann-Whitney (for CH_3) post-test. Significance is indicated by p-values < 0.05.

Chapter 5

Conclusions and future direction

Self-assembly can be described as the process in which discrete components spontaneously organize into structures, and maybe divided into two categories: passive self-assembly, which is driven by thermal energy and produces close-to-equilibrium structures, and active self-assembly, driven by an external source of energy that can produce far-from-equilibrium structures. Biological processes commonly use active self-assembly processes, that rely on the conversion of chemical energy into mechanical work to overcome the speed limitations of diffusion-driven, passive-self-assembly[180].

An example of such phenomena found in nature is the ability of certain fish and cephalopod species to alter their color, a characteristic that has been explored for designing revolutionary materials with macroscale behaviors driven by dissipative assembly processes over multiple length scales in hybrid systems[333]. Considering the example of color change, the components involved in deriving such intracellular phenomena involve active transport of biomolecular motors moving along their associated cytoskeletal filaments. This dissertation has been focused on one of these transport systems, kinesin-MT.

MTs are one class of cytoskeletal filaments, along with filamentous actin, that provide structural support for the cell and act as intracellular network for motor protein transport. MTs are hollow filaments, ~25 nm in diameter and 10s of microns in length, formed by the polymerization of a protein dimer (8 nm in length) consisting of α and β tubulin. Assembly of these heterodimers in the presence of GTP forms protofilaments that laterally associate into sheets, and eventually a mature MT filament. These hollow tubular filaments have a distinct polarity of “plus” (β tubulin terminated) and “minus” (α tubulin terminated) end, which is important to the bidirectional transport of organelles by molecular motors. The concerted relationship between MTs and their associated molecular motors plays a critical role in many emergent cellular phenomena, such as chromosomal segregation during cell division at the cellular level, to macroscopic color changing at the organismal level as mentioned previously[31,45].

Kinesin molecular motors are a superfamily of MT-associated motors that convert chemical energy (ATP) into mechanical work needed to transport organelles through the viscous medium of a cell. Kinesin motor domains are able to “walk” directionally along the microtubule “tracks” with a step size of 8 nm, and rates of up to 12 µm/sec via ATP hydrolysis. The force associated with the kinesin stepping of ~6 pN per step, which translates to approximately 48 pN nm of energy expanded, and thermodynamic efficiency of ~ 50%[28,45]. Kinesin motors can be tethered to a surface in vitro (i.e. flow cell), and propel MTs across the surface, known as the “gliding motility geometry”. When cross-linkers capable of binding multiple MTs (e.g. streptavidin-coated Qdots) are present, MTs undergo self-assembly forming hybrid bundles, rings, and spools, that differ in shape and size depending on the specific conditions used for assembly[180]. Chapter 2 of this work highlights in depth the basic characteristics of the kinesin-MT system that is briefly discussed above, with details on recent research focusing on their applications in nanotechnology.

As previously mentioned, the MT-kinesin biomolecular motor system has been used to obtain a wide variety of assembled structures, but the ring and spool structures in particular have attracted considerable attention as these non-equilibrium structures are capable of storing large amounts of bending energy, and are capable of providing continuous work without changing the position of the mass center[168,192,204]. Therefore, understanding factors affecting the formation and properties of ring-shaped MT structures are important for use in future nanotechnological applications. In Chapter 3, we described how the inclusion of defective domains (i.e. non-biotinylated MTs incapable of bonding with streptavidin coated quantum dots (sQDs)) into MT supramolecular building blocks affect the dynamic assembly and behavior of motor-driven MT spools. This was demonstrated by creating segmented MTs by annealing MTs to contain alternating bonding (biotinylated) and non-bonding (non-biotinylated and defective) domains with varying lengths and frequencies. Our results demonstrated that segmented MTs were still capable of assembling into motor-driven spools, however, spool morphologies, densities and areas were overall affected. Interestingly, we observed preferential removal of these defect domains from the spools over time to offset the strain within these rotating spools.

The kinesin-MT system has also been used for many revolutionary nanotechnological applications, aside from fabricating complex non-equilibrium structures, including smart-dust biosensing,[173] cargo transportation,[174] and much more, by using the “gliding assay” geometry mentioned previously. This approach, however, poses a range of limitations where longer run times cause

MT loss due to MT shrinkage[188]and photodamage[233]. Low quality of motility and MT loss is particularly problematic in lithographically nanostructured surfaces, where MTs tend to get stuck and eventually detach from nanofabricated walls[36], adversely affecting the use of molecular motors in more intricate nanotechnological devices. Thus, exploring alternative nanostructures to investigate MT guiding is essential. Chapter 4 describes our collaborative effort to fabricate biocompatible multiple layers using a “bottom-up” approach, in which the layers displayed various chemistries and structures in order to further understand and regulate MT transport in complex environments. Briefly, we created three different layers and characterized each using multiple types of methods (details provided in Chapter 4) by: 1) altering the surface chemistry using self-assembled monolayers (SAMs) with three physiologically relevant functional groups (CH_3, COO^- and NH_3^+) to serve as the first layer to test MT motility on each of the functional groups; 2) created varying structures on the surface by incubating each SAM with fetal bovine serum (FBS) for protein patterning (second layer) , and 3) silicifying the FBS-coated SAMs (third layer) to preserve the structures on the surface. We evaluated the overall MT velocities, trajectories and displacement on each layer, and our overall results showed silicified surfaces to be the most compatible for kinesin-MT adhesion and transport, a surface that can be potentially applied to more complex structures in the future.

Overall, the work outlined in this dissertation highlights the effects of large scale defective MTs on the active assembly of MT spools, as well as the effects of surface chemistry and roughness on MT transport. This work provides crucial insights for future development of adaptable hybrid nanomaterials, as well as advancement of materials with revolutionary characteristics such as self-regulating and healing multi-functional constituents. However, there's still much work needed to fully explore the capability of these materials. Follow-on work is discussed below, based on experimental limitations we encountered, followed by future direction of this work.

With respect to the spool formation in the presence of non-bonding defective segments, our results supported defect removal from the spools, however, this was only visualized from the tail ends of the spools (Figure 3.4). We have attempted experiments using a microfluidic device previously utilized in many of our experiments in the lab to investigate how defects are released over the course of thirty minutes, in hopes to visualize their release from the loops; however, our attempts were unsuccessful. Although this has been a reliable technique, many issues arise[31,233] due to the nature of the experiment requiring imaging in a single field of view, causing photodamage and the probability of observing such events being extremely low. Future experiments utilizing this device would require control over these issues, which would require a separate, more complex design for successful execution of real time characterization of these structures. Further, in depth characterization of the structures is necessary to evaluate the effect of the varying levels of the non-bonding defective MTs on the spool formation and properties, a characteristic limited by fluorescence microcopy and available software (for 3D reconstruction). Future work involving high-resolution techniques (e.g AFM and SEM) would be necessary to determine miniscule difference in structures, and possibly even reveal sites at which breakage and release of the MTs occur. Because these are biological materials, they can be sensitive, and therefore, sample preparation and technique performance can potentially damage these structures. This can be mitigated through silicification (process described in Chapter 4) of the spools to preserve the structures, where chemicals/forces applied to sample will be tolerated. This by far may be the most promising approach, as we have successfully silicified MTs, in which the MTs maintained their structure in a gliding motility assay for > 6 months at room temperature (data not included here).

Moving forward, future work involving the advancement of self-regulation of the spool structures can be achieved by modifying the MT building blocks with specific chemical functionalities requiring complementary binding groups within the system. As shown in our work in Chapter 3, using biotin-streptavidin non-covalent bonding, we defined exact locations for the sQDs to attach to. Here, we can leverage off this concept by exploring other types of chemical functionalities, both covalent and non-covalent. For example, the assembly of two populations of differentially modified MTs in the same system could be controlled through complementarity of different chemistries on QDs. Additionally, this approach can be further implemented into a layer-by-layer growth of rings/spools using the molecular encoding of MTs and sequential delivery of complementary QDs. Such control will enable for motor-driven assembly of nanocomposites with optical properties dictated by the radial organization of the individual nanoparticle-microtubule layers. For instance, this can be useful in the design of multicomponent QD-QD FRET devices for sensing applications[334,335].

Additionally, we demonstrated successful fabrication of biocompatible substrates with complex features and varying chemistries and determined the effects of such substrates on kinesin-MT transport. However, one major limitation was determining the layers' thicknesses, as this is an important characteristic for a "bottom-up" fabrication method in order to determine if, for example, some of the layers are integrating, or if we have purely defined layers. We attempted to use X-ray reflectivity, and the results showed inconsistent measurements, especially for the FBS layer, a characteristic of protein interaction with the underlying SAMs layer. This could also be a result in the variance caused by repeated experiments or the deposition process of the gold/SAMs layer, in which slight variation in the first layer can affect and lead to inconsistencies in the following two layers. Another characterization method should also be explored, for example, using surface plasmon resonance (SPR).

Further, we envision the creation of more complex structures than ones reported in Chapter 4, for example, using microcontact printing to pattern SAMs on specified substrate locations, and functionalizing the remaining bare (gold) surfaces with SAMs displaying different functional groups. This will enable the fabrication of surfaces with SAMS of different functional groups on the same substrate with varying wettability and roughness. This can also be utilized for protein patterning (i.e, FBS) as the proteins on the surface would result in varying secondary structures within defined distances, allowing to further explore MT motility on surfaces with varying degrees of roughness and charge.

References

(1) Vélez, M. Dynamic and Active Proteins: Biomolecular Motors in Engineered Nanostructures. *Adv. Exp. Med. Biol.* **2016**, *940*, 121–141.

(2) Korten, T.; Mansson, A.; Diez, S.; Månsson, A.; Diez, S. Towards the Application of Cytoskeletal Motor Proteins in Molecular Detection and Diagnostic Devices. *Curr. Opin. Biotechnol.* **2010**, *21* (4), 477–488.

(3) Kinbara, K.; Aida, T. Toward Intelligent Molecular Machines: Directed Motions of Biological and Artificial Molecules and Assemblies. *Chemical Reviews*. **2005**, pp 1377–1400.

(4) Hess, H.; Bachand, G. D. Biomolecular Motors. *Mater. Today* **2005**, *8* (12 SUPPL. 1), 22–29.

(5) Erbas-Cakmak, S.; Leigh, D. A.; McTernan, C. T.; Nussbaumer, A. L. Artificial Molecular Machines. *Chemical Reviews*. **2015**, pp 10081–10206.

(6) Ross Kelly, T.; Silva, R. A.; De Silva, H.; Jasmin, S.; Zhao, Y. A Rationally Designed Prototype of a Molecular Motor. *J. Am. Chem. Soc.* **2000**, *122* (29), 6935–6949.

(7) Koumura, N.; Zijistra, R. W. J.; Van Delden, R. A.; Harada, N.; Feringa, B. L. Light-Driven Monodirectional Molecular Rotor. *Nature* **1999**, *401* (6749), 152–155.

(8) Fournier-Bidoz, S.; Arsenault, A. C.; Manners, I.; Ozin, G. A. Synthetic Self-Propelled Nanorotors. *Chem. Commun.* **2005**, No. 4, 441–443.

(9) van Delden, R. A.; Koumura, N.; Harada, N.; Feringa, B. L. Unidirectional Rotary Motion in a Liquid Crystalline Environment: Color Tuning by a Molecular Motor. *Proc. Natl. Acad. Sci.* **2002**, *99* (8), 4945–4949.

(10) Fennimore, A. M.; Yuzvinsky, T. D.; Han, W. Q.; Fuhrer, M. S.; Cumings, J.; Zetti, A. Rotational Actuators Based on Carbon Nanotubes. *Nature* **2003**, *424* (6947), 408–410.

(11) Hess, H.; Bachand, G. D.; Vogel, V. Powering Nanodevices with Biomolecular Motors. *Chemistry - A European Journal*. **2004**, pp 2110–2116.

(12) Vogel, V. Reverse Engineering: Learning from Proteins How to Enhance the Performance of Synthetic Nanosystems. *MRS Bull.* **2002**, *27* (12), 972–978.

(13) Howard, J.; Hudspeth, A. J.; Vale, R. D. Movement of Microtubules by Single Kinesin Molecules. *Nature* **1989**, *342* (6246), 154–158.

(14) Agarwal, A.; Hess, H. Biomolecular Motors at the Intersection of Nanotechnology and Polymer Science. *Prog. Polym. Sci.* **2010**, *35* (1–2), 252–277.

(15) Stayton, P. S.; Shimoboji, T.; Long, C.; Chilkoti, A.; Ghen, G.; Harris, J. M.; Hoffman, A. S. Control of Protein–ligand Recognition Using a Stimuli-

Responsive Polymer. *Nature* **1995**.

(16) Ding, Z.; Fong, R. B.; Long, C. J.; Stayton, P. S.; Hoffman, A. S. Size-Dependent Control of the Binding of Biotinylated Proteins to Streptavidin Using a Polymer Shield. *Nature* **2001**.

(17) Bath, J.; Turberfield, A. J. DNA Nanomachines. *Nature Nanotechnology*. **2007**.

(18) Chen, Y.; Wang, M.; Mao, C. An Autonomous DNA Nanomotor Powered by a DNA Enzyme. *Angew. Chemie - Int. Ed.* **2004**.

(19) Duhl, D. M.; Renhowe, P. A. Inhibitors of Kinesin Motor Proteins - Research and Clinical Progress. *Curr. Opin. Drug Discov. Devel.* **2005**.

(20) Alpert, N. R.; Mulieri, L. A.; Warshaw, D. The Failing Human Heart. *Cardiovascular Research*. **2002**.

(21) Stokin, G. B.; Lillo, C.; Falzone, T. L.; Brusch, R. G.; Rockenstein, E.; Mount, S. L.; Raman, R.; Davies, P.; Masliah, E.; Williams, D. S.; et al. Axonopathy and Transport Deficits Early in the Pathogenesis of Alzheimer’s Diseases. *Science.* **2005**.

(22) Aridor, M.; Hannan, L. A. Traffic Jams II: An Update of Diseases of Intracellular Transport. *Traffic* **2002**.

(23) Yanagida, T.; Nakase, M.; Nishiyama, K.; Oosawa, F. Direct Observation of Motion of Single F-Actin Filaments in the Presence of Myosin. *Nature* **1984**, *307* (5946), 58–60.

(24) Suzuki, H.; Yamada, A.; Oiwa, K.; Nakayama, H.; Mashiko, S. Control of Actin Moving Trajectory by Patterned Poly(Methylmethacrylate) Tracks. *Biophys. J.* **1997**.

(25) Nicolau, D. V.; Suzuki, H.; Mashiko, S.; Taguchi, T.; Yoshikawa, S. Actin Motion on Microlithographically Functionalized Myosin Surfaces and Tracks. *Biophys. J.* **1999**, *77* (2), 1126–1134.

(26) Dennis, J. R.; Howard, J.; Vogel, V. Molecular Shuttles: Directed Motion of Microtubules along Nanoscale Kinesin Tracks. *Nanotechnology* **1999**, *10* (3), 232–236.

(27) Hess, H.; Clemmens, J.; Qin, D.; Howard, J.; Vogel, V. Light-Controlled Molecular Shuttles Made from Motor Proteins Carrying Cargo on Engineered Surfaces. *Nano Lett.* **2001**, *1* (5), 235–239.

(28) Hess, H.; Vogel, V.; U, H. H.; Vogel, V. Molecular Shuttles Based on Motor Proteins: Active Transport in Synthetic Environments. *Rev. Mol. Biotechnol.* **2001**, *82* (1), 67–85.

(29) Kabir, A. M. R.; Kakugo, A. Study of Active Self-Assembly Using Biomolecular Motors. *Polym. J.* **2018**.

(30) Lam, A. T.; VanDelinder, V.; Kabir, A. M. R.; Hess, H.; Bachand, G. D.; Kakugo, A. Cytoskeletal Motor-Driven Active Self-Assembly in in Vitro Systems. *Soft Matter* **2016**, *12* (4), 988–997.

(31) VanDelinder, V.; Brener, S.; Bachand, G. D. Mechanisms Underlying the Active Self-Assembly of Microtubule Rings and Spools. *Biomacromolecules* **2016**, *17* (3), acs.biomac.5b01684.

(32) Bachand, M.; Trent, A. M.; Bunker, B. C.; Bachand, G. D. Physical Factors Affecting Kinesin-Based Transport of Synthetic Nanoparticle Cargo. *J. Nanosci. Nanotechnol.* **2005**, *5* (5), 718–722.

(33) Hess, H.; Clemmens, J.; Brunner, C.; Doot, R.; Luna, S.; Ernst, K. H.; Vogel, V. Molecular Self-Assembly of “Nanowires” and “Nanospools” Using Active Transport. *Nano Lett.* **2005**, *5*, 629–633.

(34) Liu, H.; Spoerke, E. D.; Bachand, M.; Koch, S. J.; Bunker, B. C.; Bachand, G. D. Biomolecular Motor-Powered Self-Assembly of Dissipative Nanocomposite Rings. *Adv. Mater*. **2008**, *20* (23).

(35) Liu, H.; Bachand, G. D. Effects of Confinement on Molecular Motor-Driven Self-Assembly of Ring Structures. *Cell. Mol. Bioeng.* **2013**, *6* (1), 98–108.

(36) Korten, T.; Chaudhuri, S.; Tavkin, E.; Braun, M.; Diez, S. Kinesin-1 Expressed in Insect Cells Improves Microtubule in Vitro Gliding Performance, Long-Term Stability and Guiding Efficiency in Nanostructures. *IEEE Trans. Nanobioscience* **2016**, *15* (1), 62–69.

(37) Wintrebert, P. La Rotation Immédiate de l’oeuf Pondu et La Rotation d’activation Chez Discoglossus Pictus Otth. *C. R. Soc. Biol.* **1931**, *106*, 439–442.

(38) Celler, K.; Koning, R. I.; Koster, A. J.; van Wezel, G. P. Multidimensional View of the Bacterial Cytoskeleton. *Journal of Bacteriology*. **2013**, pp 1627–1636.

(39) Alberts, B.; Johnson, A.; Lewis, J.; Raff, M.; Roberts, K.; Walter, P. *Molecular Biology of the Cell*, 4th ed.; Gargland Science: New York, **2002**.

(40) Howard, J. *Mechanics of Motor Proteins and the Cytoskeleton*; Sinauer: Sunderland, MA, **2001**.

(41) Ingerson-Mahar, M.; Gitai, Z. A Growing Family: The Expanding Universe of the Bacterial Cytoskeleton. *FEMS Microbiology Reviews*. **2012**, pp 256–267.

(42) Callaway, E. Cell Biology: Bacteria’s New Bones. *Nature*. **2008**, pp 124–126.

(43) Pilhofer, M.; Jensen, G. J. The Bacterial Cytoskeleton: More than Twisted Filaments. *Current Opinion in Cell Biology*. **2013**, pp 1–9.

(44) Lin, L.; Thanbichler, M. Nucleotide-Independent Cytoskeletal Scaffolds in Bacteria. *Cytoskeleton* **2013**, *70* (8), 409–423.

(45) Bachand, G. D.; Bouxsein, N. F.; VanDelinder, V.; Bachand, M. Biomolecular Motors in Nanoscale Materials, Devices, and Systems. *Wiley Interdiscip. Rev. Nanomedicine Nanobiotechnology* **2014**, *6* (2), 163–177.

(46) Bachand, G. D.; Spoerke, E. D.; Stevens, M. J. Microtubule-Based

Nanomaterials: Exploiting Nature’s Dynamic Biopolymers. *Biotechnol. Bioeng.* **2015**.

(47) Burns, R. G. Alpha-, Beta-, and Gamma-Tubulins: Sequence Comparisons and Structural Constraints. *Cell Motil. Cytoskeleton* **1991**, *20* (3), 181–189.

(48) Nogales, E.; Wolf, S. G.; Downing, K. H. Structure of the Ab Tubulin Dimer by Electron Crystallography. *Nature* **1998**, *391* (6663), 199–203.

(49) Nogales, E.; Whittaker, M.; Milligan, R. A.; Downing, K. H. High-Resolution Model of the Microtubule. *Cell* **1999**, *96* (1), 79–88.

(50) Bachand, M.; Bouxsein, N. F.; Cheng, S.; von Hoyningen-Huene, S. J.; Stevens, M. J.; Bachand, G. D. Directed Self-Assembly of 1D Microtubule Nano-Arrays. *RSC Adv.* **2014**, *4* (97), 54641–54649.

(51) Desai, A.; Mitchison, T. J. Microtubule Polymerization Dynamics. *Annu. Rev. Cell Dev. Biol.* **1997**, *13* (1), 83–117.

(52) Kozielski, F.; Arnal, I.; Wade, R. H. A Model of the Microtubule-Kinesin Complex Based on Electron Cryomicroscopy and X-Ray Crystallography. *Curr. Biol.* **1998**, *8* (4), 191–198.

(53) Ray, S.; Meyhöfer, E.; Milligan, R. A.; Howard, J.; Meyhoefer, E.; Milligan, R. A.; Howard, J. Kinesin Follows the Microtubule’s Protofilament Axis. *J. Cell Biol.* **1993**, *121* (5), 1083–1093.

(54) Chretien, D.; Metoz, F.; Verde, F.; Karsenti, E.; Wade, R. H. Lattice Defects in Microtubules: Protofilament Numbers Vary within Individual Microtubules. *J. Cell Biol.* **1992**, *117* (5), 1031–1040.

(55) Kozielski, F.; Sack, S.; Marx, A.; Thormählen, M.; Schönbrunn, E.; Biou, V.; Thompson, A.; Mandelkow, E. M.; Mandelkow, E. The Crystal Structure of Dimeric Kinesin and Implications for Microtubule-Dependent Motility. *Cell* **1997**.

(56) Pampaloni, F.; Florin, E. L. Microtubule Architecture: Inspiration for Novel Carbon Nanotube-Based Biomimetic Materials. *Trends Biotechnol.* **2008**, *26* (6), 302–310.

(57) Drabik, P.; Gusarov, S.; Kovalenko, A. Microtubule Stability Studied by Three-Dimensional Molecular Theory of Solvation. *Biophys. J.* **2007**, *92* (2), 394–403.

(58) VanBuren, V.; Odde, D. J.; Cassimeris, L. Estimates of Lateral and Longitudinal Bond Energies within the Microtubule Lattice. *Proc. Natl. Acad. Sci.* **2002**, *99* (9), 6035–6040.

(59) Hawkins, T.; Mirigian, M.; Selcuk Yasar, M.; Ross, J. L. Mechanics of Microtubules. *J. Biomech.* **2010**, *43* (1), 23–30.

(60) Kim, T.; Kao, M. T.; Hasselbrink, E. F.; Meyhöfer, E. Nanomechanical Model of Microtubule Translocation in the Presence of Electric Fields. *Biophys. J.* **2008**, *94* (10), 3880–3892.

(61) Stracke, R.; Böhm, K. J.; Wollweber, L.; Tuszynski, J. A.; Unger, E.

Analysis of the Migration Behaviour of Single Microtubules in Electric Fields. *Biochem. Biophys. Res. Commun.* **2002**, *293* (1), 602–609.

(62) Baker, N. A.; Sept, D.; Joseph, S.; Holst, M. J.; McCammon, J. A. Electrostatics of Nanosystems: Application to Microtubules and the Ribosome. *Proc. Natl. Acad. Sci.* **2001**, *98* (18), 10037–10041.

(63) Mitchison, T.; Kirschner, M. Dynamic Instability of Microtubule Growth. *Nature* **1984**, *312* (5991), 237–242.

(64) Alushin, G. M.; Lander, G. C.; Kellogg, E. H.; Zhang, R.; Baker, D.; Nogales, E. High-Resolution Microtubule Structures Reveal the Structural Transitions in Aβ-Tubulin upon GTP Hydrolysis. *Cell,* **2014**, *157* (5), 1117–1129.

(65) Dimitrov, A.; Quesnoit, M.; Moutel, S.; Cantaloube, I.; Poüs, C.; Perez, F. Detection of GTP-Tubulin Conformation in Vivo Reveals a Role for GTP Remnants in Microtubule Rescues. *Science.* **2008**, *322* (5906), 1353–1356.

(66) Cassimeris, L. Regulation of Microtubule Dynamic Instability. *Cell Motil. Cytoskeleton* **1993**, *26* (4), 275–281.

(67) Schiff, P. B.; Fant, J.; Horwitz, S. B. Promotion of Microtubule Assembly in Vitro by Taxol. *Nature* **1979**, *277* (5698), 665–667.

(68) Hess, H.; Ross, J. L. *Non-Equilibrium Assembly of Microtubules: From Molecules to Autonomous Chemical Robots*; Royal Society of Chemistry, **2017**; Vol. 46, pp 5570–5587.

(69) Lewin, B.; Cassimeris, L.; Vishwanath, L. R.; Plopper, G. Microtubules. In *Cells*; Jones and Bartlett Publishers: Sudbury, Massachusetts, **2007**; pp 1–54.

(70) Dogterom, M.; Kerssemakers, J. W. J.; Romet-Lemonne, G.; Janson, M. E. Force Generation by Dynamic Microtubules. *Curr. Opin. Cell Biol.* **2005**, *17* (1), 67–74.

(71) Howard, J. Elastic and Damping Forces Generated by Confined Arrays of Dynamic Microtubules. *Phys. Biol.* **2006**, *3* (1), 54–66.

(72) Allen, R. D.; Metuzals, J.; Tasaki, I.; Brady, S. T.; Gilbert, S. P. Fast Axonal Transport in Squid Giant Axon. *Science.* **1982**, *218* (4577), 1127–1129.

(73) Brady, S. T.; Lasek, R. J.; Allen, R. D. Fast Axonal Transport in Extruded Axoplasm from Squid Giant Axon. *Science* **1982**, *218* (4577), 1129–1131.

(74) Vale, R. D.; Reese, T. S.; Sheetz, M. P. Identification of a Novel Force-Generating Protein, Kinesin, Involved in Microtubule-Based Motility. *Cell* **1985**, *42* (1), 39–50.

(75) Endow, S. A.; Kull, F. J.; Liu, H. Kinesins at a Glance. *J. Cell Sci.* **2010**, *123* (20), 3420–3424.

(76) Hirokawa, N.; Noda, Y.; Tanaka, Y.; Niwa, S. Kinesin Superfamily Motor Proteins and Intracellular Transport. *Nat. Rev. Mol. Cell Biol.* **2009**, *10* (10),

682–696.

(77) Gunawardena, S.; Goldstein, L. S. B. Cargo-Carrying Motor Vehicles on the Neuronal Highway: Transport Pathways and Neurodegenerative Disease. *Journal of Neurobiology*. **2004**, pp 258–271.

(78) Sharp, D. J.; Rogers, G. C.; Scholey, J. M. Microtubule Motors in Mitosis. *Nature*. **2000**, pp 41–47.

(79) Insinna, C.; Besharse, J. C. Intraflagellar Transport and the Sensory Outer Segment of Vertebrate Photoreceptors. *Developmental Dynamics*. **2008**, pp 1982–1992.

(80) Saxton, W. M.; Hicks, J.; Goldstein, L. S. B.; Raff, E. C. Kinesin Heavy Chain Is Essential for Viability and Neuromuscular Functions in Drosophila, but Mutants Show No Defects in Mitosis. *Cell* **1991**, *64* (6), 1093–1102.

(81) Hurd, D. D.; Saxton, W. M. Kinesin Mutations Cause Motor Neuron Disease Phenotypes by Disrupting Fast Axonal Transport in Drosophila. *Genetics* **1996**, *144* (3), 1075–1085.

(82) Reid, E.; Kloos, M.; Ashley-Koch, A.; Hughes, L.; Bevan, S.; Svenson, I. K.; Graham, F. L.; Gaskell, P. C.; Dearlove, A.; Pericak-Vance, M. A.; et al. A Kinesin Heavy Chain (KIF5A) Mutation in Hereditary Spastic Paraplegia (SPG10). *Am. J. Hum. Genet.* **2002**, *71* (5), 1189–1194.

(83) Gerdes, J. M.; Katsanis, N. Microtubule Transport Defects in Neurological and Ciliary Disease. *Cellular and Molecular Life Sciences*. **2005**, pp 1556–1570.

(84) Dagenbach, E. M.; Endow, S. A. A New Kinesin Tree. *J. Cell Sci.* **2004**, *117* (Pt 1), 3–7.

(85) Lawrence, C. J.; Dawe, R. K.; Christie, K. R.; Cleveland, D. W.; Dawson, S. C.; Endow, S. A.; Goldstein, L. S. B.; Goodson, H. V.; Hirokawa, N.; Howard, J.; et al. A Standardized Kinesin Nomenclature. *Journal of Cell Biology*. **2004**, pp 19–22.

(86) Block, S. M. Kinesin Motor Mechanics: Binding, Stepping, Tracking, Gating, and Limping. *Biophys. J.* **2007**.

(87) Hirokawa, N.; Pfister, K. K.; Yorifuji, H.; Wagner, M. C.; Brady, S. T.; Bloom, G. S. Submolecular Domains of Bovine Brain Kinesin Identified by Electron Microscopy and Monoclonal Antibody Decoration. *Cell* **1989**, *56* (5), 867–878.

(88) Kull, F. J.; Sablin, E. P.; Lau, R.; Fletterick, R. J.; Vale, R. D. Crystal Structure of the Kinesin Motor Domain Reveals a Structural Similarity to Myosin. *Nature* **1996**, *380* (6574), 550–555.

(89) Sablin, E. P.; Kull, F. J.; Cooke, R.; Vale, R. D.; Fletterick, R. J. Crystal Structure of the Motor Domain of the Kinesin-Related Motor Ncd. *Nature* **1996**, *380* (6574), 555–559.

(90) Hackney, D. D.; Stock, M. F. Kinesin's IAK Tail Domain Inhibits Initial

Microtubule-Stimulated ADP Release. *Nat. Cell Biol.* **2000**, *2* (5), 257–260.

(91) Hunt, A. J.; Howard, J. Kinesin Swivels to Permit Microtubule Movement in Any Direction. *Proc. Natl. Acad. Sci.* **1993**, *90* (December), 11653–11657.

(92) Terada, S.; Hirokawa, N. Moving on to the Cargo Problem of Microtubule-Dependent Motors in Neurons. *Current Opinion in Neurobiology*. **2000**, pp 566–573.

(93) Kawaguchi, K.; Ishiwata, S. Temperature Dependence of Force, Velocity, and Processivity of Single Kinesin Molecules. *Biochem. Biophys. Res. Commun.* **2000**, *272* (3), 895–899.

(94) Hancock, W. O.; Howard, J. Kinesin's Processivity Results from Mechanical and Chemical Coordination between the ATP Hydrolysis Cycles of the Two Motor Domains. *Proc. Natl. Acad. Sci.* **1999**, *96* (23), 13147–13152.

(95) Block, S. M.; Goldstein, L. S. B.; Schnapp, B. J. Bead Movement by Single Kinesin Molecules Studied with Optical Tweezers. *Nature* **1990**, *348* (6299), 348–352.

(96) Hackney, D. D. Highly Processive Microtubule-Stimulated ATP Hydrolysis by Dimeric Kinesin Head Domains. *Nature* **1995**, *377* (6548), 448–450.

(97) Case, R. B.; Rice, S.; Hart, C. L.; Ly, B.; Vale, R. D. Role of the Kinesin Neck Linker and Catalytic Core in Microtubule-Based Motility. *Curr. Biol.* **2000**, *10* (3), 157–160.

(98) Coy, D. L.; Wagenbach, M.; Howard, J. Kinesin Takes One 8-Nm Step for Each ATP That It Hydrolyzes. *J. Biol. Chem.* **1999**, *274* (6), 3667–3671.

(99) Asbury, C. L.; Fehr, A. N.; Block, S. M. Kinesin Moves by an Asymmetric Hand-Over-Hand Mechanism. *Science (80-.).* **2003**, *302* (5653), 2130–2134.

(100) Asbury, C. L. Kinesin: World&apos;s Tiniest Biped. *Curr Opin Cell Biol* **2005**, *17* (1), 89–97.

(101) Svoboda, K.; Schmidt, C. F.; Schnapp, B. J.; Block, S. M. Direct Observation of Kinesin Stepping by Optical Trapping Interferometry. *Nature* **1993**, *365* (6448), 721–727.

(102) Schnitzer, M. J.; Block, S. M. Kinesin Hydrolyses One ATP per 8-Nm Step. *Nature* **1997**, *388* (6640), 386–390.

(103) Kaseda, K.; Higuchi, H.; Hirose, K. Alternate Fast and Slow Stepping of a Heterodimeric Kinesin Molecule. *Nat. Cell Biol.* **2003**, *5* (12), 1079–1082.

(104) Higuchi, H.; Bronner, C. E.; Park, H. W.; Endow, S. A. Rapid Double 8-Nm Steps by a Kinesin Mutant. *EMBO J.* **2004**, *23* (15), 2993–2999.

(105) Yildiz, A.; Tomishige, M.; Vale, R. D.; Selvin, P. R. Kinesin Walks Hand-Over-Hand. *Science (80-.).* **2004**, *303* (5658), 676–678.

(106) Kron, S. J.; Spudich, J. a. Fluorescent Actin Filaments Move on Myosin Fixed to a Glass Surface. *Proc. Natl. Acad. Sci. U. S. A.* **1986**, *83* (17),

6272–6276.

(107) Kron, S. J.; Toyoshima, Y. Y.; Uyeda, T. Q. P.; Spudich, J. A. Assays for Actin Sliding Movement over Myosin-Coated Surfaces. *Methods Enzymol.* **1991**, *196* (C), 399–416.

(108) Howard, J.; Hunt, A. J.; Baek, S. Assay of Microtubule Movement Driven by Single Kinesin Molecules. *Methods Cell Biol.* **1993**, *39* (C), 137–147.

(109) Proteins, A.; Motors, B.; Nanostructures, E. Dynamic and Active Proteins : In Engineered Nanostructures. **2016**.

(110) Galland, R.; Leduc, P.; Guérin, C.; Peyrade, D.; Blanchoin, L.; Théry, M. Fabrication of Three-Dimensional Electrical Connections by Means of Directed Actin Self-Organization. *Nat. Mater.* **2013**, *12* (5), 416–421.

(111) Behrens, S.; Rahn, K.; Habicht, W.; Böhm, K. J.; Rösner, H.; Dinjus, E.; Unger, E. Nanoscale Particle Arrays Induced by Highly Ordered Protein Assemblies. *Adv. Mater.* **2002**, *14* (22), 1621–1625.

(112) Gazit, E. Use of Biomolecular Templates for the Fabrication of Metal Nanowires. *FEBS Journal*. **2007**, pp 317–322.

(113) Patolsky, F.; Weizmann, Y.; Willner, I. Actin-Based Metallic Nanowires as Bio-Nanotransporters. *Nat. Mater.* **2004**, *3* (10), 692–695.

(114) Behrens, S.; Wu, J.; Habicht, W.; Unger, E. Silver Nanoparticle and Nanowire Formation by Microtubule Templates. *Chem. Mater.* **2004**, *16* (16), 3085–3090.

(115) Boal, A. K.; Headley, T. J.; Tissot, R. G.; Bunker, B. C. Microtubule-Templated Biomimetic Mineralization of Lepidocrocite. *Adv. Funct. Mater.* **2004**, *14* (1), 19–24.

(116) Dinu, C. Z.; Bale, S. S.; Zhu, G.; Dordick, J. S. Tubulin Encapsulation of Carbon Nanotubes into Functional Hybrid Assemblies. *Small* **2009**, *5* (3), 310–315.

(117) Böhm, K. J.; Stracke, R.; Unger, E. Speeding up Kinesin-Driven Microtubule Gliding in Vitro by Variation of Cofactor Composition and Physicochemical Parameters. *Cell Biol. Int.* **2000**, *24* (6), 335–341.

(118) Wang, F.; Chen, L.; Arcucci, O.; Harvey, E. V.; Bowers, B.; Xu, Y.; Hammer, J. A.; Sellers, J. R. Effect of ADP and Ionic Strength on the Kinetic and Motile Properties of Recombinant Mouse Myosin V. *J. Biol. Chem.* **2000**, *275* (6), 4329–4335.

(119) Kerssemakers, J. W. J.; Laura Munteanu, E.; Laan, L.; Noetzel, T. L.; Janson, M. E.; Dogterom, M. Assembly Dynamics of Microtubules at Molecular Resolution. *Nature* **2006**, *442* (7103), 709–712.

(120) Finer, J. T.; Simmons, R. M.; Spudich, J. A. Single Myosin Molecule Mechanics: Piconewton Forces and Nanometre Steps. *Nature* **1994**, *368* (6467), 113–119.

(121) Reck-Peterson, S. L.; Yildiz, A.; Carter, A. P.; Gennerich, A.; Zhang, N.;

Vale, R. D. Single-Molecule Analysis of Dynein Processivity and Stepping Behavior. *Cell* **2006**, *126* (2), 335–348.

(122) Yildiz, A.; Forkey, J. N.; McKinney, S. A.; Ha, T.; Goldman, Y. E.; Selvin, P. R. Myosin V Walks Hand-over-Hand: Single Fluorophore Imaging with 1.5-Nm Localization. *Science (80-.).* **2003**, *300* (5628), 2061–2065.

(123) Arai, Y.; Yasuda, R.; Akashi, K. I.; Harada, Y.; Miyata, H.; Kinosita, K.; Itoh, H. Tying a Molecular Knot with Optical Tweezers. *Nature* **1999**, *399* (6735), 446–448.

(124) Sakakibara, H.; Kojima, H.; Sakai, Y.; Katayama, E.; Oiwa, K. Inner-Arm Dynein c of Chlamydomonas Flagella Is a Single-Headed Processive Motor. *Nature* **1999**, *400* (6744), 586–590.

(125) Müller, M. J. I.; Klumpp, S.; Lipowsky, R. Tug-of-War as a Cooperative Mechanism for Bidirectional Cargo Transport by Molecular Motors. **2008**, No. 12.

(126) Klumpp, S.; Lipowsky, R. Cooperative Cargo Transport by Several Molecular Motors. *Proc. Natl. Acad. Sci.* **2005**, *102* (48), 17284–17289.

(127) Harada, Y.; Sakurada, K.; Aoki, T.; Thomas, D. D.; Yanagida, T. Mechanochemical Coupling in Actomyosin Energy Transduction Studied by in Vitro Movement Assay. *J. Mol. Biol.* **1990**, *216* (1), 49–68.

(128) Katira, P.; Agarwal, A.; Fischer, T.; Chen, H. Y.; Jiang, X.; Lahann, J.; Hess, H. Quantifying the Performance of Protein-Resisting Surfaces at Ultra-Low Protein Coverages Using Kinesin Motor Proteins as Probes. *Adv. Mater.* **2007**, *19* (20), 3171–3176.

(129) Katira, P.; Hess, H. Two-Stage Capture Employing Active Transport Enables Sensitive and Fast Biosensors. *Nano Lett.* **2010**, *10* (2), 567–572.

(130) Nitta, T.; Hess, H. Dispersion in Active Transport by Kinesin-Powered Molecular Shuttles. *Nano Lett.* **2005**, *5* (7), 1337–1342.

(131) Nitta, T.; Tanahashi, A.; Obara, Y.; Hirano, M.; Razumova, M.; Regnier, M.; Hess, H. Comparing Guiding Track Requirements for Myosin-and Kinesin-Powered Molecular Shuttles. *Nano Lett.* **2008**, *8* (8), 2305–2309.

(132) Riveline, D.; Ott, A.; Jülicher, F.; Winkelmann, D. A.; Cardoso, O.; Lacapère, J. J.; Magnúsdóttir, S.; Viovy, J. L.; Gorre-Talini, L.; Prost, J. Acting on Actin: The Electric Motility Assay. *Eur. Biophys. J.* **1998**, *27* (4), 403–408.

(133) Clemmens, J.; Hess, H.; Lipscomb, R.; Hanein, Y.; Böhringer, K. F.; Matzke, C. M.; Bachand, G. D.; Bunker, B. C.; Vogel, V. Mechanisms of Microtubule Guiding on Microfabricated Kinesin-Coated Surfaces: Chemical and Topographic Surface Patterns. *Langmuir* **2003**, *19* (26), 10967–10974.

(134) Sundberg, M.; Bunk, R.; Albet-Torres, N.; Kvennefors, A.; Persson, F.; Montelius, L.; Nicholls, I. A.; Ghatnekar-Nilsson, S.; Omling, P.; Tågerud, S.; et al. Actin Filament Guidance on a Chip: Toward High-Throughput

Assays and Lab-on-a-Chip Applications. *Langmuir* **2006**, *22* (17), 7286–7295.

(135) Suzuki, H.; Oiwa, K.; Yamada, A.; Sakakibara, H.; Nakayama, H.; Mashiko, S. Linear Arrangement of Motor Protein on a Mechanically Deposited Fluoropolymer Thin Film. *Jpn. J. Appl. Phys.* **1995**, *34* (7S), 3937–3941.

(136) Clemmens, J.; Hess, H.; Howard, J.; Vogel, V. Analysis of Microtubule Guidance in Open Microfabricated Channels Coated with the Motor Protein Kinesin. *Langmuir* **2003**, *19* (5), 1738–1744.

(137) Stracke, R.; Böhm, K. J.; Burgold, J.; Schacht, H. J.; Unger, E. Physical and Technical Parameters Determining the Functioning of a Kinesin-Based Cell-Free Motor System. *Nanotechnology* **2000**, *11* (2), 52–56.

(138) Kerssemakers, J.; Ionov, L.; Queitsch, U.; Luna, S.; Hess, H.; Diez, S. 3D Nanometer Tracking of Motile Microtubules on Reflective Surfaces. *Small* **2009**, *5* (15), 1732–1737.

(139) Doot, R. K.; Hess, H.; Vogel, V. Engineered Networks of Oriented Microtubule Filaments for Directed Cargo Transport. *Soft Matter* **2007**, *3* (3), 349–356.

(140) Hess, H.; Matzke, C. M.; Doot, R. K.; Clemmens, J.; Bachand, G. D.; Bunker, B. C.; Vogel, V. Molecular Shuttles Operating Undercover: A New Photolithographic Approach for the Fabrication of Structured Surfaces Supporting Directed Motility. *Nano Lett.* **2003**, *3* (12), 1651–1655.

(141) Bunk, R.; Sundberg, M.; Månsson, A.; Nicholls, I. A.; Omling, P.; T̊gerud, S.; Montelius, L. Guiding Motor-Propelled Molecules with Nanoscale Precision through Silanized Bi-Channel Structures. *Nanotechnology* **2005**, *16* (6), 710–717.

(142) Clemmens, J.; Hess, H.; Doot, R.; Matzke, C. M.; Bachand, G. D.; Vogel, V. Motor-Protein “Roundabouts”: Microtubules Moving on Kinesin-Coated Tracks through Engineered Networks. *Lab Chip* **2004**, *4* (2), 83–86.

(143) Hiratsuka, Y.; Tada, T.; Oiwa, K.; Kanayama, T.; Uyeda, T. Q. Controlling the Direction of Kinesin-Driven Microtubule Movements along Microlithographic Tracks. *Biophys. J.* **2001**, *81* (3), 1555–1561.

(144) Hess, H.; Clemmens, J.; Matzke, C. M.; Bachand, G. D.; Bunker, B. C.; Vogel, V. Ratchet Patterns Sort Molecular Shuttles. *Appl. Phys. A Mater. Sci. Process.* **2002**, *75* (2), 309–313.

(145) Lin, C. T.; Kao, M. T.; Kurabayashi, K.; Meyhöfer, E. Efficient Designs for Powering Microscale Devices with Nanoscale Biomolecular Motors. *Small* **2006**, *2* (2), 281–287.

(146) Hess, H.; Clemmens, J.; Howard, J.; Vogel, V. Surface Imaging by Self-Propelled Nanoscale Probes. *Nano Lett.* **2002**, *2* (2), 113–116.

(147) Lipscomb, R. C.; Clemmens, J.; Hanein, Y.; Holl, M. R.; Vogel, V.; Ratner, B. D.; Denton, D. D.; Böhringer, K. F. Controlled Microtubules Transport on Patterned Non-Fouling Surfaces. In *2nd Annual International IEEE-EMBS*

Special Topic Conference on Microtechnologies in Medicine and Biology - Proceedings; **2002**; pp 21–26.

(148) Romet-Lemonne, G.; VanDuijn, M.; Dogterom, M. Three-Dimensional Control of Protein Patterning in Microfabricated Devices. *Nano Lett.* **2005**, *5* (12), 2350–2354.

(149) Reuther, C.; Hajdo, L.; Tucker, R.; Kasprzak, A. A.; Diez, S. Biotemplated Nanopatterning of Planar Surfaces with Molecular Motors. *Nano Lett.* **2006**, *6* (10), 2177–2183.

(150) Cheng, L. J.; Kao, M. T.; Meyhöfer, E.; Guo, L. J. Highly Efficient Guiding of Microtubule Transport with Imprinted CYTOP Nanotracks. *Small* **2005**, *1* (4), 409–414.

(151) Van Den Heuvel, M. G. L.; Butcher, C. T.; Smeets, R. M. M.; Diez, S.; Dekker, C. High Rectifying Efficiencies of Microtubule Motility on Kinesin-Coated Gold Nanostructures. *Nano Lett.* **2005**, *5* (6), 1117–1122.

(152) Hirokawa, N.; Takemura, R. Molecular Motors and Mechanisms of Directional Transport in Neurons. *Nature Reviews Neuroscience*. **2005**, pp 201–214.

(153) Huxley, H. E.; Sase, I.; Miyata, H.; Ishiwata, S.; Kinosita, K. Axial Rotation of Sliding Actin Filaments Revealed by Single-Fluorophore Imaging. *Proc. Natl. Acad. Sci. U. S. A.* **1997**, *94* (11), 5646–5650.

(154) Beausang, J. F.; Schroeder, H. W.; Nelson, P. C.; Goldman, Y. E. Twirling of Actin by Myosins II and V Observed via Polarized TIRF in a Modified Gliding Assay. *Biophys. J.* **2008**, *95* (12), 5820–5831.

(155) Platt, M.; Muthukrishnan, G.; Hancock, W. O.; Williams, M. E. Millimeter Scale Alignment of Magnetic Nanoparticle Functionalized Microtubules in Magnetic Fields. *J. Am. Chem. Soc.* **2005**, *127* (45), 15686–15687.

(156) Bachand, G. D.; Rivera, S. B.; Boal, A. K.; Gaudioso, J.; Liu, J.; Bunker, B. C. Assembly and Transport of Nanocrystal CdSe Quantum Dot Nanocomposites Using Microtubules and Kinesin Motor Proteins. *Nano Lett.* **2004**, *4* (5), 817–821.

(157) Hutchins, B. M.; Hancock, W. O.; Williams, M. E. Magnet Assisted Fabrication of Microtubule Arrays. *Phys. Chem. Chem. Phys.* **2006**, *8* (30), 3507–3509.

(158) Diez, S.; Reuther, C.; Dinu, C.; Seidel, R.; Mertig, M.; Pompe, W.; Howard, J. Stretching and Transporting DNA Molecules Using Motor Proteins. *Nano Lett.* **2003**, *3* (9), 1251–1254.

(159) Dinu, C. Z.; Opitz, J.; Pompe, W.; Howard, J.; Mertig, M.; Diez, S. Parallel Manipulation of Bifunctional DNA Molecules on Structured Surfaces Using Kinesin-Driven Microtubules. *Small* **2006**, *2* (8–9), 1090–1098.

(160) Yokokawa, R.; Miwa, J.; Tarhan, M. C.; Fujita, H.; Kasahara, M. DNA Molecule Manipulation by Motor Proteins for Analysis at the Single-Molecule Level. *Anal. Bioanal. Chem.* **2008**, *391* (8), 2735–2743.

(161) Taira, S.; Du, Y. Z.; Hiratsuka, Y.; Konishi, K.; Kubo, T.; Uyeda, T. Q. P.; Yumoto, N.; Kodaka, M. Selective Detection and Transport of Fully Matched DNA by DNA-Loaded Microtubule and Kinesin Motor Protein. *Biotechnol. Bioeng.* **2006**, *95* (3), 533–538.

(162) Dinu, C. Z.; Bale, S. S.; Chrisey, D. B.; Dordick, J. S. Manipulation of Individual Carbon Nanotubes by Reconstructing the Intracellular Transport of a Living Cell. *Adv. Mater.* **2009**, *21* (10–11), 1182–1186.

(163) Hutchins, B. M.; Platt, M.; Hancock, W. O.; Williams, M. E. Directing Transport of CoFe2O4-Functionalized Microtubules with Magnetic Fields. *Small*. **2007**, pp 126–131.

(164) Agarwal, A.; Katira, P.; Hess, H. Millisecond Curing Time of a Molecular Adhesive Causes Velocity-Dependent Cargo-Loading of Molecular Shuttles. *Nano Lett.* **2009**.

(165) Korten, T.; Diez, S. Setting up Roadblocks for Kinesin-1: Mechanism for the Selective Speed Control of Cargo Carrying Microtubules. *Lab Chip* **2008**, *8* (9), 1441–1447.

(166) Ramachandran, S.; Ernst, K. H.; Bachand, G. D.; Vogel, V.; Hess, H. Selective Loading of Kinesin-Powered Molecular Shuttles with Protein Cargo and Its Application to Biosensing. *Small* **2006**, *2* (3), 330–334.

(167) Hess, H. Self-Assembly Driven by Molecular Motors. *Soft Matter* **2006**, *2* (8), 669–677.

(168) Liu, H. Q.; Spoerke, E. D.; Bachand, M.; Koch, S. J.; Bunker, B. C.; Bachand, G. D. Biomolecular Motor-Powered Self-Assembly of Dissipative Nanocomposite Rings. *Adv. Mater.* **2008**, *20* (23), 4476–4481.

(169) Kawamura, R.; Kakugo, A.; Shikinaka, K.; Osada, Y.; Gong, J. P. Ring-Shaped Assembly of Microtubules Shows Preferential Counterclockwise Motion. *Biomacromolecules* **2008**, *9* (9), 2277–2282.

(170) Bachand, G. D.; Rivera, S. B.; Carroll-Portillo, A.; Hess, H.; Bachand, M. Active Capture and Transport of Virus Particles Using a Biomolecular Motor-Driven, Nanoscale Antibody Sandwich Assay. *Small* **2006**, *2* (3), 381–385.

(171) Soto, C. M.; Martin, B. D.; Sapsford, K. E.; Blum, A. S.; Ratna, B. R. Toward Single Molecule Detection of Staphylococcal Enterotoxin B: Mobile Sandwich Immunoassay on Gliding Microtubules. *Anal. Chem.* **2008**, *80* (14), 5433–5440.

(172) Rios, L.; Bachand, G. D. Multiplex Transport and Detection of Cytokines Using Kinesin-Driven Molecular Shuttles. *Lab Chip* **2009**, *9* (7), 1005–1010.

(173) Fischer, T.; Agarwal, A.; Hess, H. A Smart Dust Biosensor Powered by Kinesin Motors. *Nat. Nanotechnol.* **2009**, *4* (March), 162–166.

(174) Brunner, C.; Wahnes, C.; Vogel, V. Cargo Pick-up from Engineered Loading Stations by Kinesin Driven Molecular Shuttles. *Lab Chip* **2007**, *7*

(10), 1263–1271.

(175) Hiyama, S.; Gojo, R.; Shima, T.; Takeuchi, S.; Sutoh, K. Biomolecular-Motor-Based Nano- or Microscale Particle Translocations on DNA Microarrays. *Nano Lett.* **2009**, *9* (6), 2407–2413.

(176) Hirabayashi, M.; Taira, S.; Kobayashi, S.; Konishi, K.; Katoh, K.; Hiratsuka, Y.; Kodaka, M.; Uyeda, T. Q. P.; Yumoto, N.; Kubo, T. Malachite Green-Conjugated Microtubules as Mobile Bioprobes Selective for Malachite Green Aptamers with Capturing/Releasing Ability. *Biotechnol. Bioeng.* **2006**, *94* (3), 473–480.

(177) Fialkowski, M.; Bishop, K. J. M.; Klajn, R.; Smoukov, S. K.; Campbell, C. J.; Grzybowski, B. A. Principles and Implementations of Dissipative (Dynamic) Self-Assembly. *J. Phys. Chem. B* **2006**, *110* (6), 2482–2496.

(178) Lehn, J.-M. Toward Self-Organization and Complex Matter. *Science (80-.).* **2002**, *295* (5564), 2400–2403.

(179) Whitesides, G. M.; Grzybowski, B. *Self-Assembly at All Scales*; **2002**; Vol. 295, pp 2418–2421.

(180) Lam, A. T.-C.; VanDelinder, V.; Kabir, A. M. R.; Hess, H.; Bachand, G.; Kakugo, A. Cytoskeletal Motor-Driven Active Self-Assembly in in Vitro Systems. *Soft Matter* **2015**.

(181) Aoyama, S.; Shimoike, M.; Hiratsuka, Y. Self-Organized Optical Device Driven by Motor Proteins. *Proc. Natl. Acad. Sci.* **2013**, *110* (41), 16408–16413.

(182) Crenshaw, J. D.; Liang, T.; Hess, H.; Phillpot, S. R. A Cellular Automaton Approach to the Simulation of Active Self-Assembly of Kinesin-Powered Molecular Shuttles. *J. Comput. Theor. Nanosci.* **2011**, *8* (10), 1999–2005.

(183) Tamura, Y.; Kawamura, R.; Shikinaka, K.; Kakugo, A.; Osada, Y.; Gong, J. P.; Mayama, H. Dynamic Self-Organization and Polymorphism of Microtubule Assembly through Active Interactions with Kinesin. *Soft Matter* **2011**, *7* (12), 5654–5659.

(184) Hess, H.; Clemmens, J.; Brunner, C.; Doot, R.; Luna, S.; Ernst, K.; Vogel, V.; Uni, V. Molecular Self-Assembly of " Nanowires " and " Nanospools " Using Active Transport. **2005**, 0–4.

(185) Idan, O.; Lam, A.; Kamcev, J.; Gonzales, J.; Agarwal, A.; Hess, H. Nanoscale Transport Enables Active Self-Assembly of Millimeter-Scale Wires. *Nano Lett.* **2012**, *12* (1), 240–245.

(186) Kawamura, R.; Kakugo, A.; Osada, Y.; Gong, J. P. Microtubule Bundle Formation Driven by ATP: The Effect of Concentrations of Kinesin, Streptavidin and Microtubules. *Nanotechnology* **2010**, *21* (14), 145603.

(187) Kawamura, R.; Kakugo, A.; Osada, Y.; Gong, J. P. Selective Formation of a Linear-Shaped Bundle of Microtubules. *Langmuir* **2010**, *26* (1), 533–537.

(188) Dumont, E. L. P.; Do, C.; Hess, H. Molecular Wear of Microtubules

Propelled by Surface-Adhered Kinesins. *Nat. Nanotechnol.* **2015**, *10* (2), 166–169.

(189) Lam, a T.; Curschellas, C.; Krovvidi, D.; Hess, H. Controlling Self-Assembly of Microtubule Spools via Kinesin Motor Density. *Soft Matter* **2014**, *10* (43), 8731–8736.

(190) Kakugo, A.; Shikinaka, K.; Takekawa, N.; Sugimoto, S.; Osada, Y.; Gong, J. P. Polarity and Motility of Large Polymer-Actin Complexes. *Biomacromolecules* **2005**, *6* (2), 845–849.

(191) Kwon, K. Y.; Wong, K. L.; Pawin, G.; Bartels, L.; Stolbov, S.; Rahman, T. S. Unidirectional Adsorbate Motion on a High-Symmetry Surface: “Walking” Molecules Can Stay the Course. *Phys. Rev. Lett.* **2005**, *95* (16).

(192) Luria, I.; Crenshaw, J.; Downs, M.; Agarwal, A.; Seshadri, S. B.; Gonzales, J.; Idan, O.; Kamcev, J.; Katira, P.; Pandey, S.; et al. Microtubule Nanospool Formation by Active Self-Assembly Is Not Initiated by Thermal Activation. *Soft Matter* **2011**, *7* (7), 3108.

(193) Sanchez, T.; Welch, D.; Nicastro, D.; Dogic, Z. Cilia-like Beating of Active Microtubule Bundles. *Science (80-.).* **2011**, *333* (6041), 456–459.

(194) Bray, D. Cell Movements: From Molecules To Motility, 2Nd Edition. *Shock*. **2001**, p 327.

(195) Inoue, D.; Mahmot, B.; Kabir, A. M. R.; Farhana, T. I.; Tokuraku, K.; Sada, K.; Konagaya, A.; Kakugo, A. Depletion Force Induced Collective Motion of Microtubules Driven by Kinesin. *Nanoscale* **2015**, *7* (43), 18054–18061.

(196) Amos, L. A.; Amos, W. B. The Bending of Sliding Microtubules Imaged by Confocal Light Microscopy and Negative Stain Electron Microscopy. *J Cell Sci Suppl* **1991**, *14* (95), 95–101.

(197) Gittes, F.; Mickey, B.; Nettleton, J.; Howard, J. Flexural Rigidity of Microtubules and Actin Filaments Measured from Thermal Fluctuations in Shape. *J. Cell Biol.* **1993**, *120* (4), 923–934.

(198) Liu, H.; Bachand, G. D. Understanding Energy Dissipation and Thermodynamics in Biomotor-Driven Nanocomposite Assemblies. *Soft Matter* **2011**, *7* (7), 3087.

(199) Kakugo, A.; Kabir, A. M. R.; Hosoda, N.; Shikinaka, K.; Gong, J. P. Controlled Clockwise-Counterclockwise Motion of the Ring-Shaped Microtubules Assembly. *Biomacromolecules* **2011**, *12* (10), 3394–3399.

(200) Inoue, D.; Kabir, A. M. R.; Mayama, H.; Gong, J. P.; Sada, K.; Kakugo, A. Growth of Ring-Shaped Microtubule Assemblies through Stepwise Active Self-Organisation. *Soft Matter* **2013**, *9* (29), 7061.

(201) Liu, L.; Tüzel, E.; Ross, J. L. Loop Formation of Microtubules during Gliding at High Density. *J. Phys. Condens. Matter* **2011**, *23* (37), 374104.

(202) Ziebert, F.; Mohrbach, H.; Kulić, I. M. Why Microtubules Run in Circles - Mechanical Hysteresis of the Tubulin Lattice. **2014**, No. c, 5.

(203) Pierson, G. B.; Burton, P. R.; Himes, R. H. Alterations in Number of Protofilaments in Microtubules Assembled in Vitro. *J. Cell Biol.* **1978**, *76* (1), 223–228.

(204) Ito, M.; Kabir, A. M. R.; Inoue, D.; Torisawa, T.; Toyoshima, Y.; Sada, K.; Kakugo, A. Formation of Ring-Shaped Microtubule Assemblies through Active Self-Organization on Dynein. *Polym. J.* **2014**, *46* (4), 220–225.

(205) Wada, S.; Kabir, A. M. R.; Kawamura, R.; Ito, M.; Inoue, D.; Sada, K.; Kakugo, A. Controlling the Bias of Rotational Motion of Ring-Shaped Microtubule Assembly. *Biomacromolecules* **2015**.

(206) Wada, S.; Kabir, A. M. R.; Ito, M.; Inoue, D.; Sada, K.; Kakugo, A. Effect of Length and Rigidity of Microtubules on the Size of Ring-Shaped Assemblies Obtained through Active Self-Organization. *Soft Matter* **2015**, *11* (6), 1151–1157.

(207) Sumino, Y.; Nagai, K. H.; Shitaka, Y.; Tanaka, D.; Yoshikawa, K.; Chaté, H.; Oiwa, K. Large-Scale Vortex Lattice Emerging from Collectively Moving Microtubules. *Nature* **2012**, *483* (7390), 448–452.

(208) Askeland, D. R.; Fulay, P. P.; Wright, W. J. The Science and Engineering of Materials. *Stamford, CT Cengage Learn. c2011* **2011**, 944.

(209) Queisser, H. J.; Haller, E. E. Defects in Semiconductors: Some Fatal, Some Vital. *Science.* **1998**, *281* (5379), 945–950.

(210) Sun, C.; Hui, R.; Roller, J. Cathode Materials for Solid Oxide Fuel Cells: A Review. *J. Solid State Electrochem.* **2010**, *14* (7), 1125–1144.

(211) Szuromi, P.; Clery, D. Control and Use of Defects in Materials. *Science.* **1998**, *281* (5379), 939.

(212) William D. Callister, J.; David G. Rethwisch. *Materials Science and Engineering*, 9th ed.; John Wiley & Sons, Inc.: Hoboken, NJ, **2014**.

(213) Hager, M. D.; Greil, P.; Leyens, C.; Van Der Zwaag, S.; Schubert, U. S. Self-Healing Materials. *Adv. Mater.* **2010**, *22* (47), 5424–5430.

(214) Greenhalgh, D. G. The Role of Apoptosis in Wound Healing. *International Journal of Biochemistry and Cell Biology*. **1998**, pp 1019–1030.

(215) Yuan, Y. C.; Yin, T.; Rong, M. Z.; Zhang, M. Q. Self Healing in Polymers and Polymer Composites. Concepts, Realization and Outlook: A Review. *Express Polymer Letters*. **2008**, pp 238–250.

(216) Li, J.; Shklyaev, O. E.; Li, T.; Liu, W.; Shum, H.; Rozen, I.; Balazs, A. C.; Wang, J. Self-Propelled Nanomotors Autonomously Seek and Repair Cracks. *Nano Lett.* **2015**, *15* (10), 7077–7085.

(217) Block, S. M. Kinesin: What Gives? *Cell* **1998**, *93* (1), 5–8.

(218) Vale, R. D.; Milligan, R. A. The Way Things Move: Looking under the Hood of Molecular Motor Proteins. *Science*. **2000**, p 88.

(219) Böhm, K. J. Kinesin-Driven Transport in Cell-Free Environment. *Cell Biol. Int.* **2008**, *32* (5), 588–590.

(220) Mulder, B. M.; Janson, M. E. Biological Filaments: Self-Healing Microtubules. *Nat. Mater.* **2015**, *14* (11), 1080–1081.

(221) Boekhoven, J.; Hendriksen, W. E.; Koper, G. J. M.; Eelkema, R.; Esch, J. H. Van. Transient Self-Assembly of Active Materials Fueled by a Chemical Reaction. *Science (80-.).* **2015**, *349* (6252), 1075.

(222) Palacci, J.; Sacanna, S.; Abramian, A.; Barral, J.; Hanson, K.; Grosberg, A. Y.; Pine, D. J.; Chaikin, P. M. Artificial Rheotaxis. *Sci. Adv.* **2015**, *1* (4).

(223) Wang, J.; Manesh, K. M. Motion Control at the Nanoscale. *Small*. **2010**, pp 338–345.

(224) Sanchez, S.; Soler, L.; Katuri, J. Chemically Powered Micro- and Nanomotors. *Angew. Chemie - Int. Ed.* **2015**, *54* (5), 1414–1444.

(225) Wang, J. Can Man-Made Nanomachines Compete with Nature Biomotors? *ACS Nano* **2009**, *3* (1), 4–9.

(226) Kim, K.; Guo, J.; Xu, X.; Fan, D. L. Recent Progress on Man-Made Inorganic Nanomachines. *Small*. **2015**, pp 4037–4057.

(227) Ibele, M.; Mallouk, T. E.; Sen, A. Schooling Behavior of Light-Powered Autonomous Micromotors in Water. *Angew. Chemie - Int. Ed.* **2009**, *48* (18), 3308–3312.

(228) Bachand, G. D.; Hess, H.; Ratna, B.; Satir, P.; Vogel, V. “Smart Dust” Biosensors Powered by Biomolecular Motors. *Lab Chip* **2009**, *9* (12), 1661–1666.

(229) Schaedel, L.; John, K.; Gaillard, J. J.; Nachury, M. V.; Blanchoin, L.; Thery, M.; Théry, M. Microtubules Self-Repair in Response to Mechanical Stress. *Nat. Mater.* **2015**, *14* (September), 1156–1163.

(230) Cross, R. A. Microtubule Lattice Plasticity. *Current Opinion in Cell Biology*. **2019**.

(231) Chaudhuri, S.; Korten, T.; Korten, S.; Milani, G.; Lana, T.; te Kronnie, G.; Diez, S. Label-Free Detection of Microvesicles and Proteins by the Bundling of Gliding Microtubules. *Nano Lett.* **2017**, acs.nanolett.7b03619.

(232) Kaur, H.; Kumar, S.; Kukkar, D.; Kaur, I.; Singh, K.; Bharadwaj, L. M. Transportation of Drug-(Polystyrene Bead) Conjugate by Actomyosin Motor System. *J. Biomed. Nanotechnol.* **2010**, *6* (3), 279–286.

(233) VanDelinder, V.; Bachand, G. D. Photodamage and the Importance of Photoprotection in Biomolecular-Powered Device Applications. *Anal. Chem.* **2014**, *86* (1), 721–728.

(234) Schindelin, J.; Arganda-Carreras, I.; Frise, E.; Kaynig, V.; Longair, M.; Pietzsch, T.; Preibisch, S.; Rueden, C.; Saalfeld, S.; Schmid, B.; et al. Fiji: An Open Source Platform for Biological Image Analysis. *Nat. Methods* **2012**, *9* (7), 676–682.

(235) Longair, M. H.; Baker, D. a.; Armstrong, J. D. Simple Neurite Tracer: Open Source Software for Reconstruction, Visualization and Analysis of

Neuronal Processes. *Bioinformatics* **2011**, *27* (17), 2453–2454.

(236) Greene, A. C.; Bachand, M.; Gomez, A.; Stevens, M. J.; Bachand, G. D. Interactions Regulating the Head-to-Tail Directed Assembly of Biological Janus Rods. *Chem. Commun.* **2017**, *53*, 4493–4496.

(237) Williams, R. C.; Rone, L. a. End-to-End Joining of Microtubules: Kinetics in Crowded Solutions. *Protoplasma* **1988**, *145* (2–3), 200–203.

(238) Waterman-Storer, C. M.; Salmon, E. D. Actomyosin-Based Retrograde Flow of Microtubules in the Lamella of Migrating Epithelial Cells Influences Microtubule Dynamic Instability and Turnover and Is Associated with Microtubule Breakage and Treadmilling. *J. Cell Biol.* **1997**, *139* (2), 417–434.

(239) Carroll-Portillo, A.; Bachand, M.; Greene, A. C.; Bachand, G. D. In Vitro Capture, Transport, and Detection of Protein Analytes Using Kinesin-Based Nanoharvesters. *Small* **2009**.

(240) Montemagno, C.; Bachand, G. Constructing Nanomechanical Devices Powered by Biomolecular Motors. *Nanotechnology* **1999**.

(241) Bachand, G. D.; Montemagno, C. D. Constructing Organic/Inorganic NEMS Devices Powered by Biomolecular Motors. *Biomed. Microdevices* **2000**.

(242) Wang, M. D.; Schnitzer, M. J.; Yin, H.; Landick, R.; Gelles, J.; Block, S. M. Force and Velocity Measured for Single Molecules of RNA Polymerase. *Science (80-.).* **1998**.

(243) Verma, V.; Hancock, W. O.; Catchmark, J. M. Micro- and Nanofabrication Processes for Hybrid Synthetic and Biological System Fabrication. *IEEE Trans. Adv. Packag.* **2005**.

(244) Howard, J. The Movement of Kinesin Along Microtubules. *Annu. Rev. Physiol.* **2002**.

(245) Goel, A.; Vogel, V. Harnessing Biological Motors to Engineer Systems for Nanoscale Transport and Assembly. *Nature Nanotechnology*. 2008.

(246) Steuerwald, D.; Früh, S. M.; Griss, R.; Lovchik, R. D.; Vogel, V. Nanoshuttles Propelled by Motor Proteins Sequentially Assemble Molecular Cargo in a Microfluidic Device. *Lab Chip* **2014**, *14* (19), 3729–3738.

(247) Inoue, D.; Nitta, T.; Kabir, A. M. R.; Sada, K.; Gong, J. P.; Konagaya, A.; Kakugo, A. Sensing Surface Mechanical Deformation Using Active Probes Driven by Motor Proteins. *Nat. Commun.* **2016**.

(248) Hess, H.; Howard, J.; Vogel, V. A Piconewton Forcemeter Assembled from Microtubules and Kinesins. *Nano Lett.* **2002**.

(249) Nitzsche, B.; Ruhnow, F.; Diez, S. Quantum-Dot-Assisted Characterization of Microtubule Rotations during Cargo Transport. *Nat. Nanotechnol.* **2008**, *3* (9), 552–556.

(250) Ilic, B.; Craighead, H. G. Topographical Patterning of Chemically Sensitive

Biological Materials Using a Polymer-Based Dry Lift Off. *Biomed. Microdevices* **2000**.

(251) Kane, R. S.; Takayama, S.; Ostuni, E.; Ingber, D. E.; Whitesides, G. M. Patterning Proteins and Cells Using Soft Lithography. *Biomaterials* **1999**, *20* (23–24), 2363–2376.

(252) Thomas, C. A.; Springer, P. A.; Loeb, G. E.; Berwald-Netter, Y.; Okun, L. M. A Miniature Microelectrode Array to Monitor the Bioelectric Activity of Cultured Cells. *Exp. Cell Res.* **1972**.

(253) Gross, G. W.; Rhoades, B. K.; Azzazy, H. M. E.; Ming-Chi Wu. The Use of Neuronal Networks on Multielectrode Arrays as Biosensors. *Biosens. Bioelectron.* **1995**.

(254) Jung, D. R.; Cuttino, D. S.; Pancrazio, J. J.; Manos, P.; Cluster, T.; Sathanoori, R. S.; Aloi, L. E.; Coulombe, M. G.; Czarnaski, M. A.; Borkholder, D. A.; et al. Cell-Based Sensor Microelectrode Array Characterized by Imaging x-Ray Photoelectron Spectroscopy, Scanning Electron Microscopy, Impedance Measurements, and Extracellular Recordings. *J. Vac. Sci. Technol. A Vacuum, Surfaces, Film.* **1998**.

(255) Mrksich, M.; Whitesides, G. M. Patterning Self-Assembled Monolayers Using Microcontact Printing: A New Technology for Biosensors? *Trends in Biotechnology*. **1995**.

(256) Singhvi, R.; Kumar, A.; Lopez, G. P.; Stephanopoulos, G. N.; Wang, D. I. C.; Whitesides, G. M.; Ingber, D. E. Engineering Cell Shape and Function. *Science (80).* **1994**.

(257) Chen, C. S.; Mrksich, M.; Huang, S.; Whitesides, G. M.; Ingber, D. E. Geometric Control of Cell Life and Death. *Science (80).* **1997**.

(258) Hudalla, G. a.; Murphy, W. L. Chemically Well-Defined Self-Assembled Monolayers for Cell Culture: Toward Mimicking the Natural ECM. *Soft Matter* **2011**, *7* (20), 9561–9571.

(259) Chieh, H. F.; Su, F. C.; Liao, J. Der; Lin, S. C.; Chang, C. W.; Shen, M. R. Attachment and Morphology of Adipose-Derived Stromal Cells and Exposure of Cell-Binding Domains of Adsorbed Proteins on Various Self-Assembled Monolayers. *Soft Matter* **2011**, *7* (8), 3808–3817.

(260) Tidwell, C. D.; Ertel, S. I.; Ratner, B. D.; Tarasevich, B. J.; Atre, S.; Allara, D. L. Endothelial Cell Growth and Protein Adsorption on Terminally Functionalized, Self-Assembled Monolayers of Alkanethiolates on Gold. *Langmuir* **1997**, *13* (13), 3404–3413.

(261) Curran, J. M.; Chen, R.; Hunt, J. A. Controlling the Phenotype and Function of Mesenchymal Stem Cells in Vitro by Adhesion to Silane-Modified Clean Glass Surfaces. *Biomaterials* **2005**.

(262) Senaratne, W.; Andruzzi, L.; Ober, C. K. Self-Assembled Monolayers and Polymer Brushes in Biotechnology: Current Applications and Future Perspectives. *Biomacromolecules* **2005**, *6* (5), 2427–2448.

(263) Scotchford, C. A.; Gilmore, C. P.; Cooper, E.; Leggett, G. J.; Downes, S. Protein Adsorption and Human Osteoblast-like Cell Attachment and Growth on Alkylthiol on Gold Self-Assembled Monolayers. *J. Biomed. Mater. Res.* **2002**.

(264) Hasan, A.; Pandey, L. M. Kinetic Studies of Attachment and Re-Orientation of Octyltriethoxysilane for Formation of Self-Assembled Monolayer on a Silica Substrate. *Mater. Sci. Eng. C* **2016**.

(265) Chaki, N. K.; Vijayamohanan, K. Self-Assembled Monolayers as a Tunable Platform for Biosensor Applications. *Biosensors and Bioelectronics*. **2002**.

(266) Witt, D.; Klajn, R.; Barski, P.; Grzybowski, B. Applications, Properties and Synthesis of &#969;-Functionalized n-Alkanethiols and Disulfides - the Building Blocks of Self-Assembled Monolayers. *Curr. Org. Chem.* **2005**.

(267) Chang, C. W.; Liao, J. Der. Nano-Indentation at the Surface Contact Level: Applying a Harmonic Frequency for Measuring Contact Stiffness of Self-Assembled Monolayers Adsorbed on Au. *Nanotechnology* **2008**.

(268) Bain, C. D.; Whitesides, G. M. Formation of Two-Component Surfaces by the Spontaneous Assembly of Monolayers on Gold from Solutions Containing Mixtures of Organic Thiols. *J. Am. Chem. Soc.* **1988**.

(269) Creager, S. E.; Clarke, J. Contact-Angle Titrations of Mixed Omega-Mercaptoalkanoic Acid Alkanethiol Monolayers on Gold - Reactive Vs Nonreactive Spreading, and Chain-Length Effects on Surface Pk(a) Values. *Langmuir* **1994**, *10* (25), 3675–3683.

(270) Fears, K. P.; Creager, S. E.; Latour, R. A. Determination of the Surface PK of Carboxylic- and Amine-Terminated Alkanethiols Using Surface Plasmon Resonance Spectroscopy. *Langmuir* **2008**, *24* (3), 837–843.

(271) Pandey, L. M.; Pattanayek, S. K.; Delabouglise, D. Properties of Adsorbed Bovine Serum Albumin and Fibrinogen on Self Assembled Monolayers. *J. Phys. Chem. C* **2013**.

(272) Gruian, C.; Vanea, E.; Simon, S.; Simon, V. FTIR and XPS Studies of Protein Adsorption onto Functionalized Bioactive Glass. *Biochim. Biophys. Acta-Proteins Proteomics* **2012**, *1824* (7), 873–881.

(273) Kaehr, B.; Townson, J. L.; Kalinich, R. M.; Awad, Y. H.; Swartzentruber, B. S.; Dunphy, D. R.; Brinker, C. J. Cellular Complexity Captured in Durable Silica Biocomposites. *Proc. Natl. Acad. Sci. U. S. A.* **2012**, *109* (43), 17336–17341.

(274) Lou, Y.-R.; Kanninen, L.; Kaehr, B.; Townson, J. L.; Niklander, J.; Harjumäki, R.; Jeffrey Brinker, C.; Yliperttula, M. Silica Bioreplication Preserves Three-Dimensional Spheroid Structures of Human Pluripotent Stem Cells and HepG2 Cells. *Sci. Rep.* **2015**, *5* (February), 13635.

(275) Meyer, K. C.; Coker, E. N.; Bolintineanu, D. S.; Kaehr, B. Mechanically Encoded Cellular Shapes for Synthesis of Anisotropic Mesoporous Particles. *J. Am. Chem. Soc.* **2014**.

(276) Townson, J. L.; Lin, Y. S.; Chou, S. S.; Awad, Y. H.; Coker, E. N.; Brinker, C. J.; Kaehr, B. Synthetic Fossilization of Soft Biological Tissues and Their Shape-Preserving Transformation into Silica or Electron-Conductive Replicas. *Nat. Commun.* **2014**.

(277) Lee, J.; Choi, J.; Park, J. H.; Kim, M. H.; Hong, D.; Cho, H.; Yang, S. H.; Choi, I. S. Cytoprotective Silica Coating of Individual Mammalian Cells through Bioinspired Silicification. *Angew. Chemie - Int. Ed.* **2014**.

(278) Nowinski, A. K.; Sun, F.; White, A. D.; Keefe, A. J.; Jiang, S. Sequence, Structure, and Function of Peptide Self-Assembled Monolayers. *J. Am. Chem. Soc.* **2012**, *134* (13), 6000–6005.

(279) Wang, H.; Chen, S.; Li, L.; Jiang, S. Improved Method for the Preparation of Carboxylic Acid and Amine Terminated Self-Assembled Monolayers of Alkanethiolates. *Langmuir* **2005**, *21* (7), 2633–2636.

(280) Mendoza, S. M.; Arfaoui, I.; Zanarini, S.; Paolucci, F.; Rudolf, P. Improvements in the Characterization of the Crystalline Structure of Acid-Terminated Alkanethiol Self-Assembled Monolayers on Au(111). *Langmuir* **2007**, *23* (2), 582–588.

(281) Michael, K. E.; Vernekar, V. N.; Keselowsky, B. G.; Meredith, J. C.; Latour, R. A.; García, A. J. Adsorption-Induced Conformational Changes in Fibronectin Due to Interactions with Well-Defined Surface Chemistries. *Langmuir* **2003**, *19* (19), 8033–8040.

(282) Sumner, A. L.; Menke, E. J.; Dubowski, Y.; Newberg, J. T.; Penner, R. M.; Hemminger, J. C.; Wingen, L. M.; Brauers, T.; Finlayson-Pitts, B. J. The Nature of Water on Surfaces of Laboratory Systems and Implications for Heterogeneous Chemistry in the Troposphere. *Phys. Chem. Chem. Phys.* **2004**, 604–613.

(283) Sigal, G. B.; Mrksich, M.; Whitesides, G. M. Effect of Surface Wettability on the Adsorption of Proteins and Detergents. *J. Am. Chem. Soc.* **1998**, *120* (14), 3464–3473.

(284) Khan, M. M. T.; Ista, L. K.; Lopez, G. P.; Schuler, A. J. Experimental and Theoretical Examination of Surface Energy and Adhesion of Nitrifying and Heterotrophic Bacteria Using Self-Assembled Monolayers. *Environ. Sci. Technol.* **2011**, *45* (3), 1055–1060.

(285) Keselowsky, B. G.; Collard, D. M.; García, A. J. Surface Chemistry Modulates Fibronectin Conformation and Directs Integrin Binding and Specificity to Control Cell Adhesion. *J. Biomed. Mater. Res. Part A* **2003**, *66A* (2), 247–259.

(286) Rush, M. N.; Coombs, K. E.; Hedberg-Dirk, E. L. Surface Chemistry Regulates Valvular Interstitial Cell Differentiation in Vitro. *Acta Biomater.* **2015**, *28*, 76–85.

(287) Singh, J.; Whitten, J. E. Forces between Polymer Surfaces and Self-Assembled Monolayers. In *Journal of Macromolecular Science, Part A:*

Pure and Applied Chemistry; 2008; Vol. 45, pp 885–892.

(288) Baio, J. E.; Weidner, T.; Brison, J.; Graham, D. J.; Gamble, L. J.; Castner, D. G. Amine Terminated SAMs: Investigating Why Oxygen Is Present in These Films. *J. Electron Spectros. Relat. Phenomena* **2009**, *172* (1–3), 2–8.

(289) Wang, H.; Castner, D. G.; Ratner, B. D.; Jiang, S. Y. Probing the Orientation of Surface-Immobilized Immunoglobulin G by Time-of-Flight Secondary Ion Mass Spectrometry. *Langmuir* **2004**, *20* (5), 1877–1887.

(290) Chada, N.; Sigdel, K. P.; Sanganna Gari, R. R.; Matin, T. R.; Randall, L. L.; King, G. M. Glass Is a Viable Substrate for Precision Force Microscopy of Membrane Proteins. *Sci. Rep.* **2015**, *5*.

(291) Scotchford, C. a.; Cooper, E.; Leggett, G. J.; Downes, S. Growth of Human Osteoblast-like Cells on Alkanethiol on Gold Self-Assembled Monolayers: The Effect of Surface Chemistry. *J. Biomed. Mater. Res.* **1998**, *41* (3), 431–442.

(292) Jones, J. A.; Qin, L. A.; Meyerson, H.; Il, K. K.; Matsuda, T.; Anderson, J. M. Instability of Self-Assembled Monolayers as a Model Material System for Macrophage/FBGC Cellular Behavior. *J. Biomed. Mater. Res. - Part A* **2008**, *86* (1), 261–268.

(293) Schoenfisch, M. H.; Pemberton, J. E. Air Stability of Alkanethiol Self-Assembled Monolayers on Silver and Gold Surfaces. *J. Am. Chem. Soc.* **1998**, *120* (18), 4502–5413.

(294) Nelson, C. M.; Raghavan, S.; Tan, J. L.; Chen, C. S. Degradation of Micropatterned Surfaces by Cell-Dependent and -Independent Processes. *Langmuir* **2003**, *19* (5), 1493–1499.

(295) Flynn, N. T.; Tran, T. N. T.; Cima, M. J.; Langer, R. Long-Term Stability of Self-Assembled Monolayers in Biological Media. *Langmuir* **2003**, *19* (26), 10909–10915.

(296) Jiang, X.; Bruzewicz, D. A.; Thant, M. M.; Whitesides, G. M. Palladium as a Substrate for Self-Assembled Monolayers Used in Biotechnology. *Anal. Chem.* **2004**, *76* (20), 6116–6121.

(297) Dannenberger, O.; Weiss, K.; Himmel, H. J.; Jäger, B.; Buck, M.; Wöll, C. An Orientation Analysis of Differently Endgroup-Functionalised Alkanethiols Adsorbed on Au Substrates. *Thin Solid Films* **1997**, *307* (1–2), 183–191.

(298) Li, L. Y.; Chen, S. F.; Jiang, S. Y. Protein Adsorption on Alkanethiolate Self-Assembled Monolayers: Nanoscale Surface Structural and Chemical Effects. *Langmuir* **2003**, *19* (7), 2974–2982.

(299) Li, L.; Chen, S.; Jiang, S. Molecular-Scale Mixed Alkanethiol Monolayers of Different Terminal Groups on Au(111) by Low-Current Scanning Tunneling Microscopy. *Langmuir* **2003**, *19* (8), 3266–3271.

(300) Hasan, A.; Pattanayek, S. K.; Pandey, L. M. Effect of Functional Groups of

Self-Assembled Monolayers on Protein Adsorption and Initial Cell Adhesion. *ACS Biomater. Sci. Eng.* **2018**, *4* (9), 3224–3233.

(301) Pandey, L. M.; Pattanayek, S. K.; Delabouglise, D. Properties of Adsorbed Bovine Serum Albumin and Fibrinogen on Self-Assembled Monolayers. *J. Phys. Chem.* **2013**, *117* (12), 6151–6160.

(302) Pandey, L. M.; Pattanayek, S. K. Properties of Competitively Adsorbed BSA and Fibrinogen from Their Mixture on Mixed and Hybrid Surfaces. *Appl. Surf. Sci.* **2013**, *264*, 832–837.

(303) Hasan, A.; Waibhaw, G.; Pandey, L. M. Conformational and Organizational Insights into Serum Proteins during Competitive Adsorption on Self-Assembled Monolayers. *Langmuir* **2018**, *34* (28), 8178–8194.

(304) Sharma, I.; Pattanayek, S. K.; Aggarwal, V.; Ghosh, S. Morphology of Self Assembled Monolayers Using Liquid Phase Reaction on Silica and Their Effect on the Morphology of Adsorbed Insulin. *Appl. Surf. Sci.* **2017**, *405*, 503–513.

(305) Arima, Y.; Iwata, H. Effect of Wettability and Surface Functional Groups on Protein Adsorption and Cell Adhesion Using Well-Defined Mixed Self-Assembled Monolayers. *Biomaterials* **2007**, *28* (20), 3074–3082.

(306) Servagent-Noinville, S.; Revault, M.; Quiquampoix, H.; Baron, M. H. Conformational Changes of Bovine Serum Albumin Induced by Adsorption on Different Clay Surfaces: FTIR Analysis. *J. Colloid Interface Sci.* **2000**, *221* (2), 273–283.

(307) Dousseau, F.; Pézolet, M. Determination of the Secondary Structure Content of Proteins in Aqueous Solutions from Their Amide I and Amide II Infrared Bands. Comparison between Classical and Partial Least-Squares Methods. *Biochemistry* **1990**, *29* (37), 8771–8779.

(308) El-Ghannam, A.; Ducheyne, P.; Shapiro, I. M. Effect of Serum Proteins on Osteoblast Adhesion to Surface-Modified Bioactive Glass and Hydroxyapatite. *J. Orthop. Res.* **1999**, *17* (3), 340–345.

(309) Faucheux, N.; Schweiss, R.; Lützow, K.; Werner, C.; Groth, T. Self-Assembled Monolayers with Different Terminating Groups as Model Substrates for Cell Adhesion Studies. *Biomaterials* **2004**, *25* (14), 2721–2730.

(310) Keselowsky, B. G.; Collard, D. M.; García, A. J. Integrin Binding Specificity Regulates Biomaterial Surface Chemistry Effects on Cell Differentiation. *Proc. Natl. Acad. Sci. U. S. A.* **2005**, *102* (17), 5953–5957.

(311) Wertz, C. F.; Santore, M. M. Effect of Surface Hydrophobicity on Adsorption and Relaxation Kinetics of Albumin and Fibrinogen: Single-Species and Competitive Behavior. *Langmuir* **2001**, *17* (10), 3006–3016.

(312) Jung, S. Y.; Lim, S. M.; Albertorio, F.; Kim, G.; Gurau, M. C.; Yang, R. D.; Holden, M. A.; Cremer, P. S. The Vroman Effect: A Molecular Level Description of Fibrinogen Displacement. *J. Am. Chem. Soc.* **2003**, *125*

(42), 12782–12786.

(313) Sivaraman, B.; Fears, K. P.; Latour, R. A. Investigation of the Effects of Surface Chemistry and Solution Concentration on the Conformation of Adsorbed Proteins Using an Improved Circular Dichroism Method. *Langmuir* **2009**, *25* (5), 3050–3056.

(314) Mücksch, C.; Urbassek, H. M.; Christian, M.; Urbassek, H. M. Molecular Dynamics Simulation of Free and Forced BSA Adsorption on a Hydrophobic Graphite Surface. *Langmuir* **2011**, *27* (21), 12938–12943.

(315) Roach, P.; Farrar, D.; Perry, C. C. Interpretation of Protein Adsorption : Surface-Induced Conformational Changes Interpretation of Protein Adsorption : Surface-Induced Conformational Changes. *J. Am. Chem. Soc.* **2005**, *127* (22), 8168–8173.

(316) Vroman, L.; Adams, A. L. Identification of Rapid Changes at Plasma Solid Interfaces. *J. Biomed. Mater. Res.* **1969**, *3* (1), 43–67.

(317) Arima, Y.; Iwata, H. Preferential Adsorption of Cell Adhesive Proteins from Complex Media on Self-Assembled Monolayers and Its Effect on Subsequent Cell Adhesion. *Acta Biomater.* **2015**, *26*, 72–81.

(318) Wojciechowski, P.; Ten Hove, P.; Brash, J. L. Phenomenology and Mechanism of the Transient Adsorption of Fibrinogen from Plasma (Vroman Effect). *J. Colloid Interface Sci.* **1986**, *111* (2), 455–465.

(319) Vilaseca, P.; Dawson, K. A.; Franzese, G. Understanding and Modulating the Competitive Surface-Adsorption of Proteins through Coarse-Grained Molecular Dynamics Simulations. *Soft Matter* **2013**, *9* (29), 6978–6985.

(320) Kidoaki, S.; Matsuda, T. Adhesion Forces of the Blood Plasma Proteins on Self-Assembled Monolayer Surfaces of Alkanethiolates with Different Functional Groups Measured by an Atomic Force Microscope. *Langmuir* **1999**, *15* (22), 7639–7646.

(321) Browne, M. M.; Lubarsky, G. V.; Davidson, M. R.; Bradley, R. H. Protein Adsorption onto Polystyrene Surfaces Studied by XPS and AFM. *Surf. Sci.* **2004**, *553* (1–3), 155–167.

(322) Serra, J.; González, P.; Liste, S.; Serra, C.; Chiussi, S.; León, B.; Pérez-Amor, M.; Ylänen, H. O.; Hupa, M. FTIR and XPS Studies of Bioactive Silica Based Glasses. *J. Non. Cryst. Solids* **2003**, *332* (1–3), 20–27.

(323) Serro, A. P.; Gispert, M. P.; Martins, M. C. L.; Brogueira, P.; Colaço, R.; Saramago, B. Adsorption of Albumin on Prosthetic Materials: Implication for Tribological Behavior. *J. Biomed. Mater. Res. Part A* **2006**, *78* (3), 581–589.

(324) Vanea, E.; Tămăşan, M.; Albon, C.; Simon, V. Synthesis and Characterisation of a New Composite Aluminosilicate Bioceramic. *J. Non. Cryst. Solids* **2011**, *357* (22–23), 3791–3796.

(325) Vanea, E.; Magyari, K.; Simon, V. Protein Attachment on Aluminosilicates Surface Studied by XPS and FTIR Spectroscopy. *J. Optoelectron. Adv.*

Mater. **2010**, *12* (5), 1206–1212.

(326) Du, Y. Z.; Hiratsuka, Y.; Taira, S.; Eguchi, M.; Uyeda, T. Q. P.; Yumoto, N.; Kodaka, M. Motor Protein Nano-Biomachine Powered by Self-Supplying ATP. *Chem. Commun.* **2005**.

(327) Wu, D.; Tucker, R.; Hess, H. Caged ATP - Fuel for Bionanodevices. *IEEE Trans. Adv. Packag.* **2005**.

(328) Martin, B. D.; Velea, L. M.; Soto, C. M.; Whitaker, C. M.; Gaber, B. P.; Ratna, B. Reversible Control of Kinesin Activity and Microtubule Gliding Speeds by Switching the Doping States of a Conducting Polymer Support. *Nanotechnology* **2007**.

(329) Rahim, M. K. A.; Fukaminato, T.; Kamei, T.; Tamaoki, N. Dynamic Photocontrol of the Gliding Motility of a Microtubule Driven by Kinesin on a Photoisomerizable Monolayer Surface. *Langmuir* **2011**.

(330) Rahim, M. K. A.; Kamei, T.; Tamaoki, N. Dynamic Photo-Control of Kinesin on a Photoisomerizable Monolayer - Hydrolysis Rate of ATP and Motility of Microtubules Depending on the Terminal Group. *Org. Biomol. Chem.* **2012**.

(331) Moorjani, S. G.; Jia, L.; Jackson, T. N.; Hancock, W. O. Lithographically Patterned Channels Spatially Segregate Kinesin Motor Activity and Effectively Guide Microtubule Movements. *Nano Lett.* **2003**.

(332) Schroeder, V.; Korten, T.; Linke, H.; Diez, S.; Maximov, I. Dynamic Guiding of Motor-Driven Microtubules on Electrically Heated, Smart Polymer Tracks. *Nano Lett.* **2013**.

(333) Kreit, E.; Mäthger, L. M.; Hanlon, R. T.; Dennis, P. B.; Naik, R. R.; Forsythe, E.; Heikenfeld, J. Biological versus Electronic Adaptive Coloration: How Can One Inform the Other? *Journal of the Royal Society Interface*. **2013**.

(334) Chou, K. F.; Dennis, A. M. Förster Resonance Energy Transfer between Quantum Dot Donors and Quantum Dot Acceptors. *Sensors (Switzerland)* **2015**.

(335) Feng, C. L.; Zhong, X. H.; Steinhart, M.; Caminade, A. M.; Majoral, J. P.; Knoll, W. Functional Quantum-Dot/Dendrimer Nanotubes for Sensitive Detection of DNA Hybridization. *Small* **2008**.